CERN – EUROPEAN ORGANIZATION FOR NUCLEAR RESEARCH

CLIC – Note – 994

LHC AND CLIC LLRF FINAL REPORTS

A. Dexter, G. Burt, B. Woolley, P. Ambattu, I. Tahir, ULAN-CI
Igor Syratchev, Walter Wuensch, CERN

Abstract

Crab cavities rotate bunches from opposing beams to achieve effective head-on collision in CLIC or collisions at an adjustable angle in LHC. Without crab cavities 90% of achievable luminosity at CLIC would be lost. In the LHC, the crab cavities allow the same or larger integrated luminosity while reducing significantly the requested dynamic range of physics detectors. The focus for CLIC is accurate phase synchronisation of the cavities, adequate damping of wakefields and modest amplitude stability. For the LHC, the main LLRF issues are related to imperfections: beam offsets in cavities, RF noise, measurement noise in feedback loops, failure modes and mitigations. This report develops issues associated with synchronising the CLIC cavities. It defines an RF system and experiments to validate the approach. It reports on the development of hardware for measuring the phase performance of the RF distributions system and cavities. For the LHC, the hardware being very close to the existing LLRF, the report focuses on the requirements on the LLRF to mitigate anticipated imperfections

CERN-OPEN-2013-032
25/10/2013

Geneva, Switzerland
Date 25/10/2013

Grant Agreement No: 227579

EuCARD

European Coordination for Accelerator Research and Development

Seventh Framework Programme, Capacities Specific Programme, Research Infrastructures, Combination of Collaborative Project and Coordination and Support Action

DELIVERABLE REPORT

LHC AND CLIC LLRF FINAL REPORTS

DELIVERABLE: D10.3.3

Document identifier:	EUCARD-Deliverable-D10 3 3.doc
Due date of milestone:	End of Month 36 (February 2012)
Report release date:	01/07/2013
Work package:	WP10: SRF
Lead beneficiary:	ULAN
Document status:	Final

Abstract:

Crab cavities rotate bunches from opposing beams to achieve effective head-on collision in CLIC or collisions at an adjustable angle in LHC. Without crab cavities 90% of achievable luminosity at CLIC would be lost. In the LHC, the crab cavities allow the same or larger integrated luminosity while reducing significantly the requested dynamic range of physics detectors. The focus for CLIC is accurate phase synchronisation of the cavities, adequate damping of wakefields and modest amplitude stability. For the LHC, the main LLRF issues are related to imperfections: beam offsets in cavities, RF noise, measurement noise in feedback loops, failure modes and mitigations. This report develops issues associated with synchronising the CLIC cavities. It defines an RF system and experiments to validate the approach. It reports on the development of hardware for measuring the phase performance of the RF distributions system and cavities. For the LHC, the hardware being very close to the existing LLRF, the report focuses on the requirements on the LLRF to mitigate anticipated imperfections.

The European Coordination for Accelerator Research and Development (EuCARD) is a project co-funded by the European Commission in its 7th Framework Programme under the Grant Agreement no 227579. EuCARD began in April 2009 and will run for 4 years.

Delivery Slip

	Name	Partner	Date
Authored by	A. Dexter, G. Burt, B. Woolley, P. Ambattu, I. Tahir, I. Syratchev, W. Wuensch	[ULAN-CI] [CERN]	31/10/12
Edited by	G. Burt, A. Dexter, B. Woolley	[ULAN-CI]	31/10/12
Reviewed by	P. McIntosh	[STFC]	10/06/13
Approved by Project Coordinator	Jean-Pierre Koutchouk		01/07/13

TABLE OF CONTENTS

Executive Summary

EUCARD Task 10.3 sets out to develop prototype crab cavities and design their associated LLRF systems for both CLIC (Part 1) and LHC (Part 2).

PART 1: CLIC

Luminosity Upgrade.crab cavities rotate bunches from opposing linacs to achieve effective head-on collisions. Without crab cavities 90% of achievable luminosity would be lost. Maximising luminosity requires accurate phase synchronisation of the cavities, adequate damping of wakefields and modest amplitude stability. This report develops issues associated with synchronising the cavities. It defines an RF system and experiments to validate the approach. It reports on the development of hardware for measuring the phase performance of the RF distributions system and cavities.

Worst case beam loading arising from an offset beam is hundreds of kilowatts and hence the RF system will be high power. In order to keep luminosity loss below 2%, zero crossing times of the RF fields in the crab cavities must not differ by more than 4.4 femto-seconds. This timing error corresponds to 19 milli-degrees at 12 GHz or 9.5 milli-degrees at 6 GHz. The prospect of cavity phase correction using a high power device such a Klystron to this precision during a 156 ns pulse is too daunting to be worth considering. Precise phase control at the level of 20 milli-degrees can be avoided if the same device powers both cavities. In this instance only the phase between the pair of synchronised cavities and the beam must be controlled. The precision of this control depends on the depth of focus at the IP and is likely to be hundreds of milli-degrees.

When trying to drive cavities from the same power source we have the unfortunate situation that the beam offset is certain to be different at the two cavities and hence beam loading will be different. In order for one RF source to power both cavities a solution is needed where the cavity fields are relatively insensitive to beam loading. This is easily achieved by have losses which are much bigger than the beam loading. This pushes the power requirement to tens of Mega Watts. As a drive beam is not easily made available near the CLIC interaction point, the crab cavities are likely to be driven with a klystron. The development of high power short pulse klystrons is very expensive and hence there is a preference to use existing infra-structure. For this reason a CLIC crab cavity solution is being sort at 12.0 GHz rather the 6, 4 or 2 GHz. Operating at a lower frequency would make damping the wake fields easier however power requirement increases and the measurement of the phase difference between the cavities becomes more demanding.

The report presents key results from other EUCARD project work regarding the choice of the crab cavity structure, the required number of cells and sensitivity to beam loading. This work defines the power requirement of a single cavity to be at least 8 MW and the preferred solutions require slightly more. As two cavities must be driven and there will be waveguide losses, the minimum klystron power requirement is 20 MW. The existing SLAC XL5 klystron can deliver 50 MW without a SLED.

The report proposes a position for the klystron and enumerates factors that affect the differential path length to the two crab cavities. It is realised that path length correction (in the high power waveguide) at the level of degrees and on a timescale of seconds is certain to be necessary. The report sets out a baseline design for both the LLRF system and the high power RF system. The report finally describes prototype LLRF instrumentation that has been developed to make the required phase measurements during a range of cavity and high power

waveguide distribution experiments.

PART 2: LHC

With respect to the LLRF control system required for the LHC crab cavities, it was established early in the project that the LLRF system currently in use for the LHC accelerator cavities would only require minor modification for it to give satisfactory performance for the proposed Crab Cavities to be implemented on LHC. During the course of the EUCARD project, the Crab Cavity option for the Luminosity Upgrade has become recognised as the preferred technology choice. As a consequence, CERN directed additional effort to study LLRF effects, these studies are independent of EUCARD task M10.3.3 and hence are referenced here but not reported explicitly here.

This report starts by making an overall assessment of RF control requirements. It then gives details of LLRF parametric control studies based on simulations. The simulations consider a generic controller IQ rather than a model of the actual controller used for the LHC acceleration system, which is then adapted to operate with the Crab cavities. The goal of the parametric study is to disentangle issues that need to be faced when designing the LHC LLRF from formerly anticipated difficulties that turn out to be manageable. The potential beam offset at the crab cavities is shown to require a manageable increased RF power within agreed hypotheses. The failure of a crab cavity (quench, power failure) or of its LLRF control is shown to be potentially dangerous to the machine integrity but liable to be mitigated by appropriate control strategies and independent safety devices (e.g. measurement of the phase difference between the cavity and the beam, triggering the beam dump above a given threshold). Realistic measurement errors do not seem to perturb unduly the RF control. However, the system performance is highly dependent on the gain that needs to be high. An analysis of the RF system noise attempts at giving clues on its impact on the beam emittance..

1. Introduction to Part 1 (CLIC)

The CLIC CDR [1] proposes a crossing angle for the interacting beams of θ_c = 0.02 radians. The proposal for a 3 TeV centre of mass energy have vertical and horizontal beam sizes at the interaction point before the pinch of σ_y = 1 nm and σ_x = 40 nm respectively and a bunch length of σ_z = 44 μm. The slender profile of the bunches at the interaction point (IP) means that if they retain their crossing angle at the IP then luminosity will be reduced to just 10% of what could be obtained when the bunches are rotated to meet on. Bunches will be rotated to meet head on using crab cavities placed in the beam delivery lines before the IP. A crab cavity is a deflection cavity operated with a 90^o phase shift [2] so that a particle at the front of a bunch gets a transverse momentum kick equal and opposite to a particle at the back of a bunch while a particle in the bunch centre gets no momentum kick. The overall effect is the application of an apparent rotation rate to the bunch. The bunch inclination observed at the IP depends on momentum kick and the horizontal optical transfer function R_{12} .

Linear collider crab cavities are typically placed immediately before the final focus quadrupoles and hence are in a region of high β. This position minimises the transverse gradient that the cavity must provide. If the phase of a crab cavity is not exactly 90^o from the phase of maximum possible deflection then the bunch rotates about a point that is not its geometrical centre and hence gains an average deflection at the IP. If two bunches that should collide have differing average deflections then their axial centres miss each other at the IP. If the two crab cavities on opposing linacs are synchronised to each other, but not necessarily to the bunch arrival times, then the deflection to electron and positron bunches are identical and hence head on collision is maintained. Note that the quadrupoles that provide focusing at the IP correct for position offsets at the crab cavities but not transverse momentum errors.

If bunches arrive at the crab cavities from the linac with an offset from the cavity axis they can excite unwanted transverse electromagnetic cavity modes. These modes are collectively known as transverse wakefields and can impart additional unwanted transverse momentum (deflections) to the bunches. The most serious deflections are those in the vertical plane as the bunch height is only 1 nm.

The three key issues for crab cavities which might limit luminosity recovery to its maximum value associated with head on collision are.

- phase synchronisation of the cavities,
- achieving the correct amplitude so bunches get the correct rotation
- minimising wakefields.

Poor phase synchronisation gives horizontal position errors Δx at the IP, the most serious issue for wakefields is vertical position errors Δy at the IP and amplitude fluctuations give rotation errors Δθ at the IP [3]. The effects of small errors on the luminosity reduction factor S can be estimated using

$$S_{rms} \cong \left(1+\left(\frac{\Delta x_{rms}}{2\sigma_x}\right)^2\right)^{-\frac{1}{4}} \left(1+\left(\frac{\Delta y_{rms}}{2\sigma_y}\right)^2\right)^{-\frac{1}{4}} \left(1+\left(\frac{\sigma_z \Delta\theta}{2\sigma_x}\right)^2\right)^{-\frac{1}{2}} \quad (1)$$

where σ_x and σ_y are horizontal and vertical bunch sizes at the IP, σ_z is bunch length and errors Δ are measured bunch to bunch (not bunch to centre).

The formula assumes Gaussian distributions for synchronisation errors giving horizontal displacements and wakefields giving vertical displacements. Here the amplitude error giving angular errors is taken to be steady and $\Delta\theta$ is the angle between the two bunches at the IP. More will be said about this assumption after the cavity technology choice has been discussed.

The other approximation in (1) is neglecting the beam-beam interaction. As the colliding bunches have opposite charge they attract and hence luminosity loss with respect to the horizontal plane miss alignment are typically less than estimates not including the beam-beam interaction.

A large component of the cost of CLIC will come from the linac structures and their tunnels. Minimisation of machine cost is essential for affordability and hence the structure optimisation focuses on gradient (without breakdown). The cost of crab cavity system is small in comparison with rest of the linear collider, it is optimised almost solely on luminosity performance. There may be additional constraints on size and power source.

2. Phase Synchronisation Requirement

A crab cavity to cavity timing error Δt gives a transverse bunch position error at the IP of $\theta_c c \Delta t$, where θ_c is the beam crossing angle. Phase errors in degrees are related to timing errors using $\Delta\phi = 360 f \Delta t$ where f is the RF frequency. Not including vertical offsets and bunch rotation errors then (1) can be used to determine the maximum allowable r.m.s. cavity to cavity phasing error $\Delta\phi_{r.m.s.}$ as a function luminosity reduction factor $S_{r.m.s.}$ giving

$$\Delta\phi_{rms} = \frac{720\,\sigma_x f}{c\theta_c}\sqrt{\frac{1}{S_{rms}^4}-1} \quad \text{degrees} \qquad (2)$$

The target limit on luminosity reduction factor $S_{r.m.s.}$ from the crab system is about 0.98 and hence for 12 GHz RF (2) gives the maximum acceptable cavity to cavity phase error as 0.019 degrees. This phase error corresponds to a timing error of 4.4 ns. Equation (2) indicates that the phase error tolerance become tighter as the frequency reduces. The maximum timing error of 4.4 ns is independent of frequency of operation.

3. Luminosity Loss for Amplitude Errors

The angular bunch error $\Delta\theta_1$ caused by an amplitude error ΔV on one cavity is determined as $\Delta\theta_1/0.5\theta_c = \Delta V/V_o$ where V_o is the voltage needed for the correct crabbing angle. When the errors act to keep the bunches parallel, any orientation to the direction of motion still results in a loss of luminosity. This means that the angular error to include in (1) when both cavities have amplitude errors $\pm\Delta V$ is $\Delta\theta/\theta_c = \Delta V/V_o$. Not including horizontal and vertical offsets then (1) determines the maximum cavity amplitude error as a function luminosity reduction factor S to be

$$\frac{\Delta V}{V_o} = \frac{2\,\sigma_x}{\sigma_z\,\theta_c}\sqrt{\frac{1}{S^2}-1} \qquad (3)$$

taking S = 0.98 as before then the associated amplitude error is 2.1%. Of course a value much smaller than this is needed as this loss adds to that from wake field effects and synchronisation errors.

4. RF Requirement

Conventional crab and deflection cavities utilise a TM110 like mode to provide the deflection [4]. This mode is a dipole mode and provides zero longitudinal acceleration on its axis. How much power one requires to provide the transverse kick voltage depends on the loaded Q factor of the cavity and beam loading. For optimum power transfer one matches the loaded Q to worst case beam loading and cavity losses. For a crab cavity beam loading only occurs when the bunch is off axis. Beam loading changes its sign depending on which side of the cavity axis that the beam passes, on one side the beam takes power and on the other it adds power.

For the purpose of estimating power requirement we suppose that maximum bunch offset where cavity amplitude can be maintained is to be $\Delta x_{cc} = 375\ \mu m$. For the purpose of estimating luminosity reduction as a consequence of wake fields and amplitude errors we assume $\Delta y_{cc} = 50\ \mu m$ and $\Delta x_{cc} = 125\ \mu m$. These offsets are generous compared to estimated bunch sizes at the crab cavity of $\sigma_{ycc} \cong 35\ \mu m$ and $\sigma_{xcc} \cong 153\ \mu m$ [5].

With respect to estimating worst case beam loading one anticipates that sequences of bunches might arrive with similar offsets. A minimum power estimate comes from neglecting cavity losses. When a bunch of charge q passes through a dipole cavity at the perfect crabbing phase with repetition frequency f_{rep}, with offset a then as given in [6] the power P_a extracted from the cavity is determined by

$P_b = qV_\perp\left(\frac{2\pi f\, a}{c}\right) f_{rep}$ where the transverse kick voltage is determined as $V_\perp \cong \frac{\theta_c E_o c}{4\pi f\, R_{12}}$.

In this formula E_o is the beam energy, f is the RF frequency and R_{12} is a parameter that relates horizontal deflection at crab cavity to offset at the IP. For the purpose of the calculations here we have taken R_{12} as 23.4 m. The RF frequency has to be a multiple of the CLIC 1.99903 GHz repetition frequency. Using the parameters given previously the power requirement to satisfy worst case beam loading is hundreds of kilowatts.

It is anticipated that CLIC will operate with a bunch train of 312 bunches and hence the train passes in 156 ns. The requirement then becomes to maintain the synchronisation of two cavities which are 50 metres apart to within 4.4 fs and with amplitude control to very much better than 2%. Measuring amplitude and phase accurately and then correcting with a power supply delivering hundreds of kilowatts on a time scale much less that 150 ns is not feasible with current technology.

5. Technology Choice

Whilst the crab cavities could be operated at any frequency multiple of 1.99903 GHz the availability of power sources and major infra-structure guides the frequency choice at the initial development stage. Initial development supposes 11.9942 GHz operation as at this frequency the phase synchronisation target is less than what it would be for lower frequencies. If the satisfactory damping of wake fields was to turn out to be impossible at 11.9942 GHz one would want to consider 5.9971 GHz at the next frequency choice.

Given that beam loading is likely to be unpredictable for CLIC, the proposed solution is to have a power flow through the cavity that is significantly higher than the maximum beam loading power requirement. This is most easily realized with a high group velocity travelling (TW) wave cavity. An important criterion with respect to proving system performance is the

ability to measure phase at the milli-degree level. When making the choice of phase advance per cell (including the standing wave cavity option) one has to be weary of mode separation as the excitation of modes adjacent to the operating mode [6] can easily lead to inaccuracies in the measurement of the phase of the operating mode when the sampling period is a fraction of the 156 ns bunch train period.

6. RF Layout

High power RF at 11.9942 GHz could be provided either by klystrons or by a drive beam and PET structures [1]. The beam delivery system for CLIC will be several kilometres in length and hence the drive beam for the main linac is not easily made available near the IP. It is also thought that phase jitter generated in the PET structures is likely to be too large for the phase synchronisation target to be met. The existing XL5 klystron delivers up to 50 MW at 12 GHz [7] and hence without using a SLED this power level is an initial constraint. The 50 MW can be increased substantially with a SLED device but this device may introduce its own phase jitter. Klystrons will have phase jitter on their output coming from modulator ripple. Whilst in principle this can be corrected, the difficulty of making an accurate phase measurement and correcting phase on a timescale much less than 156 ns looks insurmountable. The proposed solution is to use one klystron to drive crab cavities on both linacs. This is effectively the same proposal made by J. Frisch for synchronising the NLC crab cavities [8]. If one klystron drives both cavities and it takes the same time for the power to propagate from the klystron to each crab cavity then phase jitter arising from the klystron is identical for each crab cavity. This means that positron and electrons deflection arising from klystron jitter are identical and luminosity is maintained. If RF length of the two paths from the klystron to the two cavities varies, then one phase moves with respect to the other; deflections of the beams differ and luminosity is lost. Importantly the RF path lengths from the klystron to the two cavities must be kept identically equal.

The CLIC interaction region is likely to have two detector caverns as shown in figure 1. The detector in use sits in the transfer tunnel.

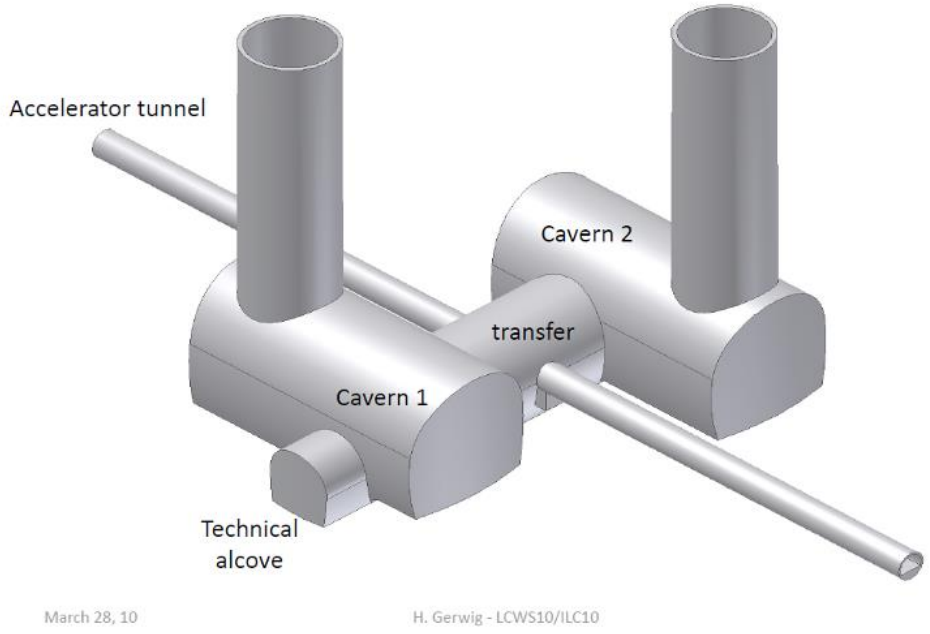

Figure 1 Civil engineering for CLIC interaction region

Figure 2 shows the layout of figure 1 in plan. The klystron for the crab cavities is likely to be positioned at the back of one of the detector caverns (halls), perhaps in its own bunker. The current design of the IP optics puts the crab cavities 23.4 metres from the IP. The crab cavities are therefore in the tunnel. The shortest distance from the klystron to a crab cavity on the linac is about 50 metres.

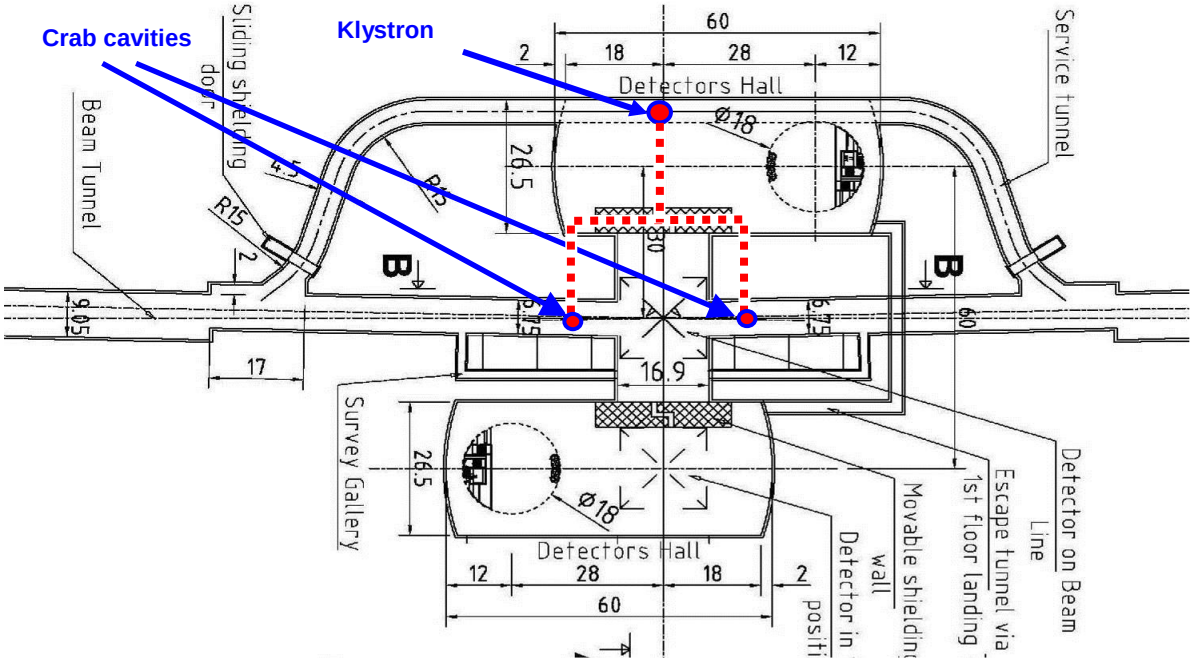

Figure 2 Plan of CLIC interaction region with crab cavities marked

As waveguides will be subject to vibration and temperature changes then they will contribute to phase errors between the cavities. For this reason one wants to keep the waveguide length after the division taking power to individual cavities as short as practical. The most straightforward layout is to split the waveguide and hence the power on the side of the detector hall cavern closest to the beam line. Figure 3 shows the configuration in 3 dimensions.

The waveguide split needs to be central so that phase fluctuations arrive at the two cavities at the same instant. In order to leave a clear passage for the detector to be moved, the waveguide split could be positioned above (or below but we will assume above) the cavern doors. One is likely to have dedicated bores from the cavern to the tunnel for the waveguides going to the crab cavities. We will assume that these bores are horizontal and perpendicular to the beam line. The waveguide will need at least one bend after the split. Assuming rectangular waveguide and to minimise mode conversion one would want to restrict bends to 90 degree E and H plane types or pairs of 45 degree E and H plane types. The path length can be reduced by cutting a corner using 45 degree bends. In order to deliver power to the coupler with the correct orientation one might start with an H plane splitter above the cavern door. On the route to a crab cavity one could have two 45 degree E bends in the cavern to bring the waveguide to the same height as the beam line. A 90 degree H bend would be used to take the waveguide into the bore. The waveguide now has the correct orientation to meet with a single feed power coupler on the cavity. For the dual feed coupler an extra E plane bend is required at the cavity. The distance from the split to the cavity following the waveguide as shown will be about 40 metres.

Assuming a waveguide group velocity of 2.5×10^8 (Rectangular waveguide EIA90 TE01) then the RF energy that will pass through the cavity while the bunch is passing occupies a length in the waveguide of 39 metres. This means that the energy that will maintain the field in the cavity while the bunch is passing has been completely determined before anything can be known about the bunch at the location of the klystron. The length of the waveguide also means that one does not need to worry about reflections from the cavity influencing the other cavity. If a circulator is needed to protect the klystron it would be mounted on the common output port of the klystron before the splitter.

The waveguide from the Klystron to the splitter could be optimised for low loses whilst the waveguide from the splitter to the cavities must be optimised for phase stability.

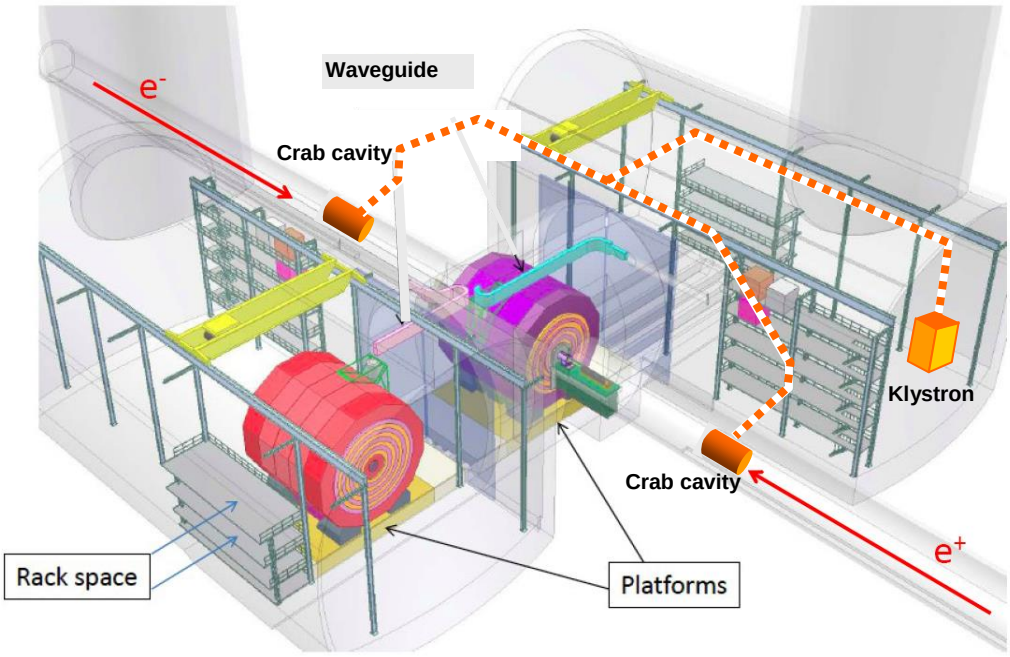

Figure 3 CLIC interaction region

7. Control loops

The proposed high power RF component schematic is shown in Figure 4. Output from the 50 MW klystron is split and carried along equal lengths of stabilised and temperature controlled waveguide to the crab cavities on opposing beams. There are three control loops, one synchronises the cavity RF to the beams, another controls the output of the klystron with respect to its input and the third maintains identical RF path lengths from the splitter to the crab cavities.

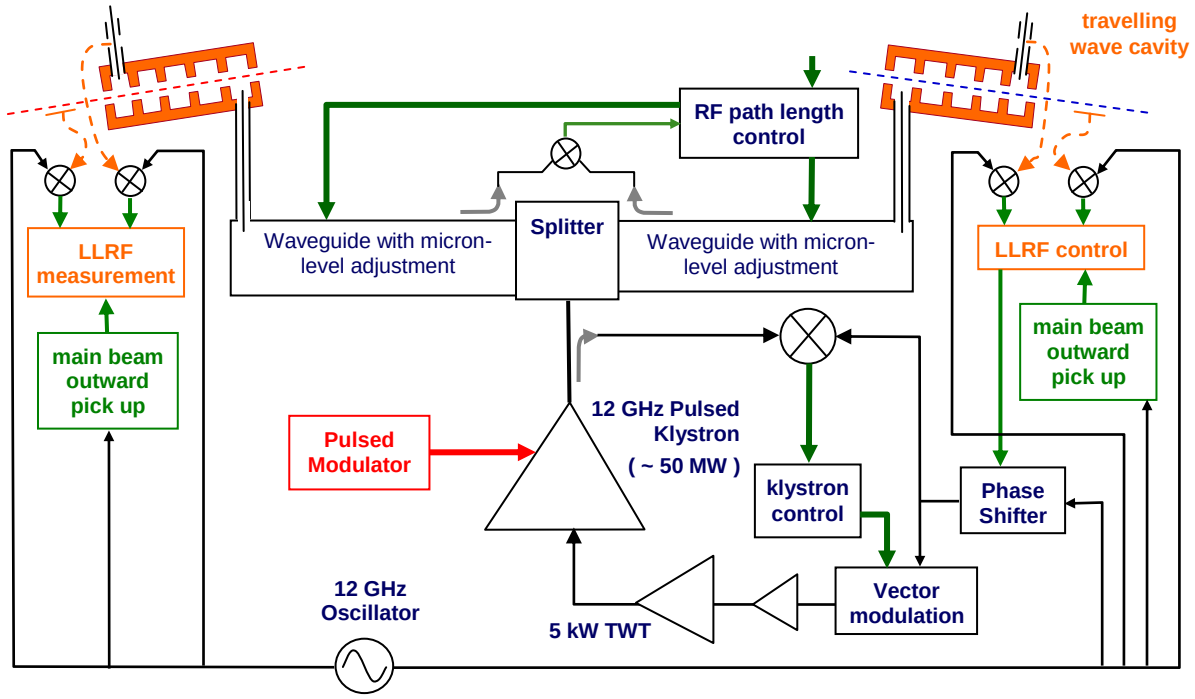

Figure 4 Proposed CLIC crab cavity system architecture

Cavity synchronisation is completely dependent on identical path lengths for the high power RF from the splitter to the cavities. Given that the r.m.s. cavity to cavity synchronisation requirement is 4.4 fs then the r.m.s. klystron to cavity stability requirement is $4.4/\sqrt{2} = 3.1$ fs (as there are two paths). The phase velocity of light in the waveguide will be just over 3.0×10^{8} hence the length of the waveguide must be steady at the precision of 10^{-6} metres. The waveguide paths must remain accurately identical over a timescale where phase differences can be measured and corrected. If this time is minutes then beam - beam interaction measurements might allow any phase offset to be corrected. If this time is less than the time it takes to make a phase length correction to the waveguide then the luminosity budget cannot be achieved. One option which will allow correction on the timescale of milli-seconds would be to send a pre-pulse at a frequency that is reflected by the cavities and then to measure the phase difference between the returning signals. Mechanical phase shifters in the waveguide could then make small corrections to the RF path length based on the return trip phase errors. A second option which does not require a pre-pulse is to have an optical interferometer providing reference phases at the cavities that are synchronized to 1 fs [9]. In this case waveguide phase shifters could be positioned near to the cavities.

In order for the proposed scheme of a single klystron delivering power to both cavities to work it is important that the cavity and its couplers are designed and manufactured to be perfectly matched. One would also want the cavity phase to follow the input phase as closely as possible. In order to achieve this one might mount the cavity centrally so that expansion gives phase errors that cancel. Careful attention to cavity temperature control will be needed so that the two systems perform in an identical fashion.

8. Waveguide expansion

The difficulty of achieving stability and equal RF path lengths at the micron level becomes evident when expansion of the waveguide is considered. If the waveguide is in a temperature controlled environment one might hope to control its temperature to better than 0.3°C. The expansivity of copper at room temperature is 17×10^{-6} K^{-1}. This means that a 40 metre waveguide could vary in length by 200 μm within the temperature controlled environment. For 12 GHz operation the waveguide wavelength will be a little over 25 mm and hence an expansion of 200 μm gives a phase shift of 2.9 degrees which is 150 times the allowance! It is probable that the waveguide will have expansion joints and so the real question is about the lateral stability of the cavity and the klystron.

Lateral expansion of the waveguide causes the wavelength to change. For the TE10 mode the wavelength is given as $\lambda = \frac{c}{f}\left\{1-\left(\frac{c}{2af}\right)^2\right\}^{-0.5}$ where f is the frequency and a is the waveguide width. If as before we allow 40 metres of waveguide carrying power at 12 GHz to change its temperature by 0.3°C then for a waveguide of width 24 mm the phase will change by -0.93 degrees.

Without expansion joints or compensation it is interesting to ask about the time scale required for correcting phase errors. A rectangular copper waveguide of width 24 mm, height 12 mm, and length 40 m and wall thickness 2 mm has an external area of 3.52 m^2 a volume of 0.0064 m^3 and would have a heat capacity of mc_p = 22 kJ K^{-1}. Assuming that the waveguide is mounted in an insulated tube and has its temperature controlled with a cold turbulent air stream over its outer surface (~ 3 ms^{-1}) then one anticipates a heat transfer coefficient of about 16 W m^{-2} K^{-1} being achieved. If one assumes that the cold air cooling the waveguide has temperature fluctuations of the order of 0.3 K then the uncertainty in the heat supply to the waveguide $\dot{Q}$ is potentially 17 W. The change in temperature with time is therefore $\frac{dT}{dt} = \frac{\dot{Q}}{mc_p} = \frac{17}{22k} = 0.8\times10^{-3}$ K s^{-1} hence the longitudinal expansion is about 0.5 μm s^{-1}. One concludes that if phase errors are driven by thermal expansion then necessary corrections must be made on a time scale of seconds.

A further question for the development of the CLIC crab cavity RF system is the level of lateral stability that can be achieved. It is certain that movements greater than 1 μm can be expected on timescales of hours.

Taking all these discussions into account there is no choice but to have some means of measuring and correcting the phase difference on the waveguide paths. Even with active measurement and correction one would almost certainly want to limit the magnitude of correction that is necessary.

It would be our recommendation to use copper plated INOVAR®[10] waveguide rather than copper waveguide. Copper plating is necessary as INOVAR®'s low electrical conductivity would result in a 99.4% power loss for the 24x12 mm 40 m waveguide. INOVAR® has a low thermal expansion coefficient of 0.65×10^{-6} K^{-1} and heat capacity 510 J Kg^{-1}. This low thermal expansion reduces phase errors caused by longitudinal and lateral expansion to 96 and 36 milli degrees respectively. Coupled with INOVAR®'s higher heat capacity the longitudinal expansion is reduced to 16 nm s^{-1}.

9. Structure Choice

The disc loaded waveguide travelling wave structure is well proven as a deflecting cavity [4, 11] and has been selected as the structure for experimental investigation during the TDR phase [12]. Design studies indicate that the wakefield damping requirements cannot be met with circular symmetry and a new design to be developed will have elliptical cells. Cell length is determined by phase advance per cell. A free choice of iris radius and iris thickness can be made and then the equator radius must be chosen to fix the required phase advance for the frequency of 11.9942 GHz.

10. Power Requirement and Number of Cells

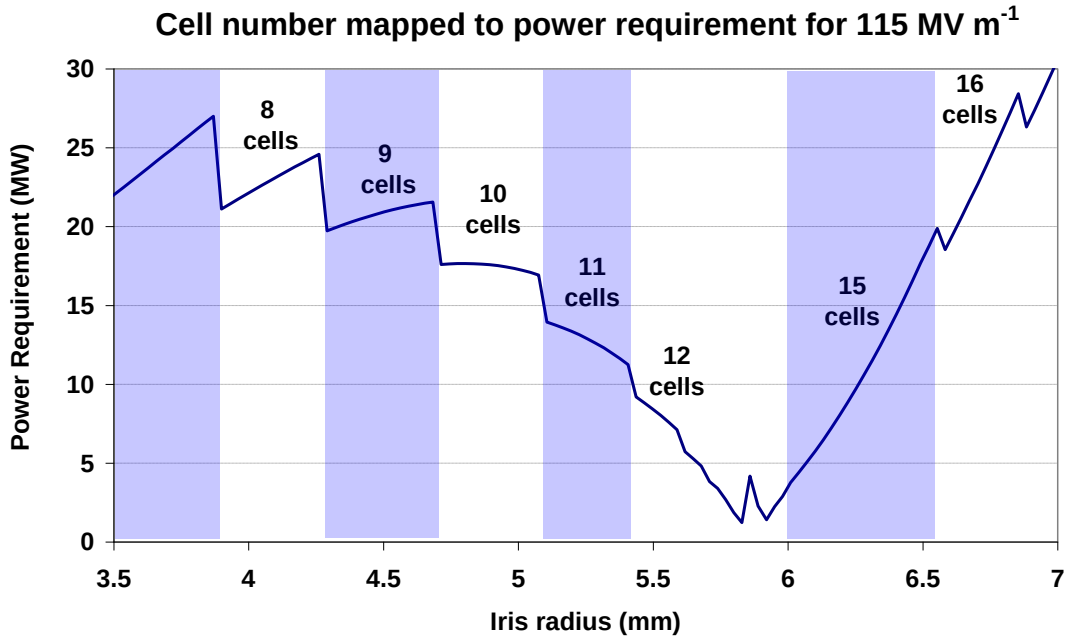

Figure 5 Power requirement as a function of iris radius maintaining maximum gradient and allowing cell number to vary.

An initial study [13] has identified a range of cell designs that are favourable to minimising wake fields and maximising gradient. The minimum cell number is determined by maximum kick per cell. From the formula given earlier, the required transverse voltage for 3 TeV operation is 2.55 MV. The maximum kick per cell will be limited by the maximum surface field and the R/Q. Reducing the iris radius increases the R/Q of the operating mode and the maximum kick per cell however it also increases the R/Q of all the other modes that contribute to the wake fields. The wake fields are expected to increase linearly with the number of cells for small numbers of cells. The structure can be made insensitive to beam loading if the structure is very inefficient. The structure is made inefficient by having a high group velocity and a small number of cells. The allowable inefficiency is limited by the maximum power available. Nominally one has 50 MW to drive two cavities but there will be waveguide losses. Figure 5 shows the results from the study for an assumed peak surface field of 115 MV m^{-1}. For iris radii 3.5 mm to 4.7 mm the group velocity is negative and increasing in magnitude, for iris radii from 4.7 mm to 5.8 mm the group velocity is negative and decreasing in magnitude, for iris radii 5.8 mm upwards the group velocity is positive and increasing. For iris radii between 5.6 mm and 6.1 mm the group velocity is small, power does not flow through the

structure and hence it becomes sensitive to amplitude fluctuations. Acceptable cell numbers at this gradient with a power requirement less than 25 MW per cavity are 8 to 12, 15 and 16. If the surface field constraint is reduced one needs more cells but consumes less power. More cells gives larger wake fields for the same R/Q. In the next section we realise that the 8, 9 and 16 cell options can be ruled out due to waveguide losses and the 10 cell option requires an over moded waveguide.

11. The RF Distribution System

When one considers standard EIA90 waveguide for the transmission one realises that for a 40 metre length only 40% of the power is transmitted. This means that only 10 MW is available per cavity and only the 12 cell and 15 cell options with iris radii of 5.5 mm and 6.2 mm are possible when using the surface field limit of 115 V m^{-1}. Table 1 considers various options for the waveguide.

Table 1 Waveguide losses

Copper σ =5.8e7 S/m and at 11.994 GHz	Attenuation	Trans-mission	Over moded	Power for cavity
Rectangular TE10 EIA90 (22.9 x 10.2 mm)	0.098 dB/m	40.6%	no	10.2 MW
Rectangular TE10 special (24 x 14 mm)	0.073 dB/m	51.3%	no	12.8 MW
Circular TE11 (r = 9.3 mm)	0.119 dB/m	33.3%	no	8.3 MW
Circular TE11 (r = 12 mm)	0.055 dB/m	60.4%	TM10	15.1 MW
Circular TE01 (r = 25 mm)	0.010 dB/m	89.1%	extremely	22.3 MW

For special rectangular waveguide we have 12.8 MW available hence in addition to the 12 and 15 cell solutions there is an 11 cell solution with an iris radius of 5.35 mm. For circular 9.3mm TE11 waveguide only 8.3 MW is available hence the 15 cell solution can be used and the 12 cell for an iris radius of 5.55 mm. For circular 12mm TE11 waveguide we have 15.1 MW available which allows 11 cells. Note that mode conversion from circular TE11 to circular TM10 is vanishingly small for properly designed bends hence over moding for this case is not an issue. Transmission at the 90% level is possible with highly over moded waveguide and this additionally permits 9 and 16 cell options. The problem with an over-moded waveguide is that any mode conversion which is sensitive to micron level dimensional changes will affect synchronisation. There is no real requirement to consider heavily over-moded waveguide on the basis of power requirement unless the klystron cannot be placed at the suggested location with RF paths less than 40 metres.

Table 2 Waveguide phase errors

INOVAR® thermal expansion 0.65 ppm/K and at 11.994 GHz	Phase error due to lateral/width expansion	Phase error due to length expansion
Rectangular TE10 EIA90 (22.9 x 10.2 mm)	40 milli degrees	94 milli degrees
Rectangular TE10 special (24 x 12 mm)	31 milli degrees	96 milli degrees
Circular TE11 (r = 9.3 mm)	113 milli degrees	70 milli degrees
Circular TE11 (r = 12 mm)	53 milli degrees	89 milli degrees
Circular TE01 (r = 25 mm)	53 milli degrees	88 milli degrees

A further consideration when choosing waveguide type is its phase stability as a function of temperature rise. Table 2 shows the phase errors introduced for various different cross-sections of INOVAR® waveguide for a 0.3 K temperature rise. The phase error due to length expansion is relatively constant for the different types of waveguide. The error due to width expansion is similar for all the waveguide choices except the 9.3 mm circular waveguide. Although the special rectangular waveguide has the highest error due to length expansion, it is the best choice for the system as expansion joints will remove this error.

12. RF Distribution Path Length Measurement and Correction.

In order to match the RF path lengths, our first choice option is to make continuous path length corrections based on measurements with RF pulses sent along the transmission lines between the linac bunch trains. These measurement pulses will have a frequency just outside the crab cavity bandwidth so they are almost fully reflected from the cavities at the input coupler. This method measures reflections from the cavities close to the E plane splitter in the detector cavern to determine the RF path length difference of the two waveguides beyond the split. Figure 6 shows a schematic of the path length control system which is effectively an RF interferometer.

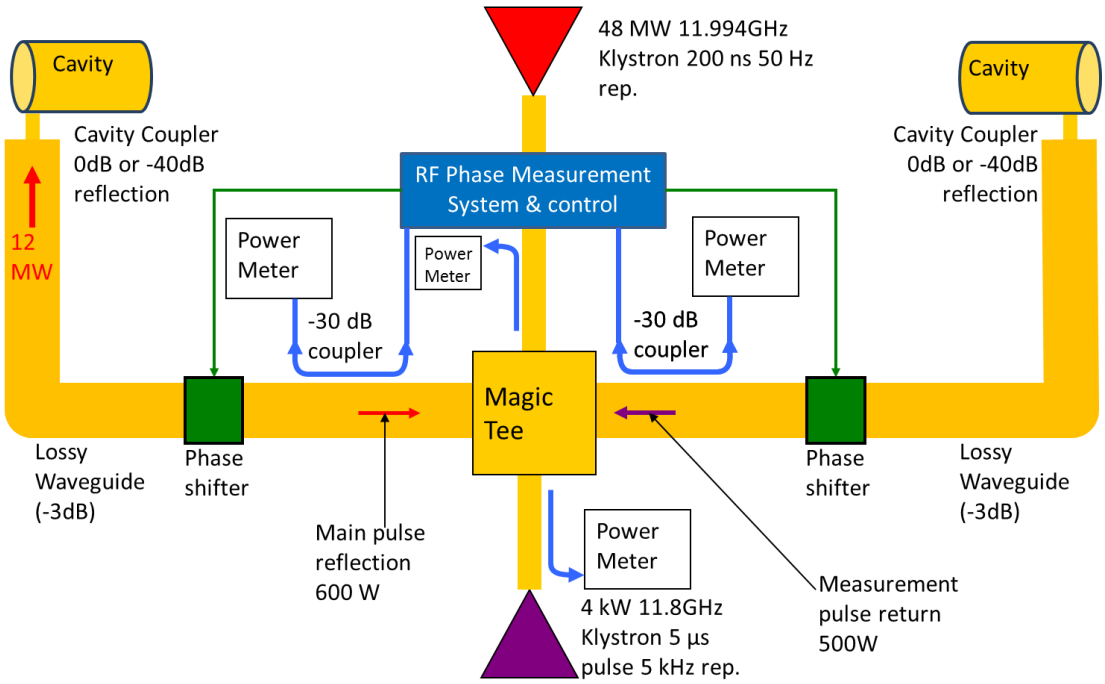

Figure 6 shows a schematic layout of a cavity phase control system.

The main feature of the layout is the introduction of a second, lower power, klystron whose sole purpose is to measure path length. An advantage of a dedicated klystron for path length measurements is that corrections can be performed at a much higher repetition rate than the bunch train repetition rate of 50 Hz. This means that the correction system sees the complete acoustic spectrum for waveguide vibration. Independently of the measurement klystron, the interferometer can make phase measurements based on reflections from the couplers for the high power pulse when the bunch train arrives. For this arrangement the E plane splitter in the detector cavern is now replaced with a magic tee.

The high and low power klystrons are connected to the sum and delta ports of the magic tee respectively. This isolates the klystrons from each other and results in the high power pulse being directed towards each of the cavities in phase and the low power pulse in anti-phase. The high power pulse travels along the waveguides until it interacts with the cavity couplers, by which time it is attenuated by 3 dB due to waveguide losses. The cavity is designed with a small bandwidth at 11.994 GHz, to match the frequency of the high power klystron. A bandwidth implies that a perfect match cannot be achieved. The match of the current design is near to -40 dB. The reflected -40 dB pulse is detected back at the magic tee through the use of -30dB directional couplers and a phase measurement system. In this way a 27.8 dBm signal is delivered to the phase measurement system. (The phase measurement system is described in more detail in section 17.)

The frequency of the low power measurement pulses is chosen at 11.8 GHz, such that it is just outside the cut-off frequency of the cavity and hence is totally reflected. A power of 4 kW is used as this ensures that a 27.0 dBm signal is directed back to the phase measurement system, which is almost identical to the high power pulse. Keeping the measurement power levels the same ensures that no switchable attenuators or diode limiters are needed which could be a source of unwanted vibration or noise.

An additional method of measuring the phase can be used by utilising the phase behaviour of the magic tee. For the high power pulse; if the reflections from the cavities arrive back at the tee in phase, all RF power will return towards the high power klystron at the sum port. Any phase mismatch will cause RF power to be detected at the delta port by a directional coupler and a power meter.

The repetition rate and pulse length of the high power klystron is fixed by the properties of the beam. However, we are free to choose the repetition rate and pulse length of the second probe klystron. The repetition rate will dictate the temporal resolution of the phase measurement system. The fastest sources of phase error contributions are likely to be acoustic vibrations in the region of a few hundred Hertz. Hence, the repetition rate of the probe klystron needs to follow this. Five kilohertz is chosen as it will encompass all these frequencies and many of the higher harmonics generated. Future experiments will further determine if this frequency is sufficient to measure all important acoustic variations.

Since electrical noise on the phase measurement signal is inversely proportional to bandwidth, a longer pulse will result in a lower noise floor and a more precise measurement. However, a long pulse will cause reflections to build as the pulse will reflect back and forth from the klystron to the cavity every ~600 ns. This will result in an incomprehensible signal being detected at the phase measurement system. By choosing the high loss single mode waveguide, reflections are damped somewhat, but will still build up over time. Taking these effects into account, 5 µs represents a good balance between noise level, heat build-up and signal reflections. The pseudo-CW nature of the measurement allows dangerous acoustic modes to be identified and feed-forward correction applied via the phase shifters.

13. Waveguide Phase Shifters

Standard ways of changing phase include dielectric inserts into the waveguide and ferrite loaded waveguide. Ferrite loaded waveguides can change phase on the order of microseconds as there are no moving parts, but are discounted due to their limited power handling. Dielectric waveguide phase shifters can be operated at high power if a low loss dielectric with high dielectric breakdown strength is used, such as diamond. An amplified piezoelectric actuator is

capable of moving the dielectric in and out of the waveguide by 1 mm at a rate of many kilohertz.

To test the performance of such a device a simplified model was constructed in CST Microwave Studio (figure 7). The model consists of a WR90 waveguide with a 1.14 x 20 mm longitudinal slot in the top wall. A shaped diamond insert with a depth of 1 mm mounted on a perfectly electrically conducting substrate is then lowered into the slot. The diamond is shaped to minimise reflections.

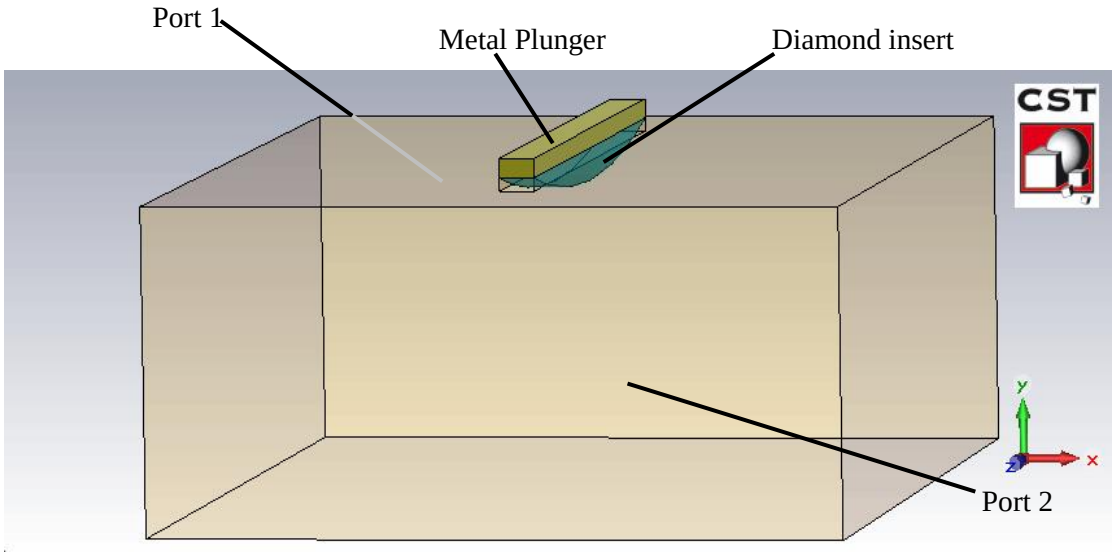

Figure 7 shows the CST MWS model of a simple phase shifter. The wave propagates in the positive z-direction.

The protrusion of the diamond insert was varied from 0 to 1 mm in 0.1 mm steps and a simulation carried out for each step. The relative phase shift, return loss, heat dissipated and maximum electric field were all recorded. A phase shift of just less than 2 degrees was recorded for the full 1 mm movement and a maximum return loss of -46 dB was observed. The reflection performance could be improved by optimisation of the diamond/slot geometry. During the high power pulse the phase shifter will have up to 25 MW of RF power passing through it. Peak heat dissipation in the diamond is 214 W, which is 1.67 mW average, due to the low duty cycle of the pulsed RF. This will be easily carried away through the metal substrate, further aided by the diamond's high heat conduction. The peak electric field is 15.7 MV/m, which is below diamond's dielectric breakdown threshold.

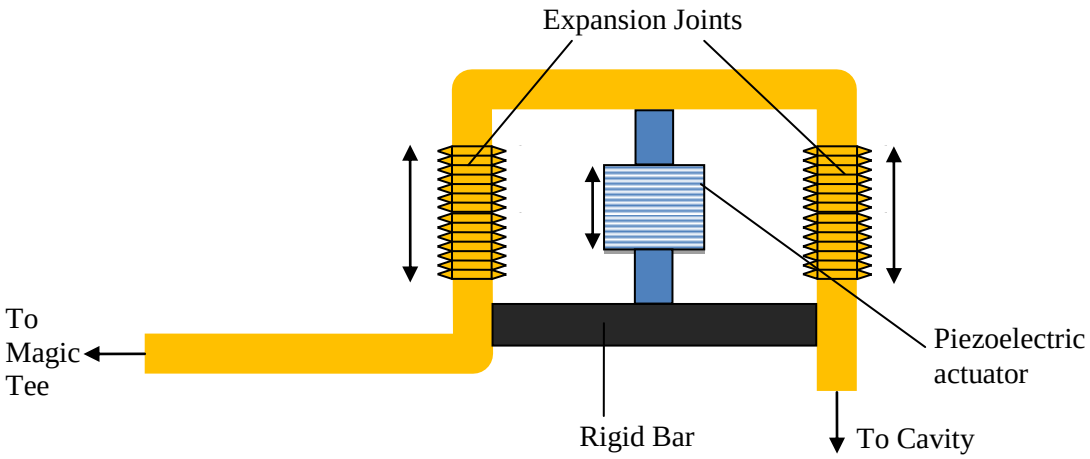

Figure 8 shows the trombone phase shifter.

A second option for a high power phase shifter with a low risk of breakdown is shown in figure 8. It uses a trombone-like structure to physically extend the length of the waveguide. In WR90 waveguide at 11.994 GHz the phase sensitivity to length expansion is 83 nm/milli-degree. A piezoelectric actuator with a resolution of ~40 nm and a free stroke of 83 µm would result in a phase shift of 2 degrees with 1 milli-degree accuracy. Three right angle bends are used with the resulting waveguide path being steered by 90 degrees. This phase shifter would therefore be placed at the end of the long straight section of waveguide in the detector hall, replacing the 90 degree waveguide bend.

Another method of phase control could be to apply external pressure to the waveguide from an electromechanically controlled clamp. This would subtly change the cross section of the waveguide, thus changing the RF propagation constant. This bypasses any chance of dielectric breakdown occurring. For example, decreasing the width of a WR90 waveguide by a micron over 5 cm of length causes a phase change of 11.3 milli-degrees. If a piezoelectric actuator with 100 microns of movement were to be used, a phase change of 1.13° is possible.

Other options include a phase shifter developed by I. Syratchev [14] that uses rotating sections of elliptical waveguide in order to rotate the polarisation of a TE11 mode, hence increasing the RF path length. Any phase shifter used will have to be calibrated at both 11.994 GHz and at 11.8 GHz to ensure no inconsistencies are introduced into the phase correction system when switching between frequencies.

Apart from using phase shifters, phase corrections local to each cavity can be made with medium power klystrons operating in quadrature to the main RF. Such a system has the potential for making corrections during a pulse train. For feedback to work one would need to measure the cavity phase to an accuracy of milli-degrees and then make the correction on the timescale of a few bunches (say 40 ns).

If after actively stabilising and matching waveguide paths to the input couplers it turns out that the relative phase of the two crab cavities drift with respect to each other during the 156 ns pulse in a systematic fashion, then the local RF power correction scheme could be operated with feed forward estimation from the previous bunch train.

14. Double Balanced Mixer Sensitivity

The phase measurement electronics will consist of a double balanced mixer and a digital phase detector. The double balanced mixer will provide the high sensitivity needed to resolve milli-

degrees at 12 GHz, while the digital phase detector will provide a larger dynamic range and a linear response. It is important to consider how the output of the mixer will respond to a given phase offset, as this will determine the amount of amplification needed and the noise performance required. When a mixer is used to measure the phase difference between two signals, its output voltage (V_{IF}) is described by the following expression [15]:

$$V_{IF} = V_{\max} \cos(\pi + \Delta\phi) \tag{4}$$

where $V_{\max}$ is the maximum output voltage and $\Delta\phi$ is the phase difference between the two inputs. The mixer also outputs a voltage whose frequency is twice that of the input. By differentiating with respect to $\Delta\phi$ we can see that the mixer gives zero output and is most sensitive when the inputs are 90° out of phase:

$$\frac{dV_{IF}}{d\Delta\phi} = V_{\max} \sin\Delta\phi \qquad \text{Volts/rad} \tag{5}$$

(NB: The mixer's output flips polarity when its input undergoes a 180° phase change due to the magic tee. However, sensitivity is unaffected).In order to calculate the maximum attainable sensitivity of the double balanced mixer, the signal to noise ratio of the device needs to be computed. The power output of a mixer depends on the input power and the conversion loss. The input power is limited by the mixer's IP3 and the conversion loss is determined by manufacturing considerations. The third intercept point (IP3) describes the maximum input power the mixer can accept before non-linear effects become important.

The Eclipse Microwave J2012ML double balanced mixer has an input response of 2-12 GHz and an output response 0-2 GHz, and thus is suitable for use in this system. Its IP3 is unspecified but its nominal input power is 10 dBm and its conversion loss is 6 dB at 12 GHz. For an input power of 12 dBm which is only slightly higher than the nominal input and so should remain linear, the output power should be 6 dBm. For a 50 Ω line this results in $V_{\max}$ = 0.446 V and thus a sensitivity of 0.466 V/radian when the inputs are 90° out of phase; changing the units equates to 7.79 µV/milli-degree.

This can be compared with the expected noise floor of the mixer in order to estimate the minimum phase measurement attainable. The Johnson noise (V_{JN}) of a device is expressed in volts as: $V_{JN} = \sqrt{4k_B TRB}$

where k_B is the Boltzmann constant, R is the line impedance, T is the temperature and B is the bandwidth multiplied by 1.57. The factor of 1.57 is included as it represents that low pass filters are not brick wall filters but have a roll off in their frequency response. For a bandwidth of 30 MHz (which would allow 6 measurements during the high power pulse,) at 300 K the Johnson noise is 6.24 µV, suggesting that the mixer could measure phase differences down to 0.8 milli-degrees.

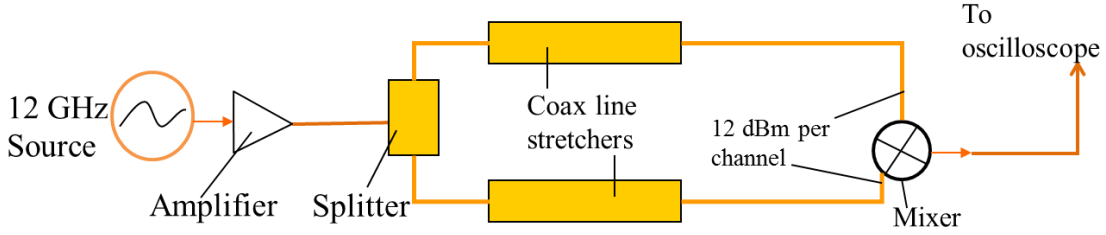

Figure 9 shows the experimental setup used to test the mixer response.

Figure 9 shows the apparatus used to test the mixer response. The 12 GHz source is a CTI PDRO-14XX low phase noise oscillator with output power 14dBm. A mini-circuits AVA-183A+ wideband amplifier was used to increase the output to 19 dBm. The splitter used was a Mini-Circuits ZX10-2-126+ Wilkinson splitter. Due to the losses in the splitter, line stretchers and coaxial cables, the power entering the mixer was 12 dBm per channel. The line stretchers were adjusted to attain the maxima and minima of the mixer's output on the oscilloscope. These were found to be 0.33 V and −0.362 V respectively, giving a phase sensitivity of 6.04 µV/milli-degrees. This agrees with theory to around 20%, the discrepancy most likely caused by a higher conversion loss than expected. The DC offset is a common feature of all mixers, due to diode imbalance and the measured offset agrees within an order of magnitude with that of theory [15]:

$$|V_{DC}| = (4.5)10^{\frac{LO-IS-30}{20}}$$

Where *LO* is the power into the oscillator port in dBm and *IS* is the isolation between the LO and IF ports in dB. Thus for 12dBm input and *IS*=25 dB (from datasheet of mixer) we expect a DC offset of 32mV and measure 16 mV. The measured offset corresponds to a phase measurement offset of 2.65°. This is not a problem as the phase measurement of the mixer is still linear to within 356 ppm at this offset. Non-linearity only increases to 5% at 30°, by which point the linear, digital phase detector will have taken over the measurements.

15. Phase Measurement Sensitivity

The low voltage output of the mixer (6.24 µV) is not a usable signal and needs to be amplified before measurement by an ADC or digital oscilloscope. Due to the high gain and bandwidth (30 MHz) required, the Analogue Devices AD8099 was used as it has a 1.5GHz gain bandwidth product. The datasheet specifies that the op amp has a flat frequency response up to around 20MHz at a gain of 20. Figure 10 shows how two amplifiers were used in tandem to achieve a gain of 473. This maps the mixer's noise floor of 6.24 µV to 2.95 mV on its output, which is easily readable on an oscilloscope.

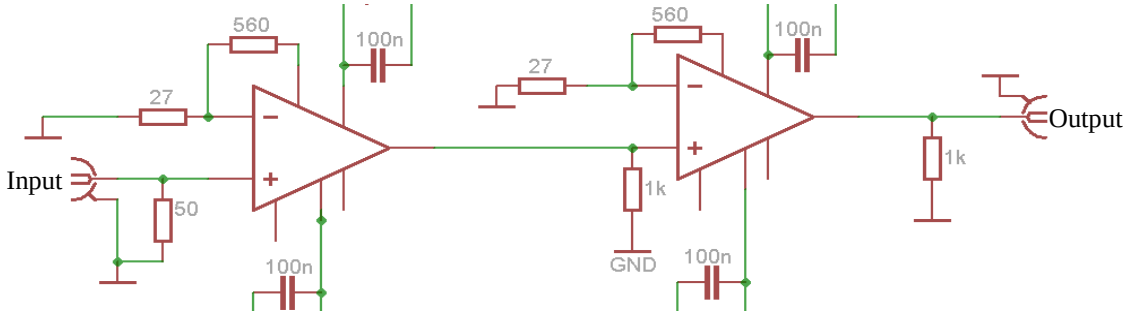

Figure 10 shows the circuit schematic of the high speed amplifier. Two AD8099 op amps are attached in series in the non-inverting configuration.

Due to the large bandwidth, careful consideration needs to be given towards the noise performance of the amplifier. This is because the noise voltage is proportional to the square root of the bandwidth. By keeping the resistances used low and choosing the AD8099 which has a low input noise voltage (V_N) of 0.95 nV/$\sqrt{Hz}$ and an input current noise (I_N) of 5.2 pA/$\sqrt{Hz}$, the noise of the system is minimised. Table 3 calculates the noise spectral density (*NSD*) of a single amplifier stage with a gain, *g* of 21.7. The calculation considers the Johnson noise of each of the feedback resistors, the input current and voltage noise of each of

the inputs and how these relate to the output. The final step is to add all of the contributions together in a quadrate sum.

Table 3 Noise spectral density contributions

Noise calculations	*NSD (V/rtHz)*	*Formula*
Feedback resistor (560Ω) to output	3.05E-09	$\sqrt{4R_{560}k_BT}$
Inverting resistor (27Ω) to output	1.45E-08	$g\sqrt{4R_{27}k_BT}$
Input resistor (50Ω) to output	1.98E-08	$g\sqrt{4R_{50}k_BT}$
Input current noise- to output	2.91E-09	$gI_N\left(R_{560}{}^{-1}+R_{27}{}^{-1}\right)^{-1}$
Input current noise+ to output	5.65E-09	gI_NR_{50}
Input Noise voltage at output	2.07E-08	gV_N
Total NSD for first OP-AMP	**3.28E-08**	Quadrature sum of above

The RMS voltage noise output of the whole system is calculated by multiplying the calculated NSD by the gain of the second stage and the square root of the bandwidth. For a bandwidth of 30 MHz the total noise output of the amplifier is 6.14 mV.

The amplifier was tested with 0 V input and the output attached to an oscilloscope. The amplifier had a high output offset of more than 80mV. Pin 5 on the AD8099 serves a special function of reducing the input offset current by a factor of 60 at the expense of increasing the input current noise by a factor of 2 (this has been accounted for in the above table). Pin 5 was activated and the output offset voltage dropped to 30mV accompanied by a small increase in the voltage noise. The voltage noise rise was small because of the relatively low resistances used in the feedback loop. The measured RMS noise output was 5.1 mV, agreeing with the calculated result to within 20%.

During testing it was noted that that the output offset voltage varied notably with temperature. This means the amplifier will have to be temperature stabilised to a high degree. A method of avoiding temperature stabilisation is to use another op amp in the negative feedback loop. If there is a temperature shift and the main op amp's offset voltage changes, the offset is cancelled by the voltage offset shift of the other op amp in the feedback loop [16]. This should be avoided however, as it will introduce large noise contributions.

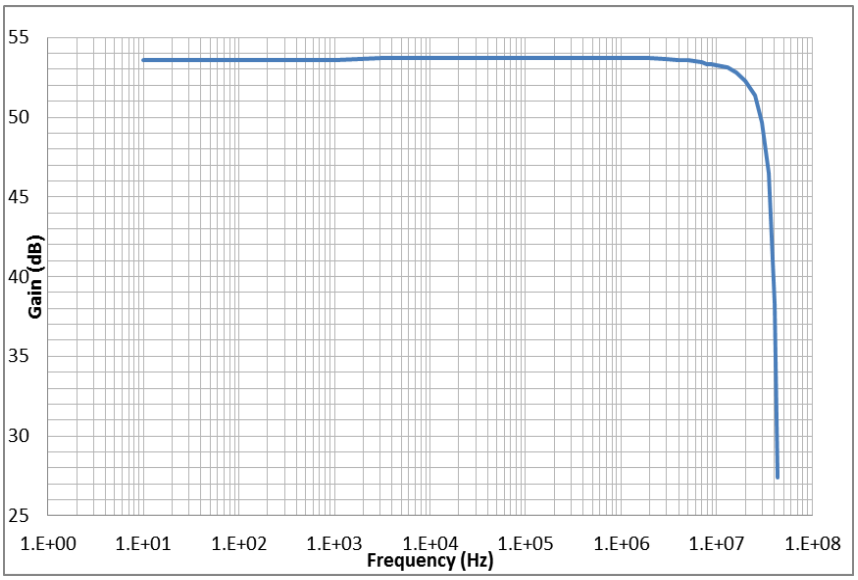

Figure 11 shows the frequency response of the amplifier with a dB-log scale.

The frequency response of the amplifier was then tested using a function generator and oscilloscope. The frequency response shown in figure 11 shows a 0.1dB flatness up to 5MHz and a -3dB cut off point at 30MHz. The frequency roll off after 30 MHz is very steep; explaining the 20% discontinuity between the noise calculation and measured noise, due to the fact that that the roll off factor of 1.57 assumed in the previous calculation was too large.

By combining the response of the amplifier with the sensitivity of the mixer, the phase sensitivity of the whole system can be obtained. The RMS noise at the output of the amplifier is 5.1 mV, which when referred to the input is 11.8 µV (divide by the gain). From the measured sensitivity of the mixer (6.04 µV/milli-degree), it is shown that the RMS sensitivity of the mixer and amplifier system is 1.79 milli-degrees. The amplifier's output saturates at about 4 V, limiting the dynamic range of the system to ± 1.4 degrees. In the final system this will be increased as a high resolution ADC will be used. The noise floor of 1.79 milli-degrees will be mapped onto the least significant noise free bit on the ADC. For a 2 V pk-pk, 13-bit ADC the least significant bit occupies a voltage of 0.244 mV, meaning a gain of 20.7 would map 1.79 milli-degrees onto it. This would result in a dynamic range of ± 8.00 degrees and a non-linearity of 0.3 %.

To assert that the real world system gives the same sensitivity, the amplifier was attached to the mixer in the setup shown in figure 9 and voltage measurements obtained (figure 12).

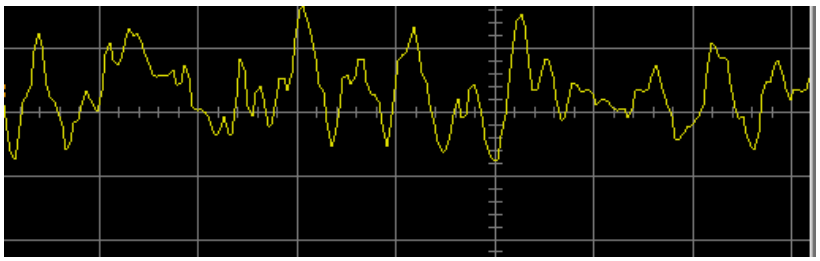

Figure 12 shows amplifier voltage output. The vertical scale is 2.88mV/milli degree, i.e. 3.47 milli-degrees per division. The horizontal scale is 50 ns per division.

The results shown in figure 12 show that the system responds as expected, and on the short time scale of the measurement (0.5 µs), there are no obvious external pick-ups or perturbations. Figure 13 shows how the system responds over a longer time period of 100 seconds.

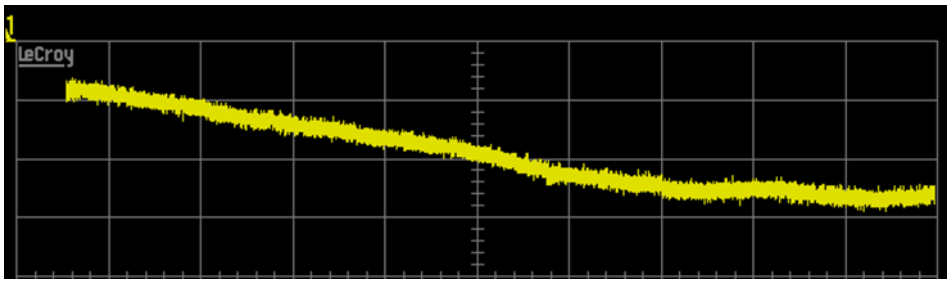

Figure 13 shows the voltage output of the amplifier. The vertical scale is 2.88mV/milli-degree, i.e. 34.7 milli-degrees per division. The horizontal scale is 10 s per division.

Over the longer time period of 100 seconds it is clear that long term drift is an issue. The figure shows a total drift of 80 milli-degrees, four times the maximum allowance, with the fastest drift rate being about 9 milli-degrees every ten seconds. The main source of drift is movement in the coaxial cables, causing path length variations. A solution would be to remove the cables altogether and mount all the components on a single PCB. This approach is discussed in section 18. A second source of drift is the temperature dependence of the DC offset of both the amplifier and mixer. Placing these devices in a temperature stabilised enclosure would solve this issue.

16. Digital Phase Detector Hardware

The previous section shows that the phase sensitivity of the mixer is at the required milli-degree level. It also shows some of the limitations of the system, such as DC offset, non-linearity of the measurement at large phase offsets and long term drifts. The digital/linear phase detector circumvents these issues as they display high linearity over the full 360° range and a high thermal stability. The linear phase detector will be used for calibration of the mixer and for phase drifts which are above the dynamic range of the mixer.

The HMC439 is a digital phase frequency detector that compares the zero-crossings of the RF waveform in order to measure the phase difference. The transistors in the phase detector are not fast enough to operate at 12 GHz so the 12 GHz signal is mixed down to 1.3 GHz using a double balanced mixer and a 10.7 GHz source. The 10.7 GHz source is locked to the same reference as the 12 GHz source to ensure that no phase drifts are introduced. The current prototype system is shown in figure 14.

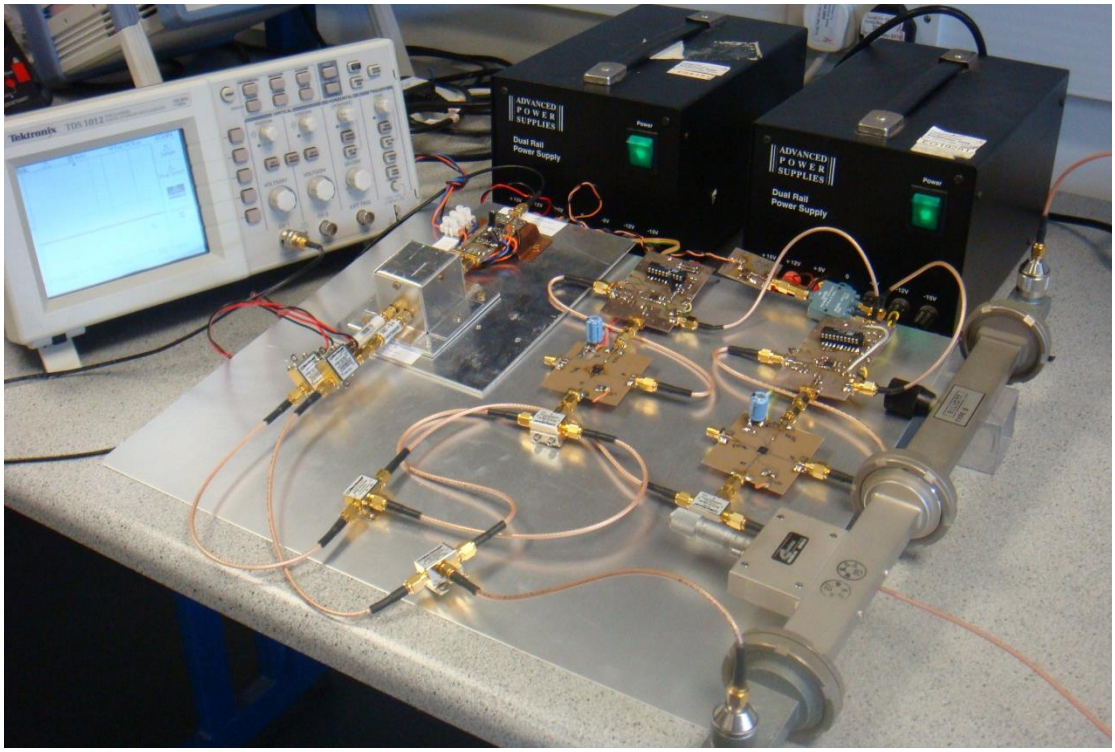

Figure 14 shows the digital phase detector set up.

The two square PCB's with large blue capacitors contain Hittite HMC735LP5 VCO's, producing the 12 GHz and 10.7 GHz signals and are phased locked to a 10 MHz local oscillator via ADF4113 PLL controllers. The two oscillator signals are split with Mini-Circuits ZX10-2-126+ splitters and mixed down by two Mini-Circuits ZX05-153LH-S$^+$ into two separate 1.3 GHz signals. One of the 12 GHz signals is passed through waveguide phase shifters before being mixed down to allow for phase adjustments and calibration. The mixed down signals are filtered and amplified before their phase is compared by the digital phase detector, whose output is amplified by an op amp with a bandwidth of 1 MHz.

The system was tested and has a sensitivity of 63°/V at the output. Touching the cables lightly resulted in a phase deviation of 0.63°. Long term drift was typically ± 63 milli-degrees over tens of seconds.

17. Phase Measurement System

The phase measurement electronics will combine a double balanced mixer, a digital phase detector and a digital processor to record the measurement. The double balanced mixer will provide the high sensitivity needed to resolve milli-degrees at 12 GHz, while the digital phase detector will provide a larger dynamic range and a linear response, useful for calibration of the mixer. Power meters will also be included because the mixer's phase sensitivity is proportional to the input amplitude. Wilkinson splitters will be used to send the signal to the phase detectors and power meters as shown in figure 15. The signals from the phase detectors and power meters are digitised and fed into the digital signal processor (DSP). The DSP measures the relative RF path length and corrects for it via the DAC's and phase shifters.

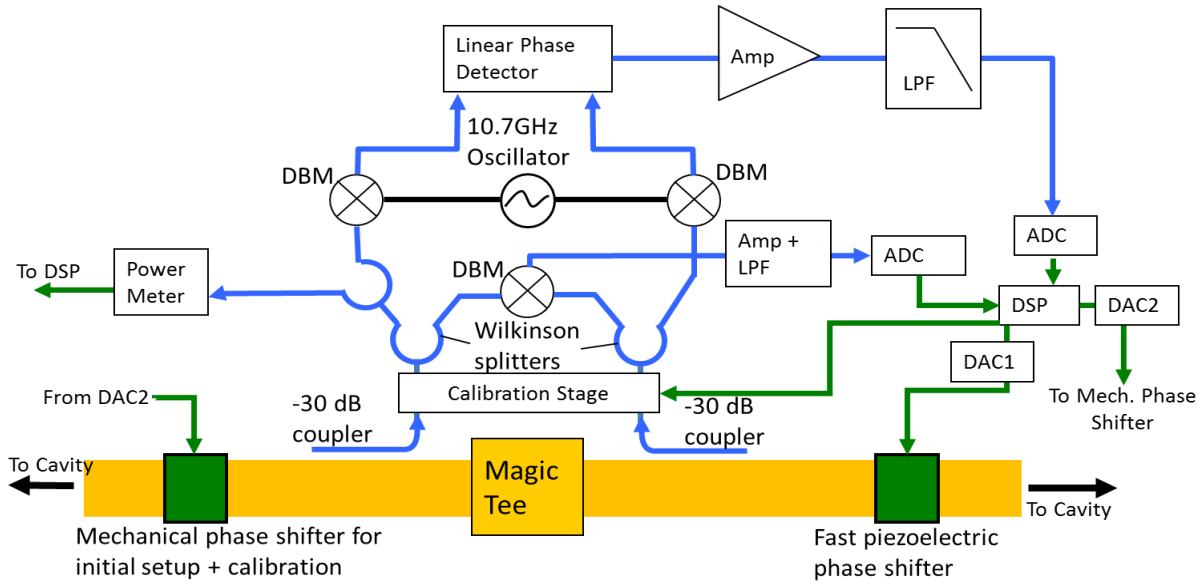

Figure 15 shows a schematic diagram of the phase measurement electronics.

The calibration stage contains a separate switchable 12 GHz source and mechanically and digitally controlled phase trimmers (figure 16). The mechanical phase trimmers are adjusted until the double balanced mixer's inputs are in quadrature. An automatic calibration is then performed by switching to the internal 12 GHz source and adjusting the digital phase trimmer, while mapping the mixer's output to that of the linear phase detector. The dynamic range of the digital phase trimmer is chosen such that the mixer's output amplifier is not saturated. The power level of the internal source is also varied to calibrate the phase sensitivity of the mixer against changes in input power level.

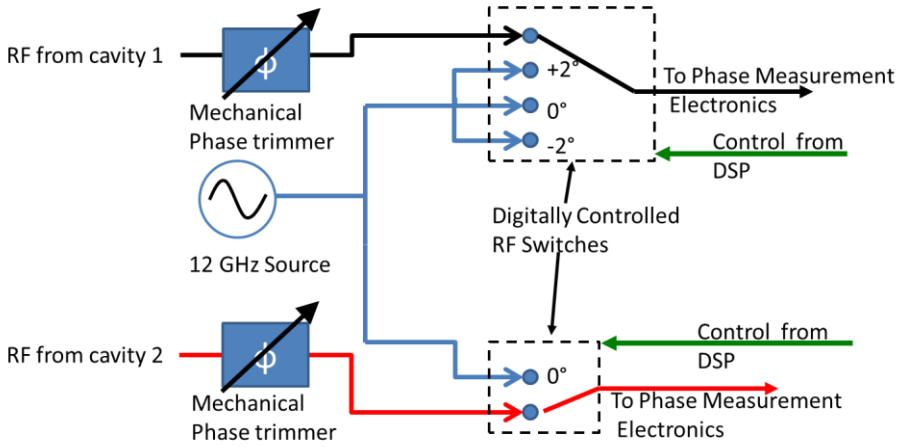

Figure 16 shows a schematic diagram of the calibration stage. A similar scheme was used by Alexandra Andersson at CTF3 [17].

18. Front End LLRF PCB

To counteract much of the slow phase drift observed in the double balanced mixer and digital phase detectors, the flexible coaxial cables connecting the various components together must be stabilised or removed. This is achieved by placing all of the components on a single PCB.

The board layout for the design has been completed and is shown in figure 17. To further increase the stability of the system the PCB will be placed in a temperature controlled, acoustically damped enclosure.

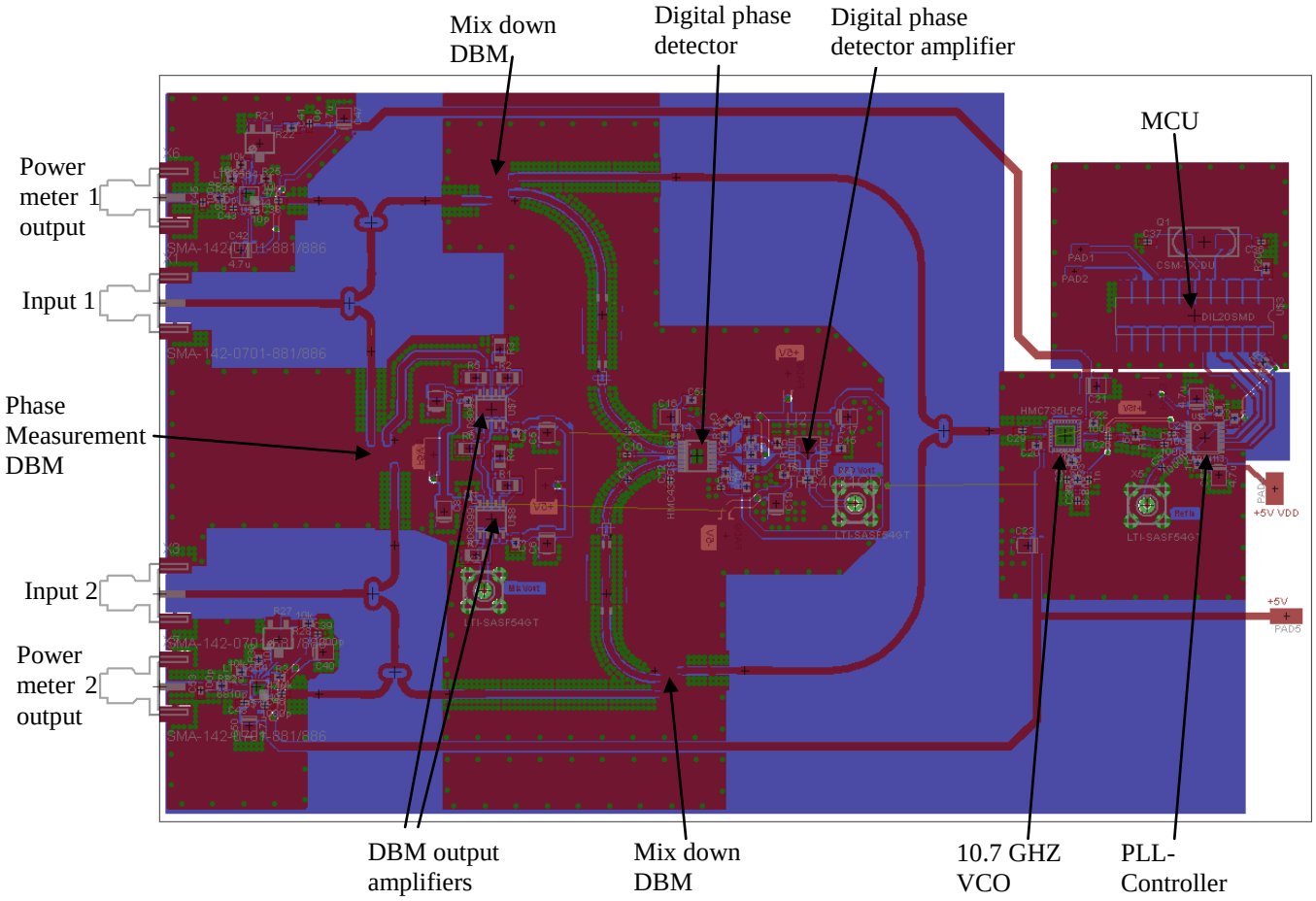

Figure 17 shows the board layout of the phase measurement electronics.

As part of the design, Wilkinson splitters have been developed using CST microwave studio and will be directly routed onto the PCB. At 12 GHz the splitter has a total loss of -3.3 dB, an isolation of -20.5 dB and a VSWR of 1.1 at port 1. The Mini-Circuits ZX10-2-126+ splitter (used in the previous experiments), has a total loss of -3.5 dB, an isolation of -19.9 dB and a VSWR of 1.7 at port 1. The simulated performance of the splitters matches or betters that of the Mini-Circuits ZX10-2-126+, showing that this design is adequate for use on the LLRF front end PCB.

The system is currently being manufactured and tested.

19. Validation Experiments

The phase synchronisation requirement for CLIC is beyond the level where we can be confident of successfully meeting it. At this early stage it is important to devise experiments that will indicate how difficult it will be to achieve synchronisation at the required level. The experiments also need to open research avenues for improving phase stability. An essential experiment is to determine the stability of a representative RF path length for the distribution system under power and over differing time scales. The time scales of interest are

- the bunch train length (156 ns)
- the inter train period (20 ms, acoustic vibrations)
- a few seconds - minutes (thermal expansion)
- a day (tides)

A second essential experiment is to determine the phase stability of a cavity at full power with its couplers. At the same time it is appropriate to determine breakdown rates in a realistic crab cavity structure at the planned gradient.

The expected outcomes from these experiments are that the gradient will be achieved once surface preparation has mastered. There will be no significant issues with the stability of the cavity itself. Drift of the phase advance through the RF distribution system will be large for simple designs and a program of development will need to be undertaken to minimise drift and correct residual errors. The waveguide distribution experiment can of course be staged. Initially tests can be done at low power looking at measurement accuracy. Low power measurements will identify the effect of tides, thermal fluctuations and vibration. A typical experimental arrangement is shown in Figure 18.

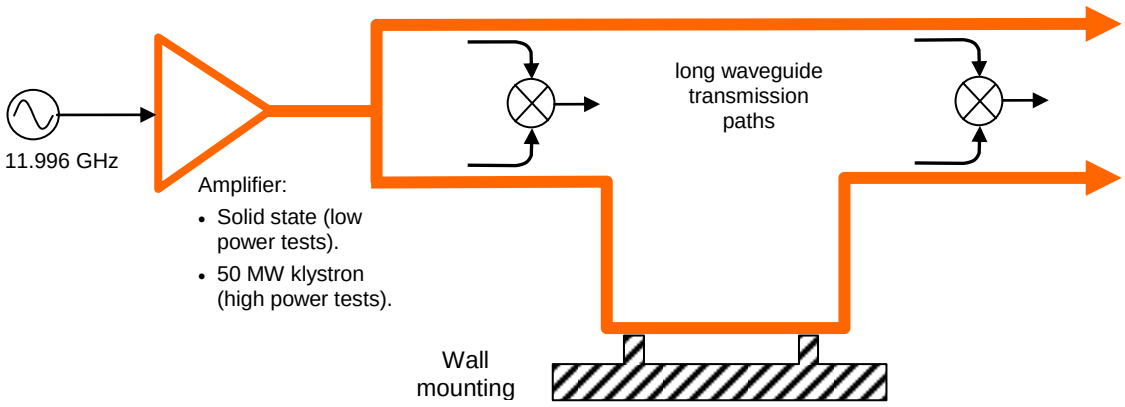

Figure 18 Waveguide stability experiments

At some stage high power measurements are needed for a full assessment of thermal effects. For low power tests the waveguide would be thermally isolated to reduce rates of dimensional change. Measurement at two locations allows the effect of the splitter to be determined. Differing paths allow the effects of wall (tunnel) movement to be assessed.

20. Digital Sampling

The data from the digital phase detector, amplitude detectors, power meters and the double balanced mixer needs to be sampled digitally during the intermediate measurement pulses and control decisions taken before the next main pulse. Maximum flexibility is achieved by implementing a bespoke system. The system we have developed uses a Digital Signal Processor (DSP) rather than a Field Programmable Gate Array (FPGA). There is no benefit from using an FPGA as the available processing time is milli-seconds hence the flexibility of a DSP is preferable. Figure 4 shows three control systems. The fast feedback control system that manages the klystron amplitude and phase during the 156 ns pulse with respect to the local reference will be analogue and hence will not have a DSP. Any feed forward element that becomes necessary would be encompassed by adjusting the phase reference.

Intelligent signal processing (with DSPs in this case) are needed for the control systems that keep the waveguide paths identical and manage the beam to RF synchronisation. The DSP that manages RF to beam synchronisation needs to:-

- receive timing and phase information on the outward going bunch train
- calculate and set the required phase shift between the master oscillator and the cavities
- generate the envelope for the klystron RF pulse
- trigger and adjust modulators
- record phase variations during a pulse train
- compute and implement any feed forward phase adjustments required during a pulse.

The recording of phase variations during a pulse might be done by comparing the cavity RF output with the beam pick up, however more information becomes available, although possibly at a reduced accuracy, if beam and cavity are separately compared with a local oscillator as shown in Figure 4. The hardware under evaluation for sampling the phase of the RF during the pulse is illustrated in Figure 19. The signals from the two power meters, digital phase detector and the DBM from the front end LLRF board are present on the input of fast ADCs (black lines).

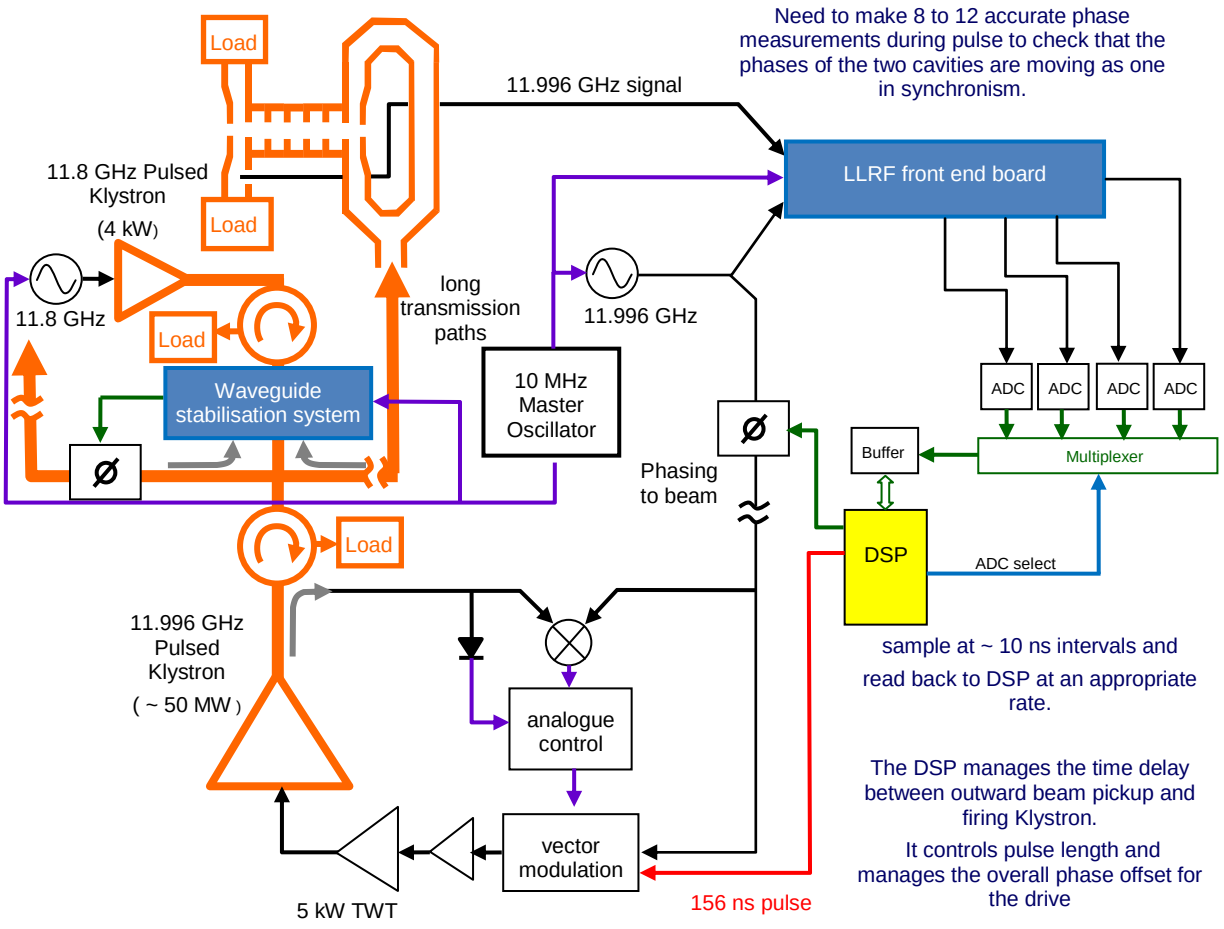

Figure 19 Digital sampling and control

The waveguide stabilisation system contains a LLRF front end board, calibration stage, digital sampling electronics and a DSP for control (as described in section 17).

The specific implementation we have developed is illustrated in figure 20. The choice of ADC was the 16 bit 105 MBPS Analog devices AD9640. When the clock is applied to its input the device starts pipeline sampling with each input value appearing on the output 13 clock cycles later. The DSP (a Texas Instruments C6745,) is limited in the speed at which it can acquire data and cannot read 16-bits at 105MSPS into its memory. To overcome this obstacle a 16 sample, 16-bit buffer board was developed using an array of 16 D flip-flops to store the data before it is read off by the DSP. In this way 16 samples can be taken during the klystron pulse.

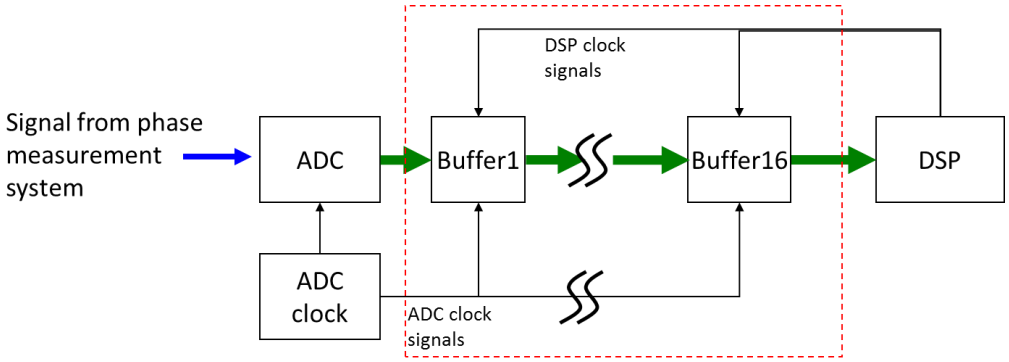

Figure 20 shows a schematic of the buffer board. There are 16 single D flip-flops connected in a serial fashion.

During the klystron pulse the ADC clock shifts each sample along the buffer train until the buffer is full. The data is then read off by the DSP, using its own clock/pulsed signal. To test the buffer board, a baseboard was developed to house a single ADC, buffer board and the TI C6745 DSP. A program was written to store 16 samples onto the buffer and read them off onto the DSP, which sent the data to a PC via USB. In this way the digital sampling system was tested and found to have a noise free resolution of 12.8 bits.

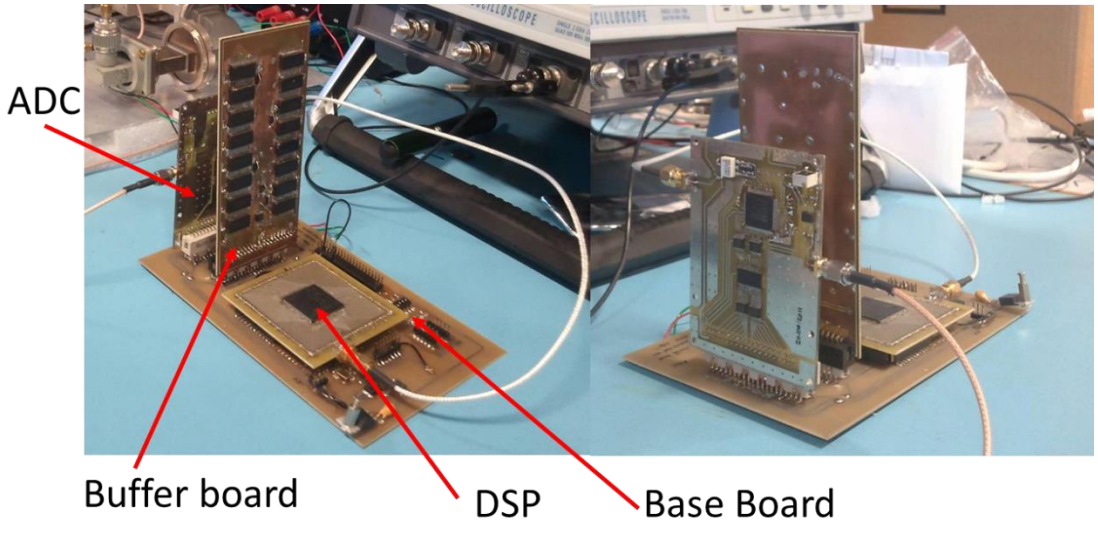

Figure 21 shows the completed digital sampling system.

The base board pictured has a further 20 GPIO pins that can be used to control the various switches and read data from lower bus width devices. In order to connect all of the 16-bit ADCs and DACs that will be needed to measure and control the phase stabilisation system, a

multiplexer board needs to be used. There is currently a multiplexer prototype board but the noise performance is poor. A redesign of the power and ground planes of the ADC and DAC boards should solve the problem.

Commercial digital oscilloscopes could have been used; however it is useful to have one's own dedicated system. In this way data can be taken into the DSP controller very quickly rather than waiting for handshaking on a commercial instrument, also one's own choices of ADC speed and resolution can be made. Typically we clock the ADC at either 40 or 80 MSPS hence the RF pulse is sampled at either 25 ns or 12.5 ns intervals.

21. Conclusions to Part 1 (CLIC)

This study has identified the key technical challenges with regard to synchronising the CLIC crab cavities. It has set out a baseline design of both a high power RF system and a low power RF system having the potential to meet the phase synchronisation specification. It has undertaken an analysis of waveguide stability requirements based on thermal effects. It has set out specifications for the measurement systems. The key features of the proposed baseline system are:-

- short, high group velocity deflecting cavities making cavity amplitude insensitive to beam loading.
- one high power klystron driving both cavities removing sensitivity to klystron jitter
- copper coated invar waveguide on damped mounting and in a controlled temperature environment.
- semi-continuous measurement of RF transmission paths to the cavities from the power splitter by operating the high power transmission system as an RF interferometer in between accelerator pulse trains.
- feed forward control of high power transmission path lengths using high power phase shifters (note that these phase shifters only require a small dynamic range).

A LLRF system that will allow phase drift measurements to be made on CLIC crab cavities and the associated high power RF distribution system during short pulses has been designed, prototyped and tested. The LLRF system has an intelligent processing capability to enable testing to be managed. Intelligent processing is required eventually for automated setup and feed forward correction where required. The LLRF system described provides both beam to cavity synchronisation and stabilisation of RF path lengths in conjunction with intermediate measurement pulses.

Future work will focus on testing the concepts, the cavities and RF distribution system components at increasing powers using the CTF3 test facility.

22. Introduction to Part 2 (LHC)

The planned LHC luminosity upgrade [18] will utilise compact crab cavities [19] to vary the alignment of proton bunches at two interaction points so as maximize the integrated luminosity by maintaining the luminosity at a constant level throughout the bunch lifetime [20]. Peak instantaneous luminosity is achieved when bunches are in perfect alignment. At the large luminosity foreseen for the LHC upgrade, the luminosity then decays rapidly by proton burning. This natural evolution is very demanding for the dynamic range required from the physics detectors that becomes prohibitive. To overcome this difficulty, crab cavities can be used to initially reduce the luminosity by inducing a crabbing angle at the interaction point, and reduce it progressively as the luminosity decays by proton burning. The attractive aspect of this solution using crab cavities is that, due to details of the beam dynamics, the integrated luminosity is increased with respect to the situation where the luminosity is maximized and then decays naturally. For the proposed optics, the initial luminosity would be reduced by a factor between 2 and 4 by the crabbing scheme. The proposal for the luminosity upgrade is thus to have a sufficient crabbing angles at IP1 and IP5 together with a precise control to decrease it during the physics data taking. The crabbing scheme should further not induce any emittance blow-up of the beams, and be fail-safe in case of beam loss or power or equipment breakdown.

A crab cavity is a deflection cavity operated with a 90^{o} phase shift [21] so that a particle at the front of a bunch gets a transverse momentum kick equal and opposite to a particle at the back of a bunch while a particle at the bunch centre gets no transverse momentum kick. The overall effect is the application of an apparent rotation rate to the bunch.

The simplest scheme for controlling crabbing angles is a global scheme as was applied at KEKB [22]. In such a scheme only one crab cavity is required per ring. Once the bunch has a crabbing angle it rotates one way and then the other way with respect to its nominal path as it passes through successive quadrupoles. For a given transverse voltage in the crab cavity the maximum angle of rotation depends on the focusing properties of the lattice. The lattice is arranged so that bunches have the ideal crabbing angle at the IPs. For the LHC, studies have indicated that having the bunch oscillating about its axis along the entire circumference is unacceptable, due to collimation control restrictions. For this reason the current proposal is to use a local crabbing scheme [18].

For a local scheme crab cavities would be located before and after IP1 and IP5 so that the crab rotation can be removed. Both crab cavities are positioned in a location of relatively high beta function, so as to minimise the kick that must be applied to get the appropriate rotation at the IP and to cancel the rotation after the IP. After the bunch leaves the crab cavity it will be rotating about its geometric centre. As it passes through the quadrupoles the rate of rotation will change. The R_{12} parameter determines the amount of rotation at the IP for a given transverse kick at the preceding crab cavity. As the bunch continues through the lattice after the IP, successive focusing quadrupoles will reverse the direction of rotation. A second crab cavity can remove the angular rotation, however for the bunch to become re-aligned with the bunch trajectory the crab cavity must be placed in a position where the rotating bunch comes into alignment with the trajectory.

23. Proposed LHC Luminosity Upgrade Beam Parameters

The parameters for the proposed luminosity upgrade are continually evolving as differing optical schemes are assessed. Key beam parameters used here have been taken from reference [23] (section 7.3). This reference does not give details of the optical deck and the beta function at the crab cavity location. Here we take the beta function at the crab cavity to be 4000 m based on the decks described in [24]. Rows 1-15 of Table 1 below give nominal parameters for current LHC operation and two proposed parameter sets for the proposed luminosity upgrade. Row 16 is a naive luminosity estimate based only on geometrical factors. Rows 17 to 20 give the Crab Cavity parameters to be used in our analysis.

Table 1 LHC Beam Related Parameters

	Parameter	Unit	Nominal	Scenario 1	Scenario 2
1	Beam energy (E_o)	TeV	7	7	7
2	Particles in bunch (N)		1.15×10^{11}	2.0×10^{11}	3.3×10^{11}
3	Bunch charge (q)	C	1.84×10^{-8}	3.2×10^{-8}	5.28×10^{-8}
4	Bunches (n)		2808	2808	1404
5	Bunch repetition frequency (f_{rep})	MHz	40	40	20
6	Bunch separation	Ns	25	25	50
7	Crossing angle (θ_c)	μ rad	300	420	520
8	β^*	M	0.55	0.2	0.2
9	β at crab cavity	M		4167	4167
10	R12 (crab cavity to IP)	M		28.9	28.9
11	ε_s	eV	2.5	2.5	2.5
12	ε_n	M	3.75×10^{-6}	2.5×10^{-6}	3.0×10^{-6}
13	Bunch length (σ_z)	M	0.0755	0.0755	0.0755
14	Bunch width at IP (σ_x)	M	16.6×10^{-6}	8.2×10^{-6}	9.0×10^{-6}
15	Piwinski parameter		0.68	1.94	2.2
16	Peak Luminosity		1.3×10^{34}	8.5×10^{34}	8.7×10^{34}
17	Crab cavity Frequency (f)	MHz	N/A	400	400
18	Required Crab Transverse Kick	MV	N/A	6.07	7.52
19	Max. bunch offset at cavity (Δx)	μm	N/A	236	259
20	Beam loading at max. offset	kW	N/A	15.4	17.3

Crab cavity requirements depend on the lattice and its position within it. Assumptions on the beta function here are based on a 2011 lattice described in reference [23]. In this reference the crab cavity is positioned 150 m before the IP at a position where the beta function β_{crab} = 4167 m. The beta function at the IP will be taken as β_{ip} = 0.2 m as suggested by [23] but less aggressive than the 0.15 m used in [24]. A key parameter for determining the voltage in the crab cavity is the R_{12} which relates an angular deflection of the trajectory at the crab cavity x'_{crab} to a transverse offset at the IP $x_{ip} = R_{12} x'_{crab}$. This parameter is evaluated from knowledge of the beta function between the IP and the crab cavity. When there is a 90^o phase advance between the crab cavity and the IP then R_{12} is given by the expression:

$$R_{12} = \sqrt{\beta_{ip}\beta_{crab}} = 28.9\,\mathrm{m}\,.^{1} \tag{23.1}$$

A choice on the Crab cavity frequency has been determined as 400.8 MHz [29].

From reference [26] the peak transverse voltage $V_\perp$ required in the crab cavity to give the correct angular deflections of protons crossing the cavity near the time that the on axis magnetic field is zero is determined by:

$$V_\perp = 0.5\frac{E_o}{R_{12}}\frac{c}{\omega}\theta_c = 0.5\times\frac{7\times10^{12}}{28.9}\times 0.119\times 0.000420 = 6.07\,\mathrm{MV} \tag{23.2}$$

where θ_c is half the crossing angle and E_o is the beam energy, this expression is evaluated for Scenario 1 in table 1. For Scenario 2 the required kick is 7.52 MV.

The peak power requirement P_{cc} for the crab cavity depends primarily on the maximum anticipated bunch offset Δx at the crab cavity [27]. Beam to beam interactions at the IP may drastically reduce beam lifetime if the bunches are not accurately aligned. The maximum offset at the crab cavity ($\sigma_{y(crab)}$) is related to the maximum offset at the IP ($\sigma_{y(ip)}$) through the beta function. If as above there is a 90^o phase shift between the crab cavity and the IP then the sizes are related by the expression[2]:

$$\sigma_y(\mathrm{crab})/\sigma_y(\mathrm{ip}) = \sqrt{\beta(\mathrm{crab})/\beta(\mathrm{ip})} = \sqrt{4167/0.2} = 144 \tag{23.3}$$

This expression is derived from the maximum offsets of individual particles.

If we suppose that under the optimum conditions for physics the bunches have a maximum transverse offset at the IP of $\Delta y = 0.2\,\sigma_y$ then the maximum offset for optimum conditions at the crab cavity is 236 μm for scenario 1 and 259 μm for scenario 2. It is likely that the phase advance between the crab cavity and the IP will be different to 90^o and in the direction that increases offsets at the crab cavity. This means that the potential offsets given above are minimum estimates. It is likely that one would actively steer the beam through the crab cavities so that deviations larger than these values never occur. This would be needed for both machine protection and beam lifetime.

The crab cavity power requirement is simply the electric current multiplied by the longitudinal voltage. The longitudinal voltage depends on offset Δx. Taking q as the bunch charge, f_{rep} as

[1] Note that this expression is readily derived from the equation for the Betatron motion [15] and this equation is explicitly written out later in this text as equation (5.5).

[2] This result is also derived from the equation for the Betatron motion

bunch repetition rate and applying Panofsky Wenzel theorem to relate the longitudinal voltage to the transverse voltage, the power requirement is determined as:

$$P_{cc} = q f_{rep} V_z = q f_{rep} \Delta x \frac{\omega}{c} V_{\perp} \sim$$
$$3.2\times10^{-8} \times 4\times10^{7} \times 2.36\times10^{-4} \times 0.119 \times 6.07\times10^{6} \quad = \quad 15.4\,\text{kW} \tag{23.4}$$

The current compact crab cavity designs are expected to deliver a maximum kick between 3MV and 5MV. On this basis the initial RF layout will be planned to accommodate 3 cavities to provide the initial crab kick on each beam and then another 3 cavities are required to remove the kick. If the cavities achieve a kick exceeding 4.0 MV then two cavities provide sufficient voltage kick. With three cavities the power requirement per cavity becomes ~ 6 kW, hence the RF power source is likely to be a solid state solution.

24. LHC Crab Cavity LLRF System Issues

There are a number of issues that will be considered in this report with respect to the operation of the LHC crab cavities and their Low Level RF (LLRF) system:

1. phasing cavities to the arrival of beam bunches,
2. phasing cavities to each other,
3. the relationship between spectral noise, beam – beam interactions and bunch lifetime,
4. amplitude control so bunches get the correct rotation at IP,
5. amplitude control to perfectly eliminate rotation after the IP,
6. elimination of spectral noise at dangerous frequencies with respect to bunch lifetime,
7. transverse kick following a quench of a superconducting crab cavity,
8. detected failure of LLRF system to regulate power amplifier.

The low level RF system (LLRF) will interact with the 12 crab cavities associated with each IP location.

24.1 Cavity Synchronisation

A crab cavity is a deflection cavity operated with a 90^o phase shift. If the phase of a crab cavity is not exactly 90^o from the phase of maximum possible deflection then the bunch rotates about a point that is not its geometrical centre and hence gains an average deflection at the IP. If two bunches that should collide have differing average deflections then their axial centres miss each other at the IP. If the two crab cavities on opposing beam lines are synchronised to each other, but not necessarily to the bunch arrival times, then the deflection to opposing proton bunches are identical and hence head on collision is maintained. Note that the quadrupoles that provide focusing at the IP correct for position offsets at the crab cavities but not transverse momentum errors.

Poor phase synchronisation gives transverse position offsets Δx at the IP [26]. When all the particles have the same offset and this offset is small then the luminosity reduction factor S is given as $S = \exp\left(-\frac{\Delta x^2}{4\sigma_x^2}\right)$ where σ_x is the transverse bunch size at the IP and errors Δ are measured bunch to bunch (not bunch to centre). For offsets that have a Gaussian distribution the r.m.s. luminosity reduction factor S_{rms} is determined by:

$$S_{rms}\left(\Delta x_{rms}\right) = \sqrt{\frac{1}{\sqrt{2\pi}}\int_{-\infty}^{\infty}\frac{1}{\Delta x_{rms}}\exp\left\{-2\left(\frac{\Delta x}{2\sigma_x}\right)^2\right\}\exp\left(-\frac{\Delta x^2}{2\Delta x_{rms}^2}\right)d(\Delta x)}$$

Performing the integration gives:

$$S_{rms}\left(\Delta x_{rms}\right) = \left\{1+\left(\frac{\Delta x_{rms}}{\sigma_x}\right)^2\right\}^{-\frac{1}{4}}\sqrt{\frac{1}{\sqrt{2\pi}}\int_{-\infty}^{\infty}\frac{1}{\Delta x_{rms}}\exp\left(-\frac{\varphi^2}{2\Delta x_{rms}^2}\right)d\varphi} = \left\{1+\left(\frac{\Delta x_{rms}}{\sigma_x}\right)^2\right\}^{-\frac{1}{4}} \quad (24.1)$$

The principle approximation in (24.1) is to neglect the beam-beam interaction effects.

A crab cavity to cavity timing error Δt gives a transverse bunch position error at the IP of $\Delta x = \theta_c c \Delta t$. Phase errors in degrees are related to timing errors using $\Delta\phi = 360 f \Delta t$ where f is the RF frequency. Most accelerator control systems easily achieve phase control at the level of 0.1 degrees, this corresponds to a timing error of 0.7 ps (at 400 MHz) and hence a position error of 0.1 μm. This is a very small transverse error compared to the transverse bunch size of 8 μm hence no special effort is required to synchronise the cavities to each other for the sole purpose of maximising luminosity. The important issue is whether a random position error of 0.1 μm combined with bunch - bunch interactions at the IP increase the transverse growth rate of the bunch.

24.2 Luminosity Loss for Amplitude Errors

For angular errors $\Delta\theta_1$ and $\Delta\theta_2$ of bunches from their nominal paths on the two colliding beam lines respectively, the luminosity reduction factor S is determined as

$$S \cong \left(1 + \left[\frac{\sigma_z \left(|\Delta\theta_1| + |\Delta\theta_2| \right)}{2\sigma_x} \right]^2 \right)^{-\frac{1}{2}} \tag{24.2}$$

Note that when the sum amplitude error on one beam line is opposite to the sum amplitude error on the opposing beam line then bunches are parallel when they collide but not in line with the nominal path. In this situation luminosity is reduced just as if the amplitude errors give an increased angle between the colliding bunches.

The angular bunch error $\Delta\theta_i$ caused by an amplitude error ΔV_i on one cavity is determined as $\Delta\theta_i / 0.5\theta_c = \Delta V_i / V_o$ where V_o is the voltage needed for the correct crabbing angle hence (24.2) becomes

$$S \cong \left(1 + \left[\frac{\sigma_z \theta_c}{2\sigma_x} \frac{\left(|\Delta V_1| + |\Delta V_2| \right)}{2V_o} \right]^2 \right)^{-\frac{1}{2}} \tag{24.3}$$

Well-designed state of the art RF systems can typically maintain amplitude in CW superconducting cavities to within one part in 10^4. For this level of amplitude control variation in luminosity is undetectable. Were the amplitude control accuracy to be reduced to one part in 10^3 and for bunches receiving opposite rotation then equation (24.3) predicts luminosity losses for the scenarios 1 and 2 given in table 1 as 1.9×10^{-6} and 2.4×10^{-6} respectively. Amplitude errors would need to rise above 5% before luminosity loss would be of any concern.

The problem with amplitude control comes with accumulated errors. The revolution frequency of a bunch is 11.424 kHz and for each revolution a bunch will see twelve crab cavities, three to crab at each IP and three to uncrab at each IP. After ten seconds a bunch will have interacted with a cavity 1.32 million times. If amplitude errors are uncorrelated then net amplitude error after one second with be 1148 times the average error on one interaction. Consideration of particles which are off centre and off energy is more difficult, an analysis is given in section 5.

25. Cavity Control Simulations and Cavity Quench

The power requirement of a cavity depends on its loaded Q factor and its stored energy. The loaded Q factor is usually adjusted for maximum power transfer but might be adjusted to

provide a set bandwidth. One might fix a minimum bandwidth to make phase and amplitude control easier in the presence of Lorentz de-tuning during cavity filling or at cavity quench.

For a superconducting cavity the maximum power requirement is determined by maximum beam loading. Beam loading is zero for an on axis bunch passing through a crab cavity, it is negative for a bunch passing one side of the nominal axis in the crabbing plane and it is positive for a bunch passing on the other side. The maximum offset used for simulations in this section will be 0.25 mm which is representative of the values in Table 1. In order to achieve this value and to guard against large offsets one might choose to insert active dipoles to steer the beam through the crab cavities. The power source for the crab cavity must be sized to maintain the correct amplitude for the largest likely offsets during normal running. The largest power requirement in Table 1 is 17.3 kW however for the simulations performed, the input power will be matched to the cavity at its design voltage for the maximum bunch offset.

The compact crab cavities are being designed to provide a kick of 3.27 MV and the 4-Rod Crab Cavity (4RCC) has a stored energy of 1.89 J when providing this kick. From (23.3), the power requirement is proportional to transverse voltage hence for a kick of 3.27 MV the maximum power requirement is 8.34 kW. For perfect power transfer at this power level, the 4RCC cavity requires an external Q factor of 5.71×10^5. Its bandwidth is then 702 Hz. Initial simulations therefore assume an external Q factor of 5.70×10^5 and a maximum forward power of 8.5 kW

The following sub-sections model the phase and amplitude response of the 4RCC in the presence of disturbances for a standard digital LLRF system acting on IQ components of the cavity voltage [28].

The noise spectrum generated by the LLRF controls system is also calculated by computing a Fast Fourier Transform (FFT) of the cavity voltage. The noise spectrum includes phase and amplitude noise. The bunches sample the cavity voltage at the revolution frequency hence a FFT of the cavity voltage includes times when there is no bunch in the cavity. An analysis is also made of the sum voltage acting on particles circulating at frequencies close to the revolution frequency.

Before a Crab cavity is inserted into the LHC, a full investigation how its performance effects beam stability and emittance control is required. Such an investigation is currently being planned on the SPS. An advantage of using a digital control scheme as described is its flexibility with respect to varying parameters, filters and injected noise as part of a systematic investigation.

The obvious choice for the Crab Cavity LLRF system is to use the existing system used for the LHC acceleration cavities with minor modifications [29]. As this option has been considered separately to the current project it is not explicitly reported here. An important feature of the LLRF system for the acceleration cavities is its ability to damp Synchrotron oscillations [30]. This is not a requirement for the Crab Cavity LLRF as the acceleration LLRF would continue to perform this function. Importantly the Crab Cavity LLRF must not affect the beam in a manner that acceleration LLRF can no longer damp Synchrotron motion. Neither must it affect the beam in a manner that the transverse damping system can no longer damp the betatron motion.

25.1 RF Cavity Model

The 4RCC performance considers its operating dipole mode at 400.8 MHz and interactions with the Lower Order Mode at 375.2 MHz and the first unwanted dipole mode at 436.6 MHz.

The model has been adapted from the model described in [24] making it applicable to circular machines.

The time evolution of a cavity mode obeys the same differential equation as a parallel lumped circuit. Where a cavity has the potential to resonate at a number of frequencies each mode adds a voltage contribution at the coupler and hence the modes are modelled as parallel resonators in series as shown in Figure 25.1.

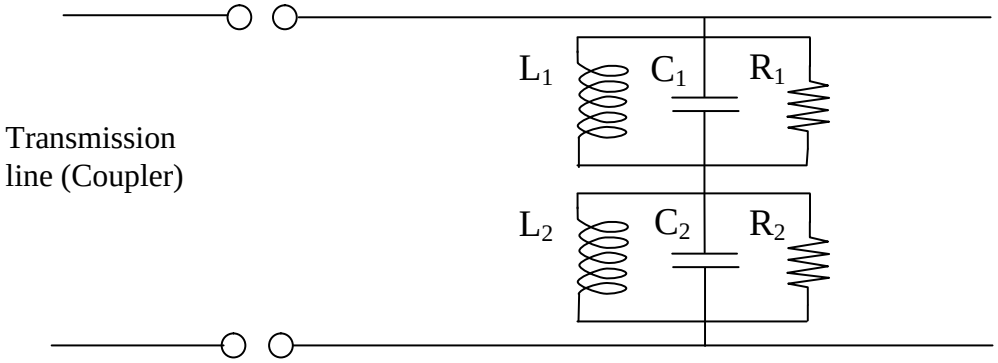

Figure 25.1 Equivalent circuit with two modes

At the terminal the voltage in the transmission line of the coupler must equal the voltage in the lumped circuit. Along the entry transmission line (i.e. the power coupler) the voltage and current satisfies the equation

$$\frac{\partial^2 V}{\partial z^2} = L_{wg} C_{wg} \frac{\partial^2 V}{\partial t^2} \tag{25.1}$$

where C_{wg} is the capacitance per unit length and L_{wg} is the inductance per unit length.

For a source of angular frequency ω the voltage along the entry transmission line is given as

$$V(z,t) = \mathcal{F} \exp\{j(kz - \omega t)\} + \mathcal{R} \exp\{-j(kz + \omega t)\} \tag{25.2}$$

where $k = \omega\sqrt{L_{wg} C_{wg}}$, $\mathcal{F}$ is the amplitude of the forward wave and $\mathcal{R}$ is the amplitude of the reflected wave. The current on the transmission line is therefore given as:

$$I(z,t) = \frac{1}{Z_{wg}}\left[\mathcal{F} \exp\{j(kz - \omega t)\} - \mathcal{R} \exp\{-j(kz + \omega t)\}\right] \tag{25.3}$$

Where:

$$Z_{wg} = \sqrt{\frac{L_{wg}}{C_{wg}}} \tag{25.4}$$

If the terminal between the cavity and the waveguide is at z = 0 then the current in the transmission line equals the sum of the currents through the equivalent circuit components of each series resonator (i.e. we get an equation for each resonator / mode) hence

$$\frac{1}{L_i}\int V_i dt + C_i \frac{dV_i}{dt} + \frac{V_i}{R_i} = \frac{1}{Z_{wg}}\{\mathcal{F} - \mathcal{R}\}\exp(-j\omega t) \tag{25.5}$$

where V_i is the voltage for the i^{th} mode. With respect to the model in Figure 25.1, V_i is the voltage across one of the parallel resonators. From (25.2) and adding series voltages for each mode, the voltage at z = 0 which is the end of the entry transmission line is given by:

$$V = \sum_{\text{modes}} V_i = (\mathcal{F} + \mathcal{R}) \exp(-j\omega t) \tag{25.6}$$

Eliminating the reflected power between (25.4) and (25.5) gives:

$$\frac{1}{L_i}\int V_i dt + C_i \frac{dV_i}{dt} + \frac{V_i}{R_i} + \frac{1}{Z_{wg}} \sum_{j=1}^{N} V_j = \frac{2\mathcal{F}}{Z_{wg}} \exp(-j\omega t) \tag{25.7}$$

If the coupling to different modes is dissimilar, then Z_{wg} takes a different value for each mode.
This equation determines the modal voltages in the cavity as a function of the amplitude of the forward wave in the waveguide.

Defining the natural frequency of the i^{th} mode as $\omega_i = \frac{1}{\sqrt{L_i C_i}}$ then to evaluate Z_{wg} we write:

$$Q_{ei} = \frac{\omega_i U_{stored}}{P_{emitted}} = \frac{\frac{1}{2}\omega_i C_i V_i^2}{\frac{1}{2}\left(V_i^2 / Z_{wg}\right)} = \omega_i Z_{wgi} C_i \tag{25.8}$$

$$Q_{oi} = \frac{\omega_i U_{stored}}{P_{diss}} = \frac{\frac{1}{2}\omega_i C_i V_i^2}{\frac{1}{2}\left(V_i^2 / R_i\right)} = \omega_i R_i C_i \tag{25.9}$$

where U is an energy, P is for the power dissipation in the cavity.
Equations (25.8) and (25.9) give:

$$Z_{wgi} = \left(\frac{R_i}{Q_{oi}}\right)_C Q_{ei} \tag{25.10}$$

The suffix C is used to denote the circuit definition of R/Q, defining the loaded Q factor using:

$$\frac{1}{Q_{Li}} = \frac{1}{Q_{oi}} + \frac{1}{Q_{ei}} \tag{25.11}$$

The differentiation of (25.7) and using the preceding equations gives the well-known cavity equation for …..

$$\frac{d^2 V_i}{dt^2} + \frac{\omega_i}{Q_{Li}}\frac{dV_i}{dt} + \frac{1}{Q_{ei}}\omega_i \sum_{\substack{j=1 \\ j\neq i}}^{N} \frac{dV_j}{dt} + \omega_i^2 V = \frac{2\omega_o}{Q_e}\frac{d}{dt}\{\mathcal{F}\exp(-j\omega t)\} \tag{25.12}$$

In this equation ω is the RF frequency and ω_i is the angular frequency for the mode in a loss-less cavity, as yet beam loading has not been considered. For the LHC crab cavity there will be a number of couplers utilised to damp the unwanted modes. The model of Figure 25.1 only has one coupler shown and this is optimised for the operating mode. The couplers used to damp unwanted modes are best included by inserting an appropriate value for the intrinsic Q factor for the mode to be extracted.

For resonant systems where Q factors are greater than about 20 one does not need to solve (25.12) for the voltage at any instant, it is sufficient to solve for the amplitude and phase. More conveniently than solving for amplitude and phase we solve for in-phase (I) and quadrature (Q) components of the voltage. We denote the phase part with the suffix r and the quadrature path with the suffix I, writing:

$$V_m(t) = \{A_{mr}(t) + jA_{mi}(t)\}\exp\{-j\omega t\} \quad [3] \tag{25.13}$$

and making approximations consistent with slowly varying amplitude and phase, equation (25.12) becomes replaced with the two first order differential equations as follows:

$$\dot{A}_{mr} = -\frac{\omega_m}{4Q_{om}}\left(\frac{\omega_m^2}{\omega^2}+1\right)A_{mr} - \frac{\omega_m}{4Q_{em}}\sum_{j=1}^{N}\left(\frac{\omega_j^2}{\omega^2}+1\right)A_{jr} + \left(\omega_m^2-\omega^2\right)\frac{A_{mi}}{2\omega} - \frac{\omega_m}{\omega Q_{em}}\left(\dot{\mathcal{F}}_i - \omega\mathcal{F}_r\right) \tag{25.14}$$

$$\dot{A}_{mi} = -\frac{\omega_m}{4Q_{om}}\left(\frac{\omega_m^2}{\omega^2}+1\right)A_{mi} - \frac{\omega_m}{4Q_{em}}\sum_{j=1}^{N}\left(\frac{\omega_j^2}{\omega^2}+1\right)A_{ji} - \left(\omega_m^2-\omega^2\right)\frac{A_{mr}}{2\omega} + \frac{\omega_m}{\omega Q_{em}}\left(\dot{\mathcal{F}}_r + \omega\mathcal{F}_i\right) \tag{25.15}$$

The difference between solving (25.12) and the equations (25.14) with (25.15) is that one no longer needs lots of time steps per RF cycle. Typically we solve (25.14) and (25.15) with one time step per cycle and this is convenient with respect to applying beam loading effects from individual bunches.

Beam loading is incorporated by allowing the phase and amplitude of the cavity excitation to change in proportion to the image charge deposited in the cavity after the passage of the bunch. For a dipole mode the change is determined as:

$$A_r(\text{final}) = A_r(\text{initial}) + \frac{r_b\omega}{c}\omega\left(\frac{R}{Q}\right)_F q\cos\alpha \tag{25.16}$$

$$A_i(\text{final}) = A_i(\text{initial}) + \frac{r_b\omega}{c}\omega\left(\frac{R}{Q}\right)_F q\sin\alpha \tag{25.17}$$

where α is the phase angle between the bunch passing the centre of the cavity and the initial RF phase of the cavity, q is the bunch charge, r_b is the offset of the bunch. Here the R/Q is defined as $\left(\frac{R}{Q}\right)_F = \frac{|V_L(r)|^2}{2\omega U\left(\frac{r\omega}{c}\right)^2}$ where the cavity voltage V_L includes transit time effects.

25.2 The RF Controller

A digital LLRF system typically measures in phase and quadrature components cavity fields and controls each component to a set point by varying the in phase and quadrature components

[3] When modes adjacent to the operating mode have a large frequency separation a better approximation can be made by using a differing centre frequency ω for each mode equation (25.13). For the results in this report the influence of the adjacent modes is minimal and hence these more complicate equations are not required.

of the RF input. Importantly the system is described by two first order differential equations rather than one second order differential system. The optimum controller for a first order system with random disturbances is a PI controller. As beam loading for a crab cavity is unpredictable some component of the controller typically requires a PI controller. This can be enhanced with feed forward to improve control where disturbances are anticipated. A property of digital LLRF system is they might act with a significantly delayed action of >0.5μs. Differential terms are not required in first order systems to provide damping. Differential terms also cause problems when there is noise on the measurement.

For the multi-mode cavity an issue with the controller is whether by clever filtering one can determine the amplitude and phase of the operating mode. If one can and with reference to the envelope equations (25.14) and (25.15) one can determine the driving components as:

$$\mathcal{F}_r\left(t+t_{delay}\right)=c_{pr}\left(V_{sp}-A_{1r}\right)+c_{ir}\left(\frac{\omega}{2\pi}\right)\int_{-\infty}^{t}dt\left(V_{sp}-A_{1r}\right) \qquad (25.18)$$

where t_{delay} is the time it takes to measure the error and adjust the amplifier output and V_{sp} is the set point voltage required in the cavity. The set point for the phase of a crab cavity is zero hence the set point for the out of phase part of the voltage A_{1i} is also zero.

In the multi-mode software model we assume that the operating mode cannot be measured directly and instead one measures a time average of amplitude and phase of all the modes in the cavity where differing modes have a differing weighting according to their coupling to the output coupler.

The ratio of the integral coefficients c_i to the proportional coefficients c_p have been chosen such that the response immediately after rapid cavity filling at full power is slightly under-damped. This choice generally gave a slightly better control of amplitude and phase during the bunch than critical damping.

25.3 Hardware Concept Appropriate to Model

With respect to the model it is useful to have a concept for the hardware that might be associated with the model. The simplest option is independent control of each crab cavity where each controller is required to achieve a set point voltage at zero phase. One would of course want each system to report back on whether the set point voltage was achieved or not so that set points can be adjusted to ensure that crabbing and un-crabbing continue to balance.

The hardware for each cavity requires knowledge of the beam phase, measurements of the cavity I and Q voltage components and an input for the cavity voltage set point. The hardware for each cavity would have an oscillator locked to the local beam phase, a detector for cavity I and Q voltages, a controller and an amplifier chain as illustrated in Figure25.2. The controller utilised for the simulations is a simple PI controller that acts independently on I and Q components. It is likely that the controller would include a comb filter to selectively reject dangerous frequencies [29]. It achieves this by feeding back the measured signal at a precise frequency in anti-phase.

Our model does not consider how accurately the voltage controlled oscillator (VCO) follows the beam phase. In principle however this problem can be solved by the same approach as for the cavity. This is because the phase detector is a special case of the IQ detector, the Phase Lock Loop (PLL) filter is a fast controller and the VCO behaves like a cavity. As the VCO is

not subject to the same perturbations as the crab cavity then one expects noise generated in this part of the system to be much smaller than noise coming from the cavity and its control system.

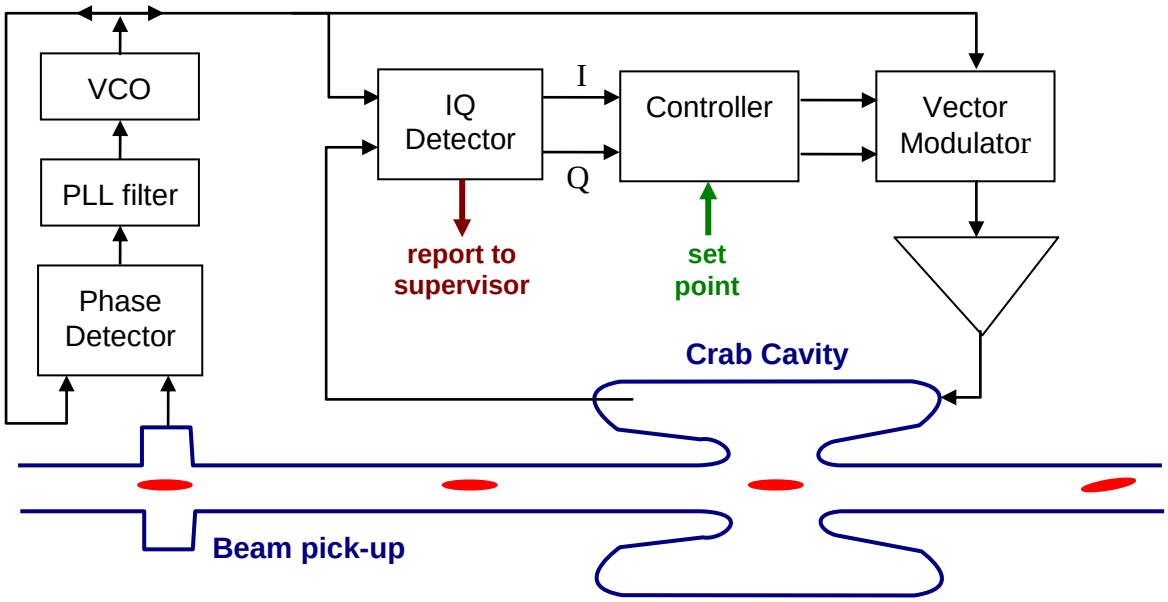

Figure 25.2 Conceptual Hardware for Model Should include MO feed

The VCO can be analysed using the same equations as used for the cavity without beam loading i.e. (25.14), (25.15), (25.18) and (25.19) but this is not done here. The loop filter is invariably a simple network of capacitors and resistors to form a PI controller with no additional delay from digital computation.

25.4 Noise Spectrum Computations

In a passive RF system spectral noise can arise from the source that drives the system and can be increased by vibration, temperature fluctuation and the control system. The superconducting cavity will operate at 1.8 K and is likely to have a bandwidth close to 1 kHz hence it filters input noise and adds no significant level of thermal noise.

The transfer function for the cavity acting as a filter is given by:

$$\frac{V_{out}}{V_{in}} = \frac{1}{1 + j\frac{1}{\delta\omega}\left(\omega - \frac{\omega_o^2}{\omega}\right)} \tag{25.19}$$

where $\delta\omega$ is the cavity bandwidth, ω_o is the cavity centre frequency and ω is the driving frequency, in this case an unwanted noise frequency. Dangerous frequencies for the LHC beam will be combinations the Synchrotron frequency at 23 Hz, the betatron frequency at 3.4 kHz and the revolution frequency at 11.245 kHz taken together as offsets from the cavity frequency at 400.8 MHz. With a cavity bandwidth of 1 kHz none of the dangerous frequencies will be so heavily damped that they can be neglected.

Taking Sine and Cosine FFT of the voltage in the cavity reveals the noise spectrum that is caused by disturbances and the control system itself. An input to the model includes cavity vibration and hence this is a major contributor to noise. The voltage needs to be sampled for a time period of normal operation after cavity voltages have stabilised and when the beam is

present. The LLRF simulations in this report needed for computing spectra have been run for 600 bunch trains allowing a sampling period for the FFT of 50 ms.

The sampling interval typically started once the cavity voltage had stabilised at the set point with beam present. Quenches and cavity faults were introduced after the FFT sample had been collected. In sections 25.4 to 25.6 the voltage was averaged over sufficient cycles so that the FFT was performed on just 2^{16} = 65536 data points. The averaging was done to limit output rather than computation time. For the computations presented here the frequency interval for the FFT was 11.7 Hz and noise at frequencies above 1.5 MHz was removed by the averaging. System disturbances for the model were set at frequencies well above 11.7 Hz so that the output properly encompasses the control system performance.

As the FFT is taken for a fixed period of ~50 ms then it contains all the spectral components associated with a pulse of this length. The results presented have had the spectrum of a 400.8 MHz pulse at the set point voltage lasting the full sampling period subtracted from the raw spectrum.

Spectral results presented under the description of the Noise Spectrum are computed as the Sine and Cosine Fast Fourier Transforms (FFT) of $\sqrt{A_r^2 + A_i^2}$ and normalised with respect to the set point voltage. The normalisation factor is $\frac{2}{N V_s}$ where N is the number of data points and V_s is the set point voltage.

Because the actual cavity field is $\sqrt{A_r^2 + A_i^2}\, e^{i\omega t}$ then the results are determined as single sided offsets from the carrier frequency.

For plotting, the Fourier coefficients are expressed as a power ratio. In order to get the spectral power density one would also need to divide by the frequency interval (11.7 Hz in this case). It is not appropriate to do this as the spectral peaks are very narrow. In order to get relative power in a spectral range one needs to add the Fourier coefficients in the range according to Parseval's identity.

Spectral results presented under the description of I and Q voltages are the absolute values of the Sine and Cosine Fourier coefficients of A_r and A_i and these are normalised by the set point voltage as described above. Result are expressed in dB as $20\log_{10}$(value). Where phase noise is given it is determined as the FFT of $\tan^{-1}(A_i/A_r)$ it is then normalised by a factor of $\pi/2$ and expressed in dB.

25.5 Model Input Parameters

A sequence of simulations have been undertaken. The parameters taken for the cavity have not been changed for the simulations and are listed as follows:

```
Number of cavity modes                  : 3
Operating mode order (1-dipole)         : 1
Operating mode centre frequency  (GHz) : 0.4008d00
Operating mode Q factor                 : 2.000d+09
Operating mode external Q factor        : 5.700d+05
Operating mode R over Q (Ohms per cell): 912.6
Mode 2 order                            : 0
Mode 2 centre frequency (GHz)           : 0.3752d+00
Mode 2 intrinsic Q factor               : 1.0000d+04
Mode 2 external Q factor                : 5.000d+06
Mode 3 relative pickup coupling         : 1.0d-01
Mode 2 relative beam coupling           : 0.136d00
Mode 3 order                            : 1
Mode 3 centre frequency (GHz)           : 0.4366d00
Mode 3 intrinsic Q factor               : 1.0000d+04
Mode 3 external Q factor                : 5.000d+06
Mode 3 relative pickup coupling         : 1.0d-01
Mode 3 relative beam coupling           : 0.0153d00
```

In this table the R/Q of mode 2 and 3 is determined by multiplying the relative mode beam coupling with the R/Q of the operating mode. The crab cavity will have a power coupler for the operating mode and HOM/LOM couplers for modes 2 and 3. The analysis only considers power transfer via the input power coupler. The action of the HOM and LOM couplers is included by reducing the intrinsic Q factors of those modes.

The software was written for multi-cell cavities where adjacent modes can influence the control of the operating mode. If the main pick-up were to have a 1 MHz band pass filter so that it does not see the LOM and the first HOM then these modes have no effect on the operating mode unless they are resonant with the bunch arrival frequency. The amount of pick-up is determined by the relative mode pickup parameter.

Results from the model have been computed for differing input parameters. The disturbance parameters are the beam offset, the bunch charge fluctuation, the microphonic detuning and bunch arrival time jitter. Charge fluctuations have a very small effect compared to beam offset and have been set at 1% for all the simulations. Only beam offsets of 250 μm and zero have been considered. The programme input allows offsets to be completely random or sinusoidal at a set frequency. Here a sinusoidal variation of offset at 5000 Hz has been used throughout.

A cavity vibration causing microphonic detuning has an amplitude and a frequency. Simulations to provide FFT output ran for 50 ms however the graphs for time domain response were typically created for shorter time intervals of just 3.5 ms. The microphonic frequency was taken at 2 kHz so that entire oscillations can be seen in the 3.5 ms output. The calculations can all be quickly repeated once the precise microphonic spectrum has been measured.

Calculations whereby the cavity detunes by 40 Hz which is about 1/20 of the bandwidth have been undertaken. One anticipates that the cavity can be made sufficiently stiff, so that microphonic detuning can be limited to this extent. At this level, the simulations show that

microphonic detuning has minimal effect for these parameters, however the results can be used to estimate the magnitude of the effect for differing parameters. As the cavity runs at constant voltage then Lorentz detuning is only an issue if the cavity quenches. Bunch arrival time jitter has been set to zero as the LHC RF systems are phase locked to the average bunch arrival time for a train.

25.5.1 Simulation 1 Results (No measurement errors)

The list of program inputs which include disturbances and LLRF parameters will be referred to as the LLRF input. This input for first simulations is shown below:

```
Master oscillator frequency (GHz)      : 0.4008d0
Bunch frequency (GHz)                  : 0.04008d00
Energy set point (Joules per cell)     : 1.89
Maximum Amp Power (Watts per cell)     : 8500.0
Maximum beam offset (mm)               : -0.250
1 for random offset 0 for periodic     : 0
Offset fluctuation frequency (Hz)      : 5000.0d00
Initial Bunch phase retard (degrees)   :  0.0
Bunch phase jitter (degrees)           :  0.0
1 for random charge fluc 0 for periodic: 0
Phase jitter frequency (Hz)            : 5000
Bunch charge fluctuation (fraction)    : 0.005
1 for random charge fluc 0 for periodic: 1
Charge fluctuation frequency (Hz)      : 5000
Bunch charge (Coulombs)                : 3.2e-8
Bunch train length (seconds)           : 86.90166e-6
Bunch train gap length (seconds)       :  2.02096e-6
RF advance time (seconds)              : 200.0e-6
Cavity freq. shift from microphonics Hz: 40.0
Vibration frequency of cavity  (Hz)    : 2000.0
Initial vibration phase (degrees, sin) : 0
Measurement phase error in degrees     : 0.0
Measurement amplitude error as fraction: 0.0
Delay for control system in seconds    : 0.5e-6
Control update interval in seconds     : 0.5e-6
Initial gain constant for controller   :  10.0
Amplifier Bandwidth                    :  5.0e6
Measurement filter bandwidth           : 10.0e6
Feed forward sum jump  (~1.2e6)        : 0.0e6
```

The parameter list includes measurement parameters, amplifier parameters and control parameters. The first simulation assumes no measurement errors in order to show control performance clearly. A delay of 0.5 μs has been assumed for the LLRF system response. As the cavity runs with a continuous wave (CW) then feed forward processes are not incorporated.

Later simulations will consider the cavity response when the beam arrives before the cavity is energised and controlled to a set point. Simulations 1 to 3 however start with an empty cavity, fill at full forward power (8.5 kW) and on reaching the set point they control the amplitude to 3.2705 MV corresponding to the energy set point of 1.89 J. Beam arrives after the cavity has settled, the settling time has been set to about 0.8 ms. The simulation continues running during

a sequence of either 24 or 600 machine revolutions each with bunches filling 2808 of the 3564 buckets according to the LHC filling scheme (*Time domain figures are for 24 revolutions with beam*). The fill time for the chosen parameters was 0.4 ms and the end time was typically 3.5 ms. A cavity quench is instigated during the 20th bunch revolution when 24 revolutions are being computed. The cavity voltage is shown on an expanded scale in Figure 25.3.

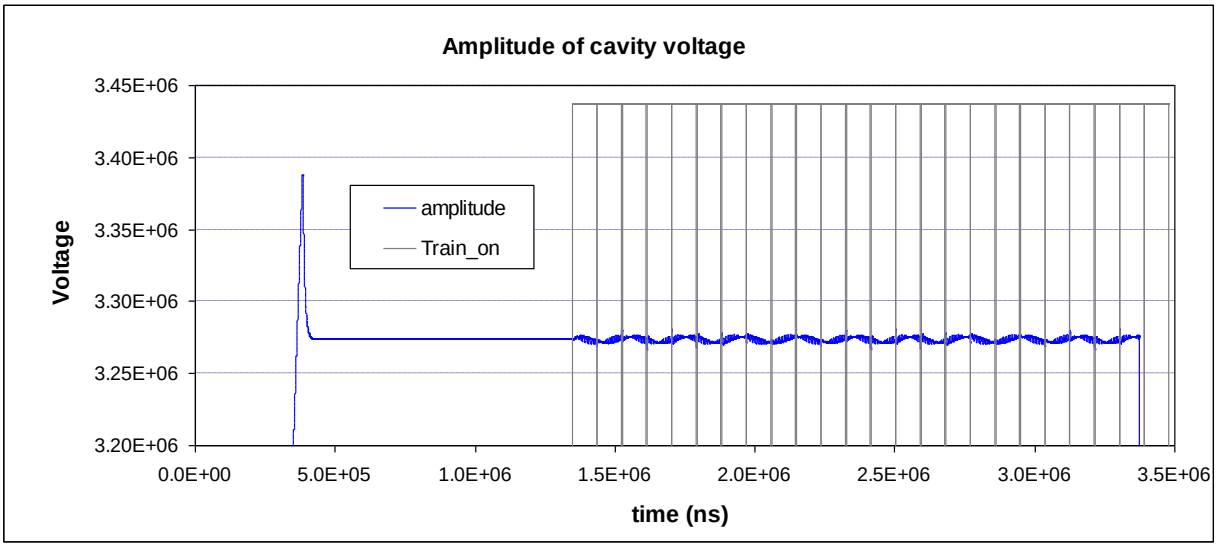

Figure 25.3 Cavity voltage during simulation with cavity quench at 3.075 ms - simulation 1.

The important questions to ask are how well the amplitude and the phase are maintained and what happens to the cavity kick during the quench. Figure 25.4 magnifies the amplitude fluctuations of Figure 25.3 between 1.8 ms and 2.1 ms. The underlining oscillation at 5 kHz comes from the frequency assigned to the bunch offset. There are small but sharp deviations in the amplitude corresponding to gaps in the LHC bunch train. The biggest deviation occurs for the gap left for LHC beam dump. These large deviations come at the machine frequency of 11.245 kHz. Anticipating that bunch offsets are unknown, feed forward control cannot work to remove the deviations. It should be remembered this simulation assumes no measurement errors, enabling reasonable control with peak voltage deviation at the 0.1% level.

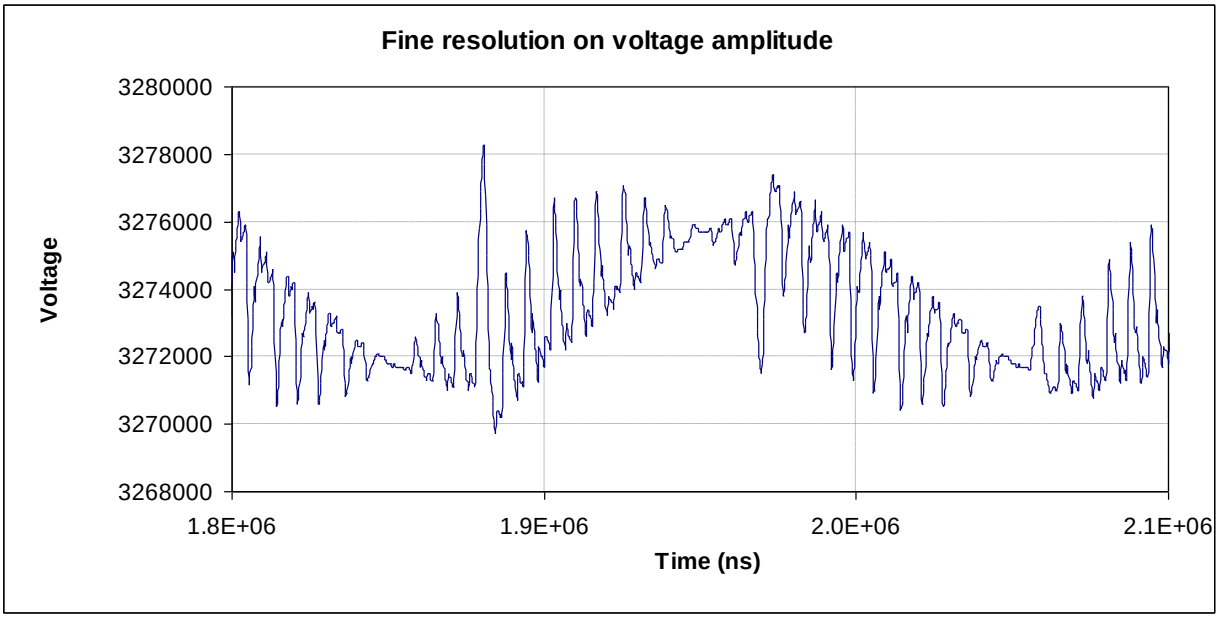

Figure 25.4 Fine detail on cavity voltage during simulation with cavity quench at 5.035 ms - simulation 1

The phase during the pulse is shown in Figure 25.5. Once the cavity has filled and before the quench, the peak phase error is only dependent on microphonic detuning. This was set at a level of 40 Hz RF detuning (cavity bandwidth ~ 0.7 kHz) and the mechanical oscillation was taken to be 2 kHz. The control system corrects the cavity phase to the level of +/- 3 milli-degrees

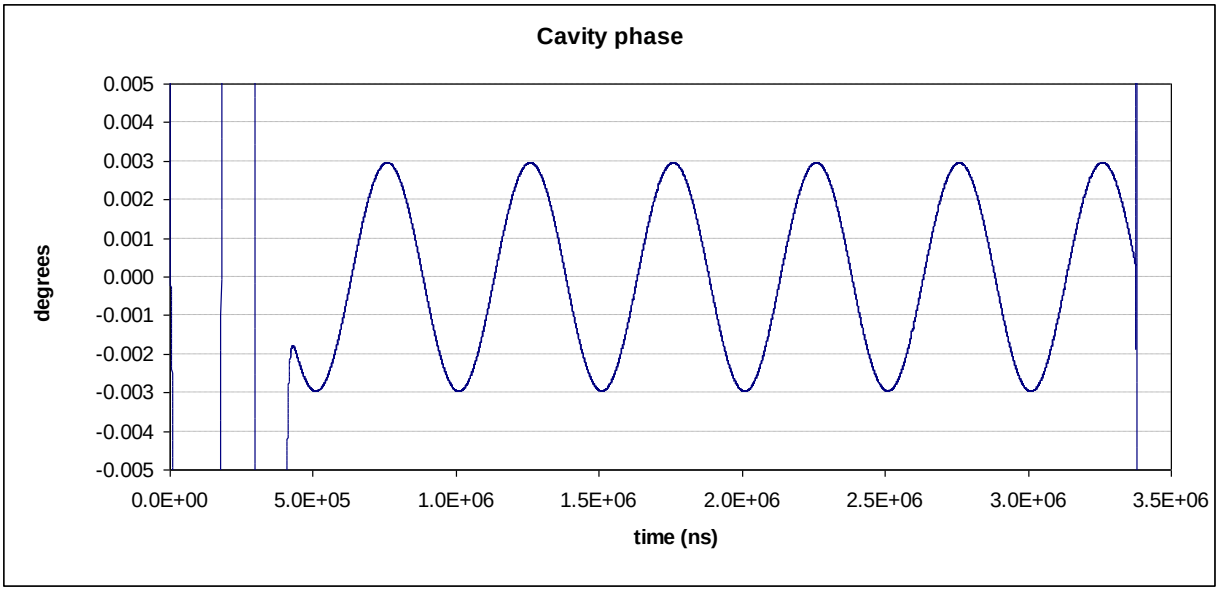

Figure 25.5 Cavity voltage during simulation during flat top - simulation 1

Figure 25.6 gives the power requirements during the simulation. In the absence of beam loading and microphonics the cavity requires 2577 W to maintain amplitude for the external Q factor of 5.7×10^5. An additional 35 W is required to compensate the 40 Hz microphonic detuning. The input power requirement is dominated by beam offset. Peak power is just short of the maximum amplifier power by virtue of the simulation offset being at the maximum design value.

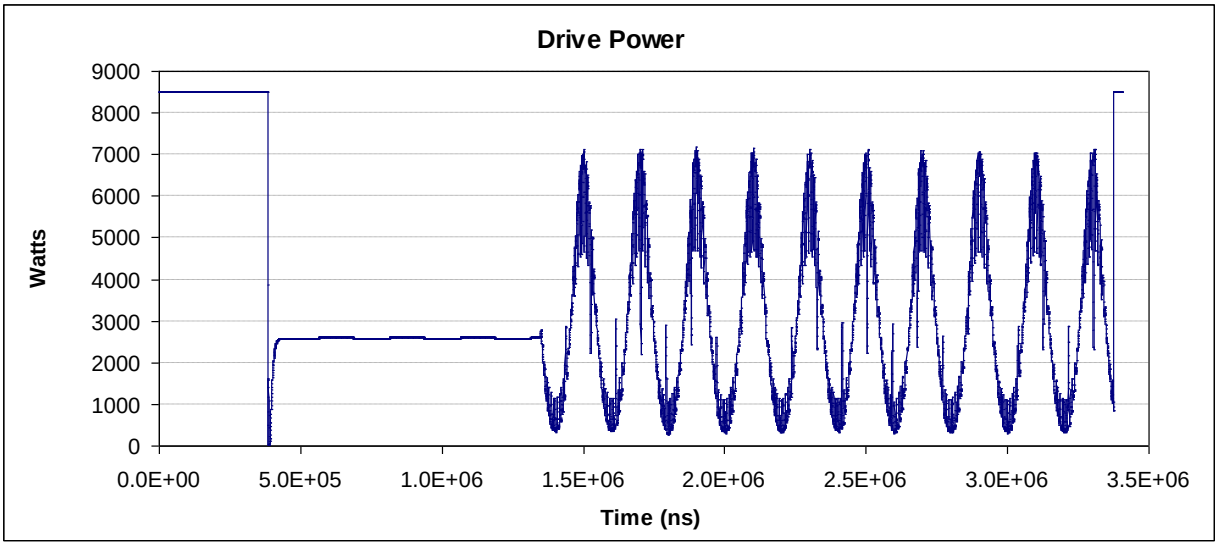

Figure 25.6 Cavity power during flat top - simulation 1

Figure 25.7 shows fine detail for the amplifier output. During the large gap in the LHC bunch train fill of 119 missing bunches associated with the LHC Dump Kicker rise time of 3 μs occurring at 1.88 ms the power requirement almost returns to level required for no beam as expected. Large power dips are seen for the 38/39 missing bunches associated with the LHC injection kicker and the 8 missing bunches for the SPS injection kicker.

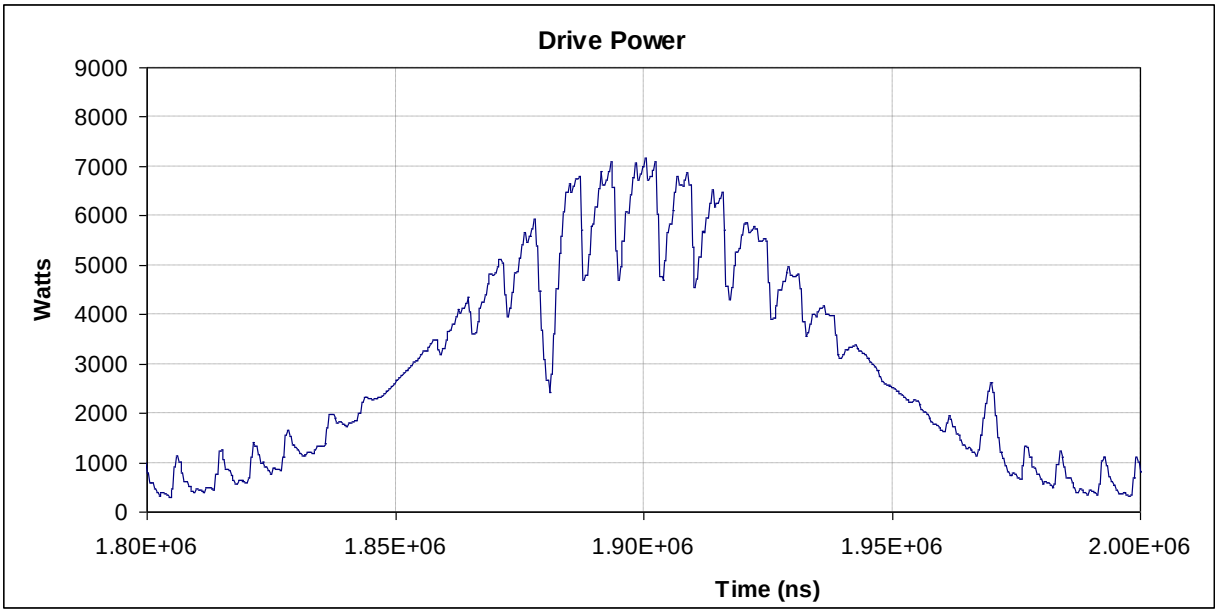

Figure 25.7 Fine detail on amplifier power - simulation 1

Figure 25.8 shows reflected power from the cavity. Initially during filling the voltage in the cavity rises linearly hence the energy rises quadratically. This means that as the cavity starts to fill there is almost 100% reflection of the forward power.

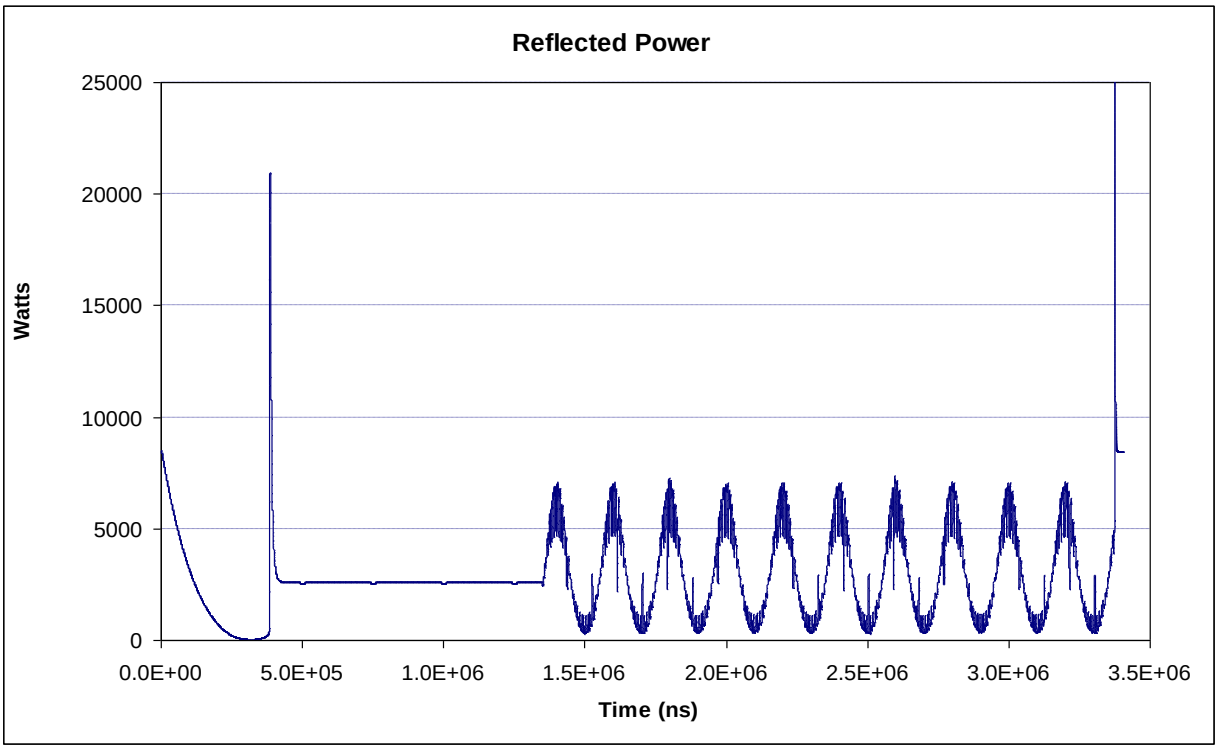

Figure 25.8 Power reflected from cavity for whole period - simulation 1

Depending on the control parameters the cavity voltage can overshoot the voltage set point; this occurs at 3.9 ms. In response the control system reverses the drive phase, the voltage at the coupler doubles and for a very short period, the power leaving the cavity can be 4 times the maximum input. In this case the reflected power only rises to 22 kW. At the quench, the instantaneous reflected power is 33.1 kW and this value is determined by the instantaneous voltage in the cavity at the time of the quench.

Figure 25.9 shows the drive phase throughout. Beam loading puts a similar demand on the drive phase as does the microphonic detuning of 40 Hz. The phase shift of the drive needed to compensate beam loading depends on the extent to which microphonics has detuned the cavity.

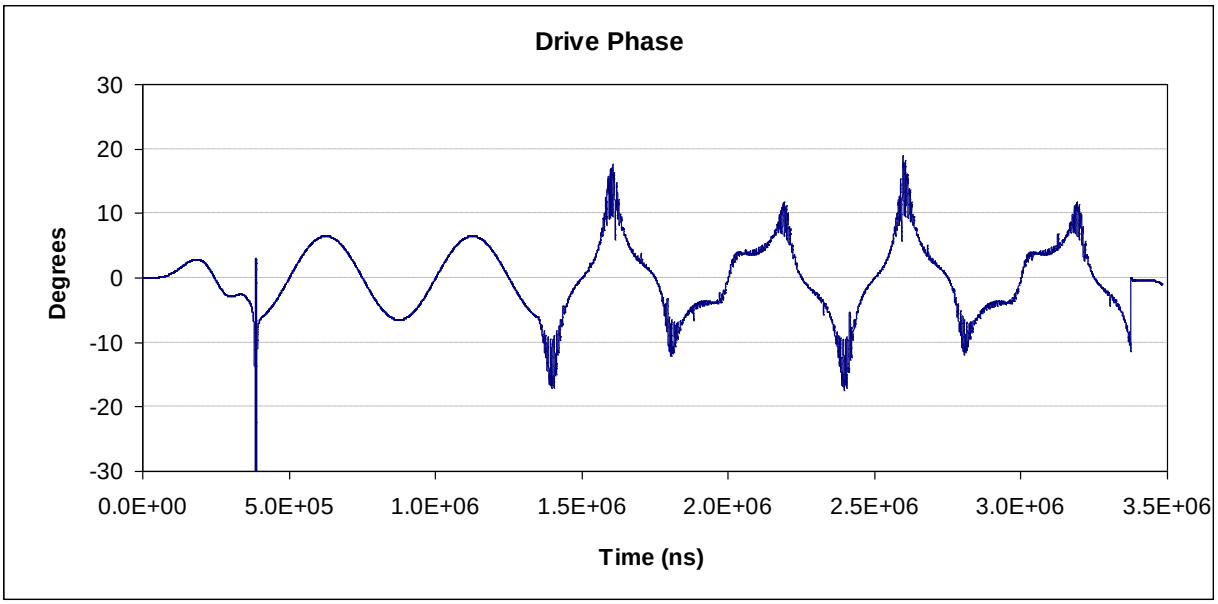

Figure 25.9 Drive phase for whole period - simulation 1

Figure 25.10 shows cavity amplitude and phase before and after the quench on a logarithmic scale. The quench is instigated by reducing the intrinsic Q factor of the operating mode to 1500. Note that with respect to the input data and equation (25.12) that the intrinsic frequency of the cavity ω_i is that for a completely lossless cavity and the actual natural frequency is determined by the intrinsic Q factor so that reducing the intrinsic Q factor to 1500 also reduces the natural frequency. Figure 25.10 shows the amplitude dropping by a factor of 300 before the phase error exceeds 1 degree. In the absence of Lorentz detuning this result implies that a quench should not pose any difficulty with spurious kicks. During the quench the cavity field decays in 7 μs In order to limit the effect of Lorentz detuning during the quench the cavity walls must be sufficiently thick, so that detuning is less than about a quarter of the bandwidth (250 Hz) in 7 μs. An effect still to be considered is where part of the cavity quenches but enough is still superconducting for high Q to be maintained however the partial quench causes a helium pressure increase that changes the cavity frequency.

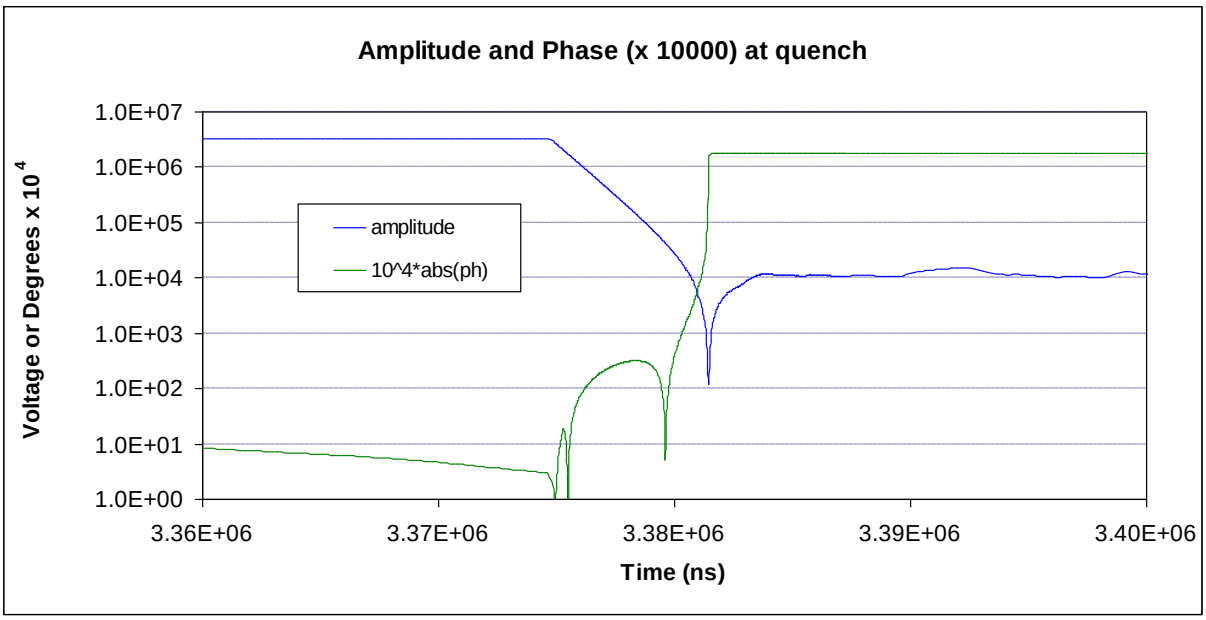

Figure 25.10 Cavity amplitude and phase before and after the Quench - simulation 1

Note that within the context of the model the control system detects the quench and resets the voltage set point to a value achievable with the power available for the new Q factor. During the correction the cavity phase shifts by 180^{o} but then recovers.

Figure 25.11 plots spectral noise for the simulation identical to that above except that it continued for 600 machine revolutions. Sine and cosine FFTs of the cavity voltage were determined, the square pulse subtracted and then values for the graph converted to dB as $10\log_{10}\left(\tilde{V}/V_s\right)^2$ where $\tilde{V}$ is the FFT of the voltage and V_s is the set point voltage.

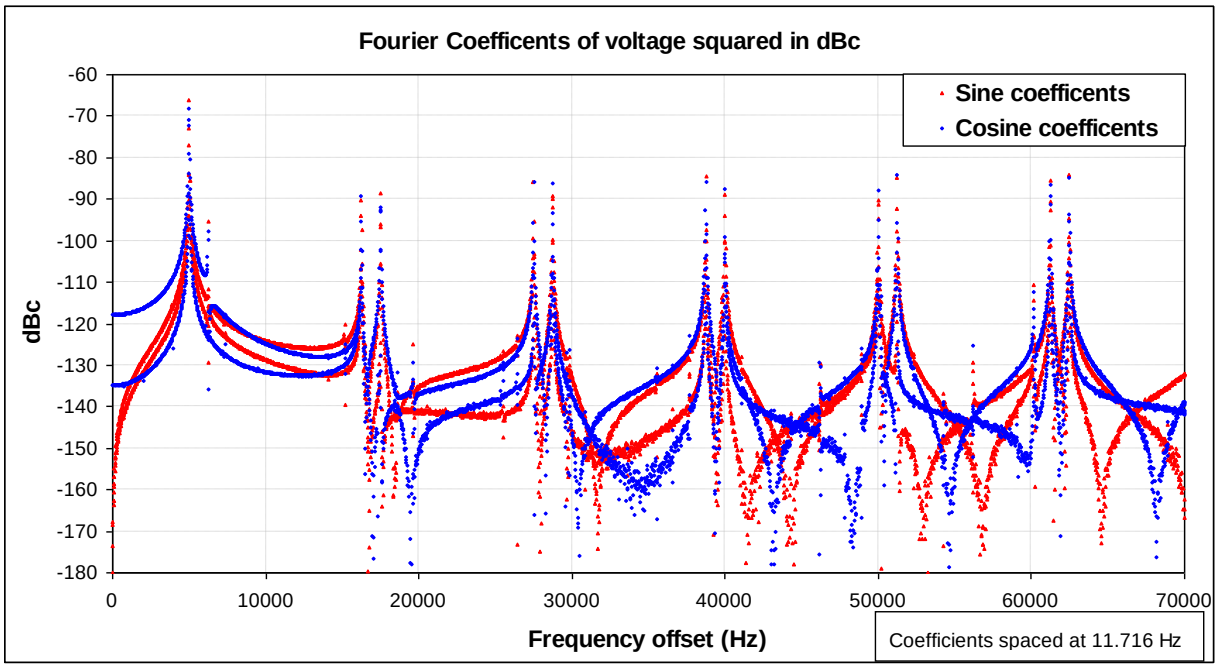

Figure 25.11 **Cavity spectral noise – simulation 1, no measurement errors.**

Two curves appear for the Sine coefficients and the Cosine coefficients, in each case one curve is associated with positive coefficients and the other with negative coefficients. As the coefficients were squared then all coefficients are represented on the graph.

The beam loading frequency is 5 kHz and the LHC revolution frequency is 11.245 kHz. Effects are seen at 5 kHz, 6.245kHz, 16.245 kHz, 17.450 kHz ….as expected. The microphonics which were added at 2 kHz[4] have minimal effect on the spectral noise and cannot be identified in Figure 25.11. The width of the peaks is determined by the sample length, in this case 600 revolutions ~ 50 ms.

Figure 25.12 gives absolute values for coefficients of the Sine and Cosine Fourier Transforms of the Inphase and Quadrature voltage functions expressed in dB. These coefficients are required to assess the impact of noise on the beam. Sine and cosine FFTs of the I and Q voltages were determined, the square pulse subtracted and then values for the graph converted to dB as $20\log_{10}\left\{\text{abs}\left(\tilde{V}_x/V_s\right)\right\}$ where $\tilde{V}_x$ is the FFT of either the I or Q voltage.

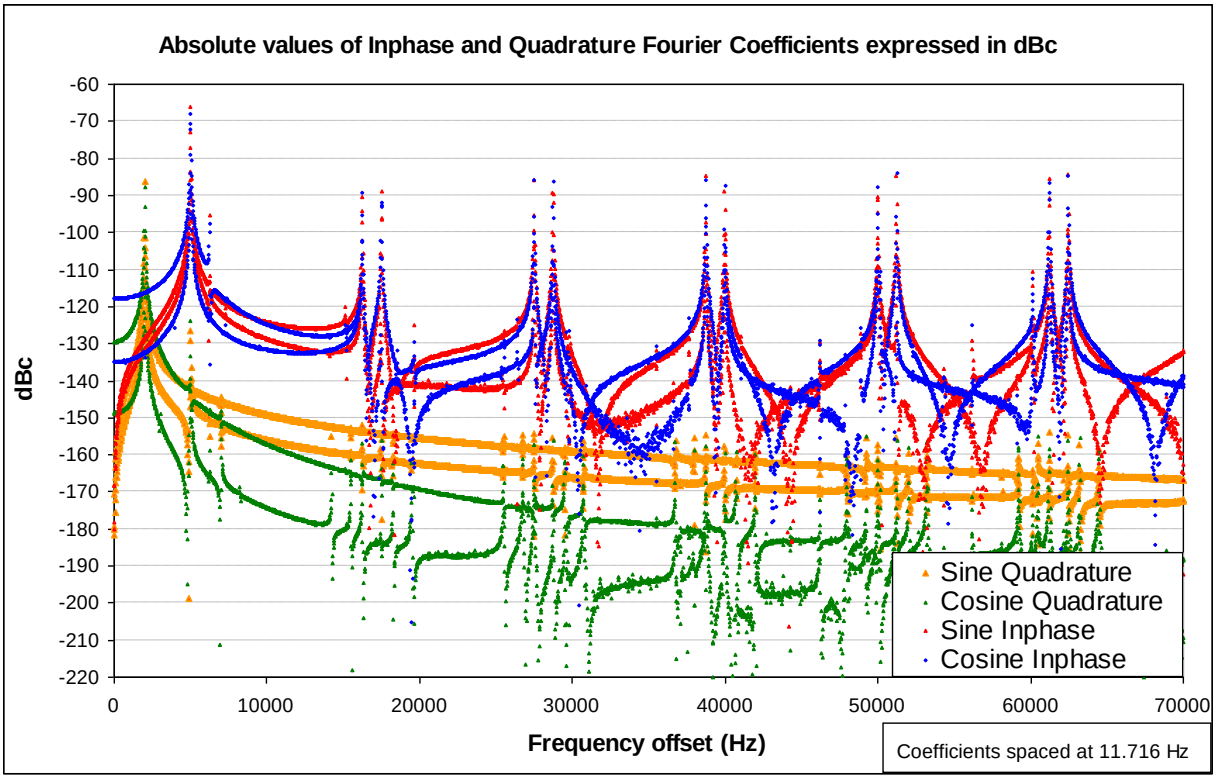

Figure 25.12 Cavity In phase and quadrature spectral voltage noise – simulation 1

The Quadrature noise in Figure 25.12 comes predominately from the 2kHz microphonic sampled for ~50 ms.

Figure 25.13 plots Fourier coefficients for the phase expressed in dB. Sine and cosine FFTs of the phase in radians were determined and then values for the graph converted to dB as $20\log_{10}\left\{\text{abs}\left(2\tilde{\theta}/\pi\right)\right\}$ where $\tilde{\theta}$ is the FFT the phase.

[4] A frequency of 2 kHz was chosen as higher frequencies are more demanding of the control system than lower frequencies and significant microphonic can be present in the kHz range.

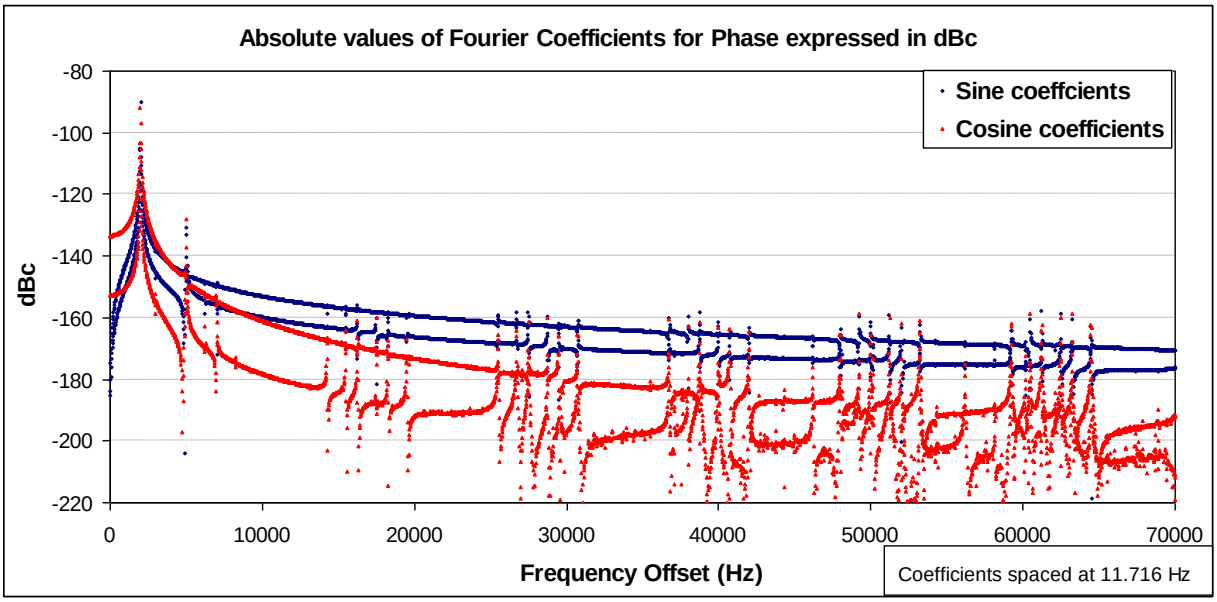

Figure 25.13 Phase noise – simulation 1

25.5.2 Simulation 2 results assuming realistic measurement errors.

The addition of realistic measurement errors has a significant effect on the control system and the spectral noise. For simulation 2 we assume that voltages are measured to an accuracy of 0.05% and that phase is measured to an accuracy of 0.005 degrees.

The LLRF parameter list for simulation 2 was taken as follows:-

```
Master oscillator frequency (GHz)       : 0.4008d0
Bunch frequency (GHz)                   : 0.04008d00
Energy set point (Joules per cell)      : 1.89
Maximum Amp Power (Watts per cell)      : 8500.0
Maximum beam offset (mm)                : -0.250
1 for random offset 0 for periodic      : 0
Offset fluctuation frequency (Hz)       : 5000.0d00
Initial Bunch phase retard (degrees)    :  0.0
Bunch phase jitter (degrees)            :  0.0
1 for random charge fluc 0 for periodic: 0
Phase jitter frequency (Hz)             : 5000
Bunch charge fluctuation (fraction)     : 0.005
1 for random charge fluc 0 for periodic: 1
Charge fluctuation frequency (Hz)       : 5000
Bunch charge (Coulombs)                 : 3.2e-8
Bunch train length (seconds)            : 86.90166e-6
Bunch train gap length (seconds)        :  2.02096e-6
RF advance time (seconds)               : 200.0e-6
Cavity freq. shift from microphonics Hz: 40.0
Vibration frequency of cavity  (Hz)     : 2000.0
Initial vibration phase (degrees, sin) : 0
Measurement phase error in degrees      : 0.005
Measurement amplitude error as fraction: 0.0005
Delay for control system in seconds     : 0.5e-6
Control update interval in seconds      : 0.5e-6
Initial gain constant for controller    :  10.0
Amplifier Bandwidth                     :  5.0e6
Measurement filter bandwidth            : 10.0e6
Feed forward sum jump  (~1.2e6)         : 0.0e6
```

Figure 25.14 shows the cavity voltage during the pulse. Measurement errors on the voltage have been introduced at the level of 0.05% ~ 1640 volts.

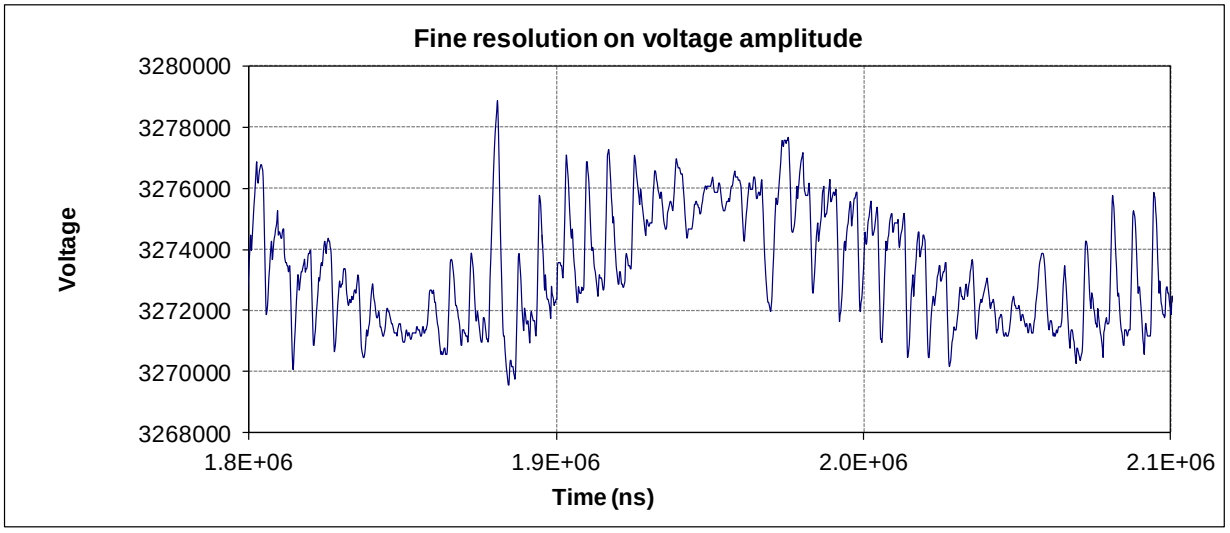

Figure 25.14 Simulation 2 with measurement errors

The error in the cavity voltage does not change significantly for errors of this magnitude. Figure 25.15 gives the phase during the pulse. Phase measurement errors were introduced at the level of 0.005 degrees however the impact on cavity phase errors is a little less than the error introduced in the measurement.

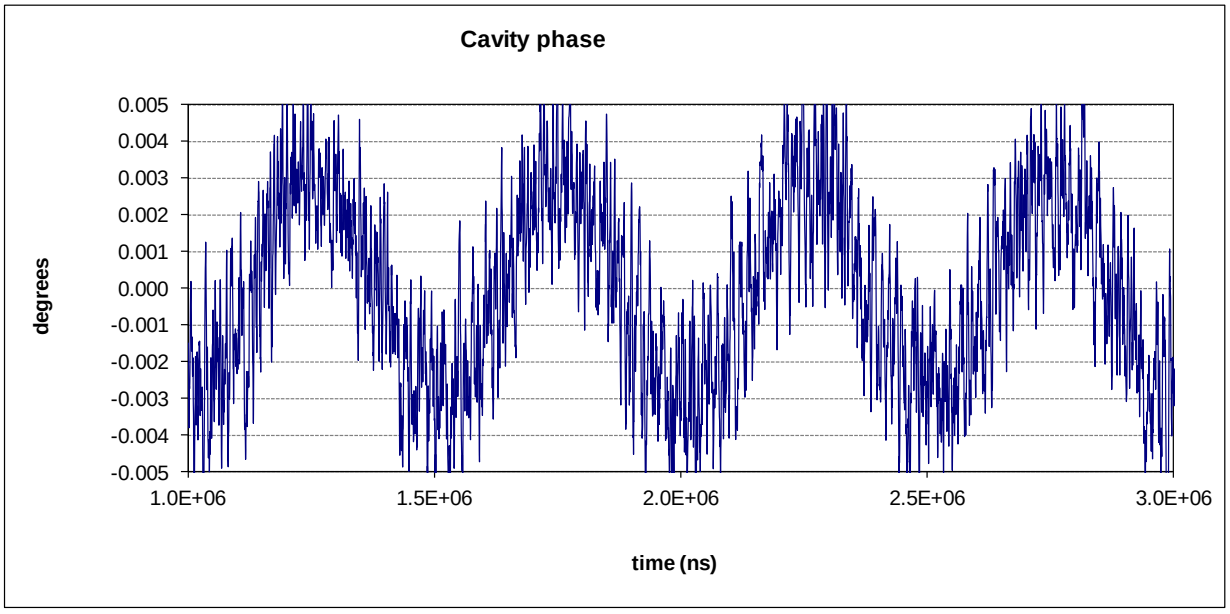

Figure 25.15 Simulation 2 with measurement errors

Figure 25.16 gives the power requirement for the simulation period whilst the beam was present.

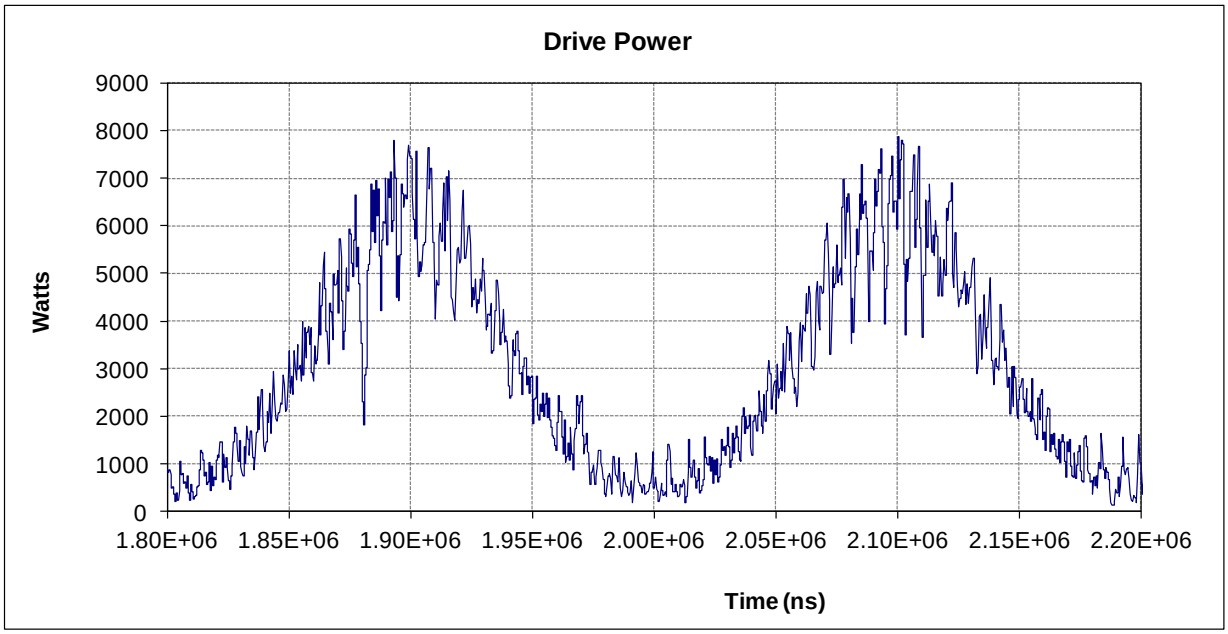

Figure 25.16 Simulation 2 with measurement errors

Figure 25.17 gives the noise spectra while the beam is present. The introduction of measurement errors at the anticipated level has given a uniform noise floor at 107 dB below the set point energy and hence the Fourier voltage coefficients are $10^{-(107/20)} = 4.5$ millionths of the set point voltage.

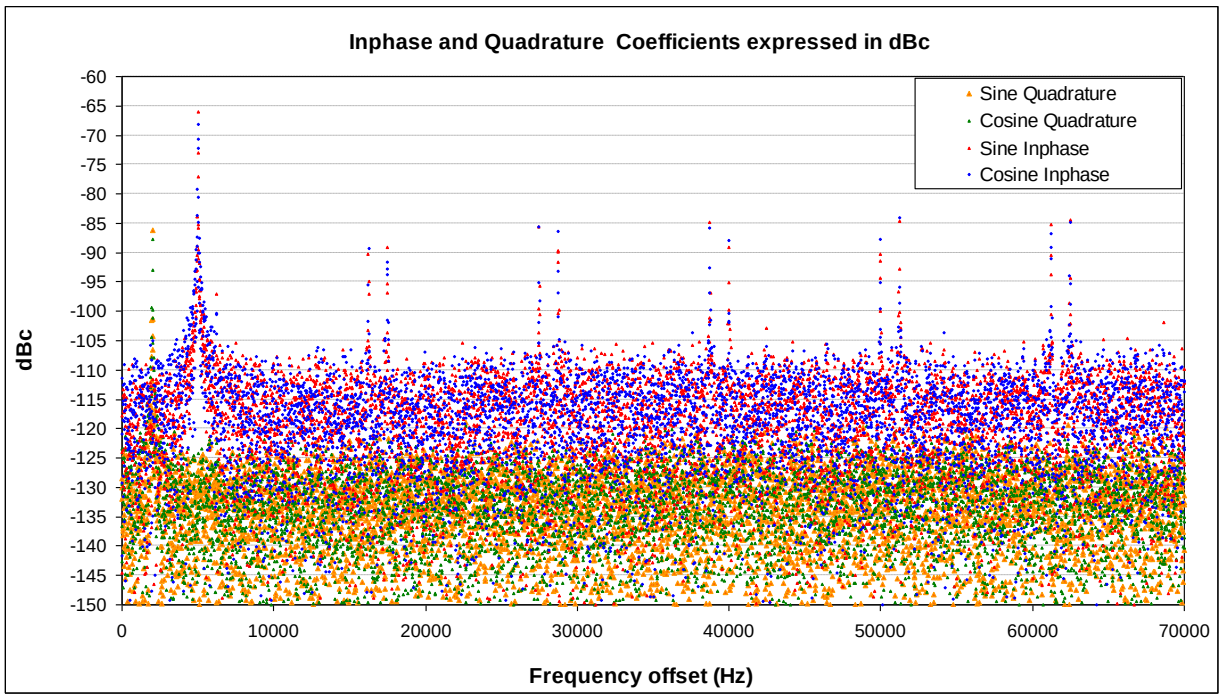

Figure 25.17 Simulation 2 with measurement errors Phase=0.005 deg, Amp =0.0005

Figure 25.18 gives absolute values of the Fourier coefficients of the phase and should be compared with Figure25.12.

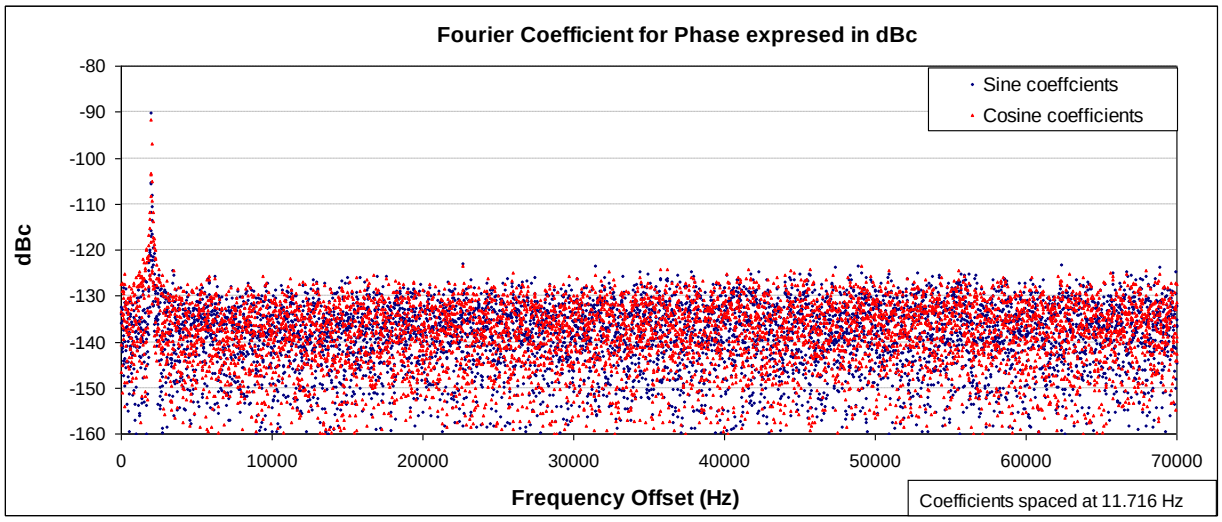

Figure 25.18 Simulation 2 with measurement errors Phase=0.005 deg, Amp =0.0005

25.5.3 Simulation 2a reduced measurement errors.

The errors assumed for simulation 2 were realistic however it is of interest to consider how the noise is reduced as the measurement errors are reduced. Figure 25.19 consider the case where phase measurement accuracy stays the same but amplitude errors are reduced by a factor of 5 with respect to simulation 2. This figure should be compared with Figure 25.17. The noise level between the peaks is reduced by just over 10 dB.

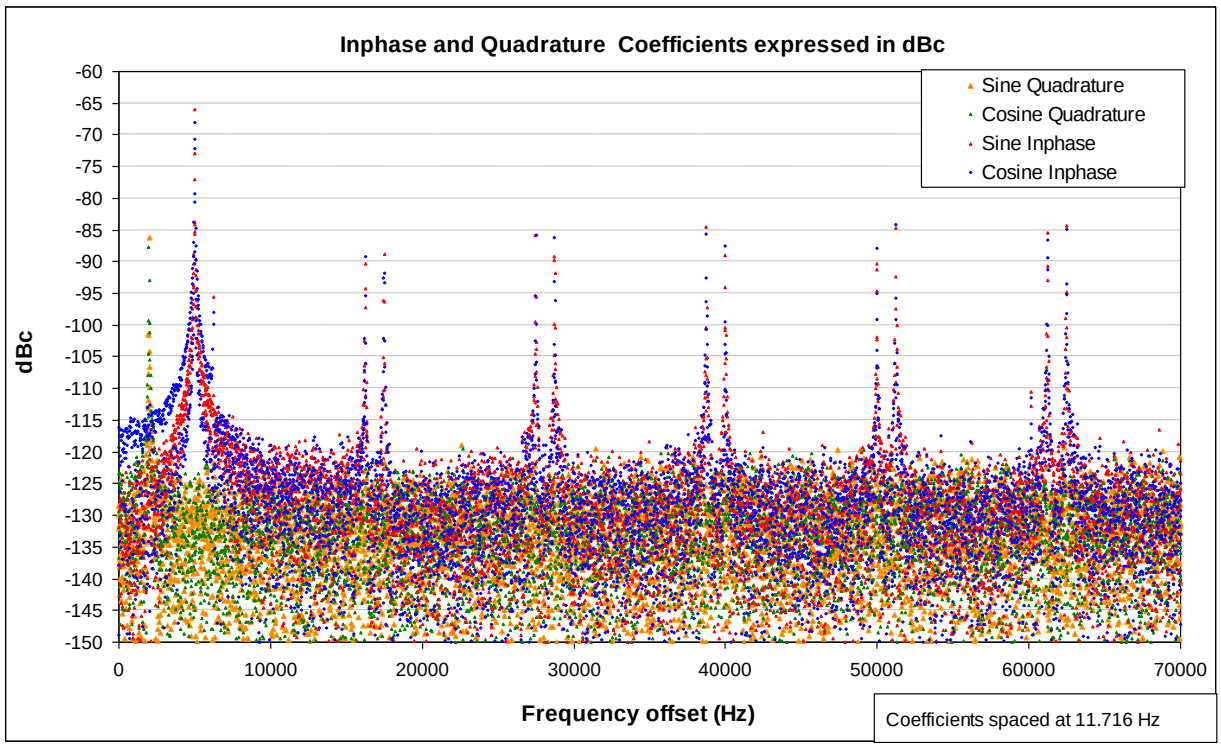

Figure 25.19 Simulation 2a with measurement errors Phase=0.005 deg, Amp =0.0001

Figure 25.20 plots the noise when the amplitude errors are reduced by a further factor of 5.

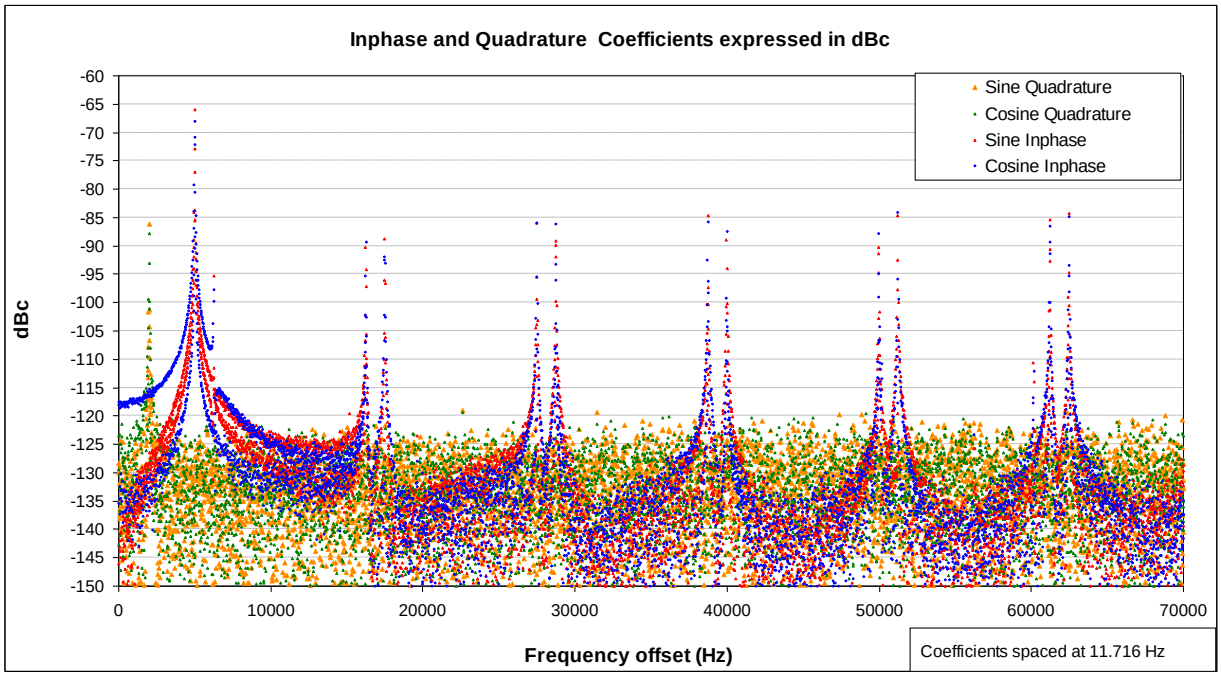

Figure 25.20 Simulation 2b with measurement errors Phase=0.005 deg, Amp =0.00002

The noise between the peaks for the inphase voltage is reduced again by just over 10 dB and comes to the level determined by the sample width limitation. The phase noise associated with the quadrature components now exceed the inphase noise components. Figure 25.21 retains the amplitude error as 1 part in 50000 and reduces the phase noise to 0.001 degrees.

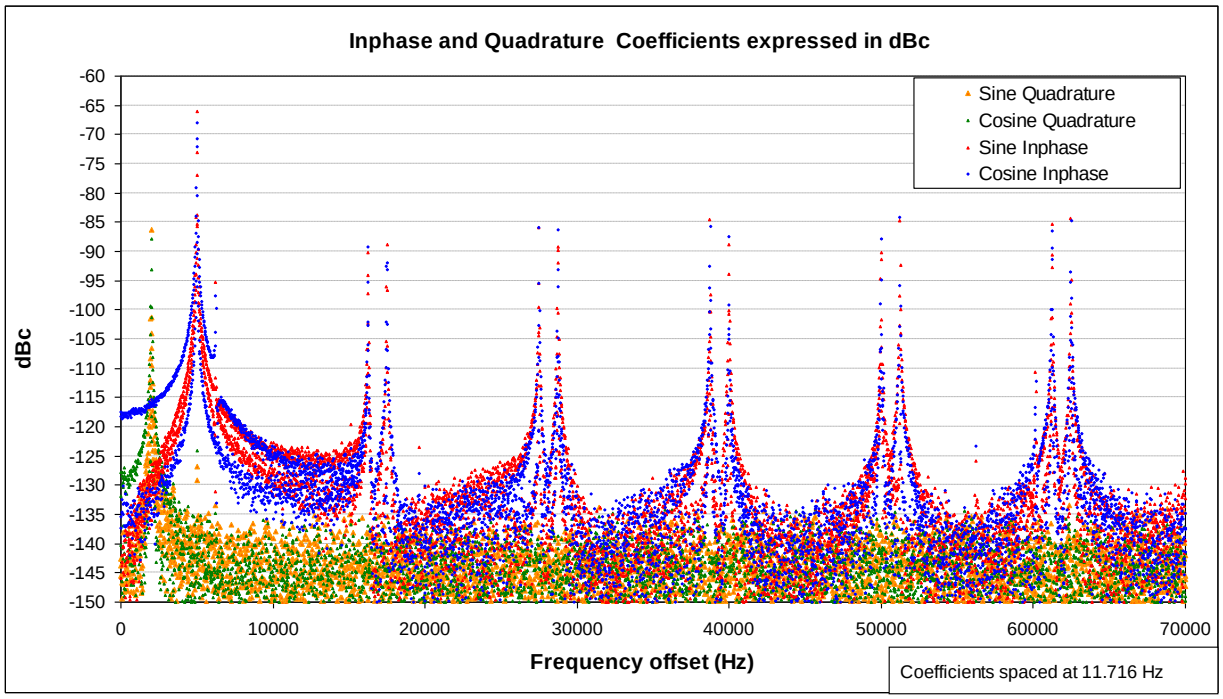

Figure 25.21 Simulation 2c with measurement errors Phase=0.001 deg, Amp =0.00002

25.5.4 Simulation 3 results using a reduced LLRF gain

Simulation 3 repeats simulation 2 with a gain reduced from 10 to 1. This has the effect of increasing amplitude and phase errors substantially, smoothing the power demand and raising noise close to the carrier frequencies as illustrated in Figures 25.22 to 25.24.

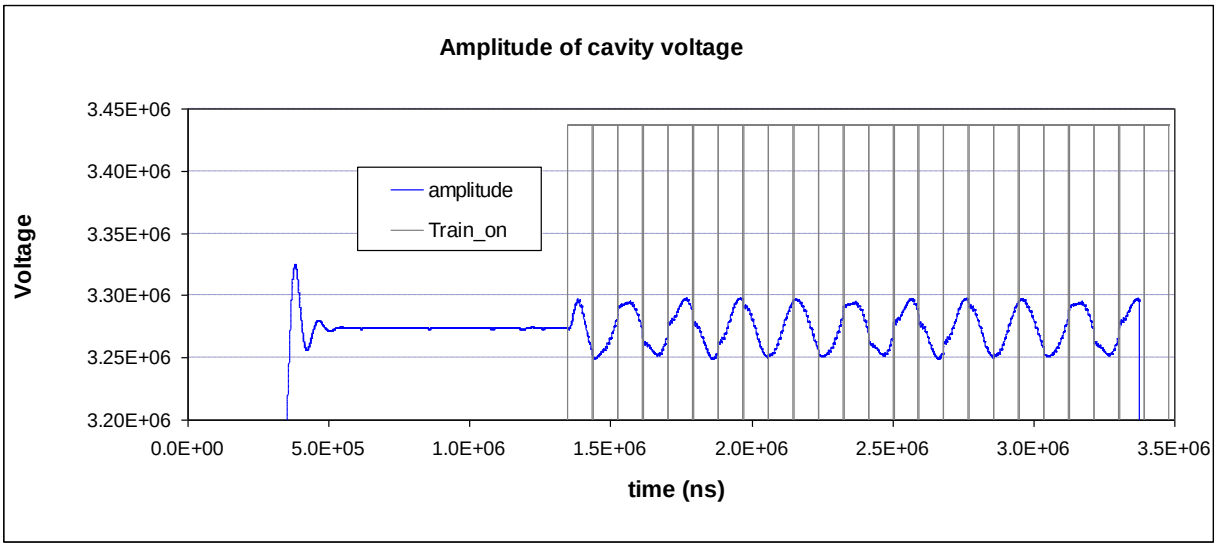

Figure 25.22 Simulation 3 with measurement errors and reduced gain

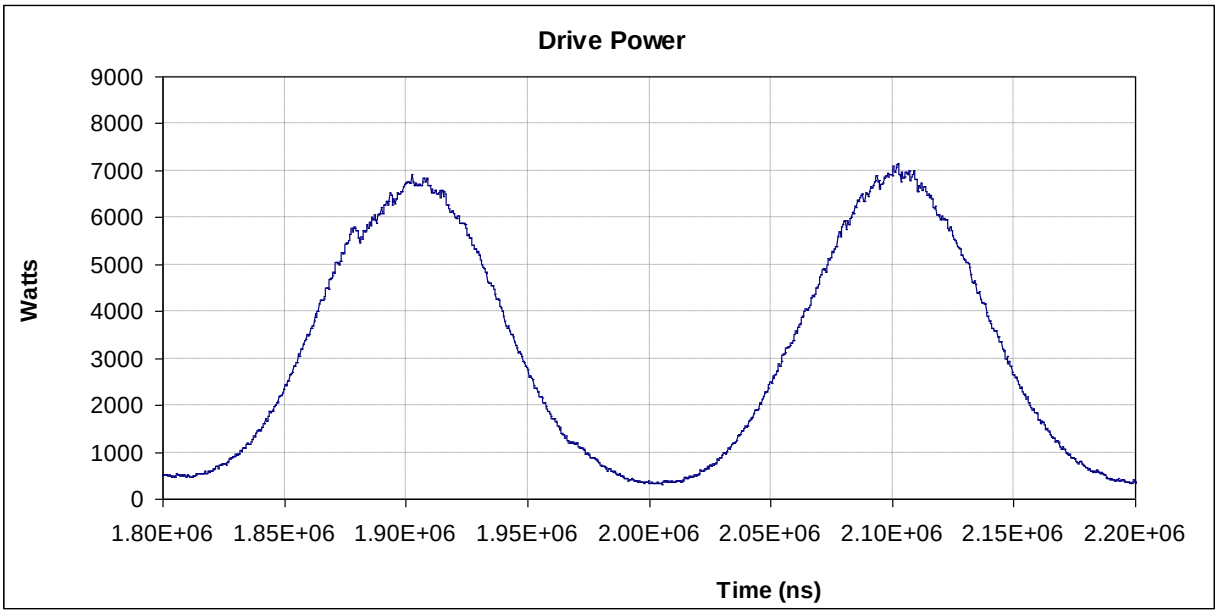

Figure 25.23 Simulation 3 with measurement errors and reduced gain

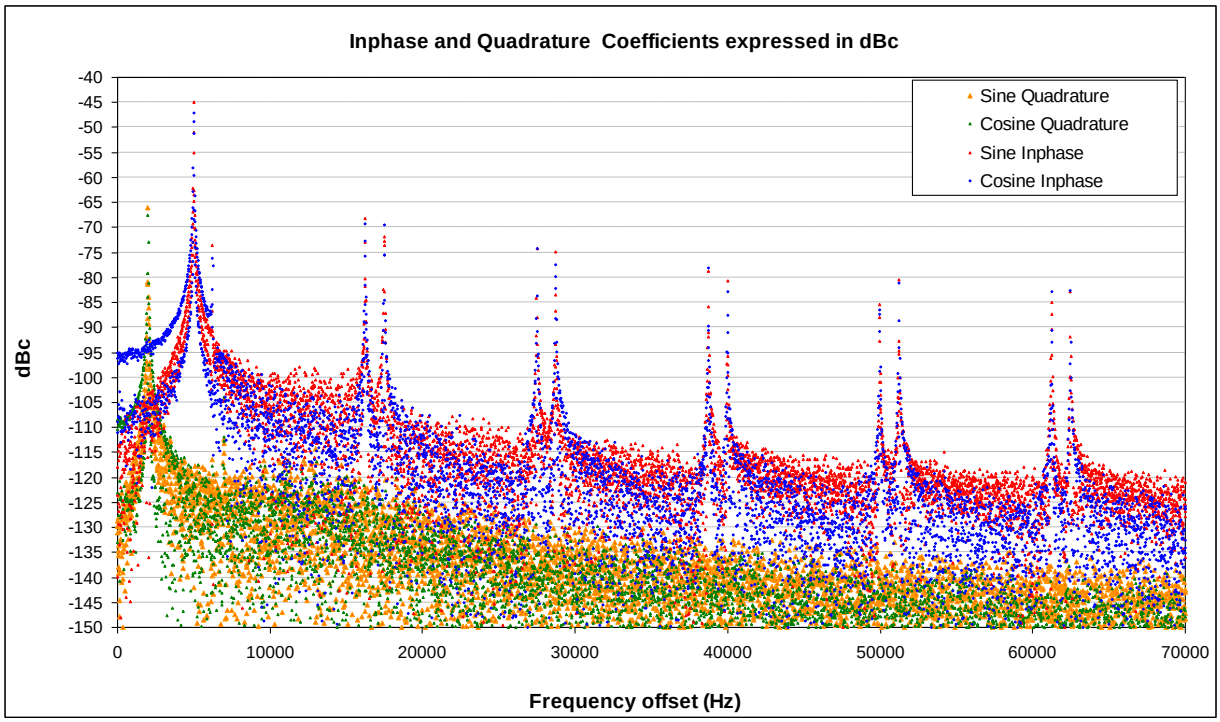

Figure 25.24 Simulation 3 with measurement errors and reduced gain Phase=0.005 deg, Amp =0.0005, Gain = 1

Figure 25.24 should be compared with figure 25.16 which had a flat noise floor below the peaks at -109 dB. Figure 25.24 shows that by reducing the gain the noise floor goes down at large offsets from the carrier but is increase close to the carrier.

The ultimate performance requires high gain and excellent measurement accuracy. Importantly if there are disturbances close to the carrier frequency then very high gain is required to remove them.

25.6 Detected LLRF Failure

In the event that the crab cavity or any of its systems fail, an essential requirement is that any failure mode does not result in the bunch train hitting the wall before the beam can be dumped [31]. It takes three revolutions to dump the beam after a failure has been identified. A worst case scenario for the crab cavity is that the LLRF system in response to an input error shifts the phase of the cavity by 90 degrees so that it becomes a deflection cavity. The response of the cavity to an incorrect set point depends on the maximum RF power and the external Q factor. Figure 25.25 plots the phase response of the cavity after the set point changes by 90^{o} at 2.842 ms into the simulation.

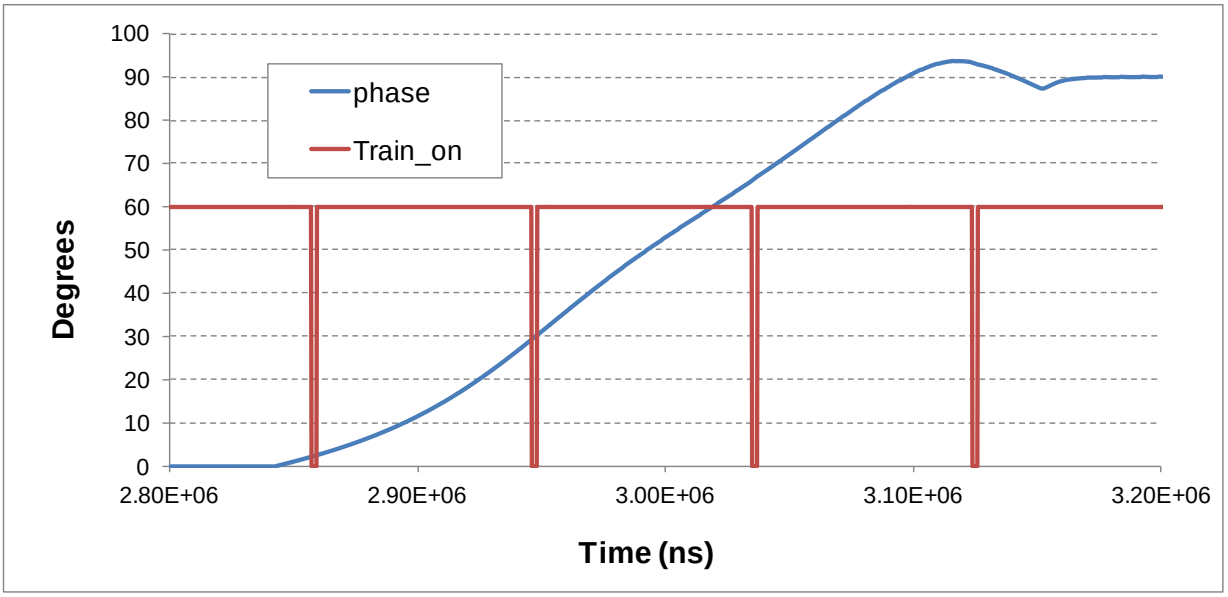

Figure 25.25 Simulation 2d, phase error with time after set point shifts by 90^o

The input data for this simulation is identical to simulation 2. After one machine revolution the phase error in the cavity is 30 degrees and the resulting bunch deflection is unacceptable. It takes three machine revolutions to dump the beam and in this time the control system can reset the reference phase by 90^o.

Once the bunch starts to show a deviation from the design orbit one anticipates that the transverse damping system will start to correct the deviation. Depending on the gain of the transverse damping system, one would expect some mitigation of the deflection over two machine revolutions.

It is probable that a safety critical system would be installed to mitigate the effect of a crab cavity RF control error. It would be straightforward to have a system that measures the difference between cavity phase and beam phase independently of the LLRF control. In the event that this phase difference rises above a set level near to 1 degree then control action could be taken. Cutting power to the cavity would initially prevent the phase from increasing however as the cavity emptying time is several milli-seconds, changes in cavity dimensions resulting from microphonics could shift the phase further. The control solution is either to have an emergency kicker with a rise time of about 25 μs or to correctively steer the bunch through the crab cavities.

25.7 Cavity Power Failure

In the event that the power amplifier was to fail then offset bunches would either fill the crab cavity with the correct phase, empty it at the correct phase or fill it with a phase error of 180°. The voltage achieved in the cavities depends on bunch offset and cavity external Q factor. For an amplifier sized for a maximum offset of 250 μm when the bunch is offset by a value less than this value the maximum voltage that can be delivered will be reduced by the ratio of the actual offset to the maximum design offset. When the cavity is filled with a 180° phase error then bunches rotate in the wrong sense for increasing luminosity. As the fill time is of the order of milli-seconds then even a bunch train with an offset slightly larger than the maximum design offset could be dumped before cavity voltages become excessive. As it is certain that kickers need to be in place to steer the beam through the crab cavities then the possibility of excess field in the cavity is not going to arise.

The scenario of no RF power is illustrated by simulation 4. The In phase and quadrature voltages are plotted in Figure 25.26.

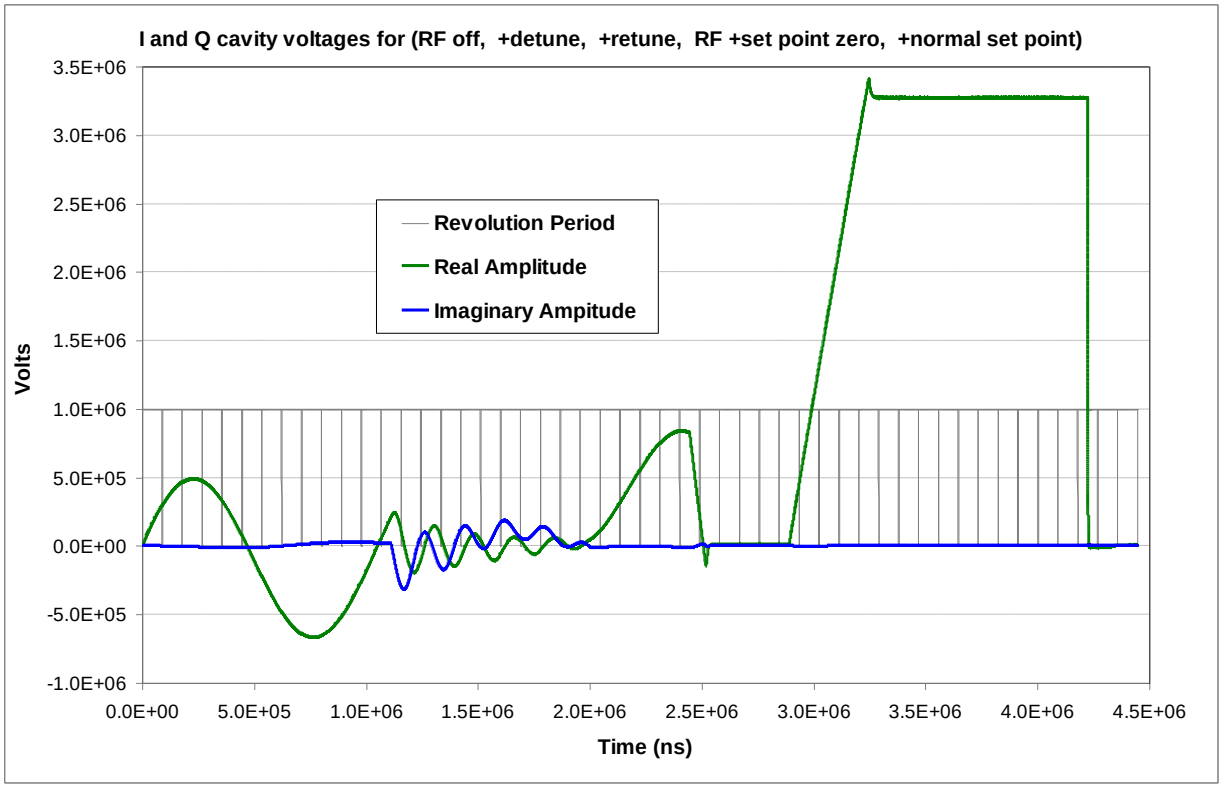

Figure 25.26 Simulation 4 with measurement errors

For this simulation the bunch offset amplitude is still 0.25 mm however the frequency has been reduced to 900 Hz. The microphonic detuning is still 40 Hz however the frequency has been reduced to 450 Hz. In the first period to 1.12 ms the beam is present but the RF is off. During this period the cavity "in phase" voltage follows the beam offset. Its peak value would grow as the frequency of the offset is reduced. Its peak value at zero offset frequency is set by the offset amplitude and the external Q factor. The quadrature voltage would be zero for the first period to 1.12 ms were the cavity not being detuned by the microphonics. As microphonics is small the quadrature voltage remains small.

During the second period from 1.12 ms to 2.03 ms the cavity has been detuned by eight bandwidths. The maximum amplitude is now restricted however the "quadrature voltage" has the same magnitude as the "in phase" voltage and hence the phase of the cavity is cycling through 2π radians.

For the third period from 2.03 ms to 2.52 ms the cavity is retuned. At 2.52 ms the RF system is energised with a set point voltage very close to zero and a phase of zero. (Phase has no value at zero voltage). This null set point continues to 2.9 ms. The figure demonstrates that keeping the RF energised with a zero set point might be a more effective way of turning the cavity off than explicitly de-tuning it.

26. RF System Spectral Noise and Bunch Lifetime

Section 25 considered fields in the cavity and the noise spectrum arising from controller action. This section considers how those fields act on individual particles in a bunch. A calculation of bunch lifetime falls outside the scope of this study. This section simply shows how the Fourier Coefficients of the cavity voltage (including noise) are used to compute the time averaged voltage that an individual particle would experience.

A particle in a bunch at the LHC will see each crab cavity field once on every revolution. A particle in the centre of the bunch which passes centrally through the cavity on its axis at the perfect time sees no net voltage. A particle passing either side of the axis with offset x in the crabbing plane will be accelerated or retarded depending on the side that it passes. A particle will receive a transverse kick voltage one way or the other way in the crabbing plane depending on whether it arrives early or late.

The analysis here will consider lateral positional deviations of a particle from the design path x(t) and longitudinal phase deviations from the design path $\phi(t)$. Specifically one wants to know the added contribution from one or more crab cavities. Previously (25.13) has given I and Q components of the crab cavity voltage as A_r and A_i. The crab cavity voltages only act on a particle once per revolution of the whole machine. Let T_o be the revolution period of bunches in the LHC. Individual particles will have a small oscillatory variation in the revolution period at the Synchrotron frequency and this variation is encompassed by longitudinal deviations from the design path $\phi(t)$.

The sum voltage that acts on a particle whose starting displacement was $x(t_o)$ and whose starting phase was $\phi(t_o)$ is given as

$$V_x\{x(t_o),\phi(t_o)\} = \mathrm{Re}\left[-j\sum_m \{A_r(t)+jA_i(t)\}\exp\{\,j\omega_{RF}\,\phi(t)/c\,\}\,\delta(t-mT_o)\right] \quad (26.1)$$

$$V_z\{x(t_o),\phi(t_o)\} = \mathrm{Re}\left[\sum_m \{A_r(t)+jA_i(t)\}\frac{x(t)\omega}{c}\exp\{j\omega_{RF}\,\phi(t)/c\}\,\delta(t-mT_o)\right] \quad (26.2)$$

In future we will not explicitly write out the dependence of V_x and V_z on the starting location of the particle of interest. As the "in phase component" is taken with respect to the crabbing phase then (26.1) is multiplied by –j. The time dependence of A_r and A_i is taken with respect to the master oscillator and the master oscillator is locked to the revolution period. A_r and A_i are evaluated for the average lateral deflection x of the particle and at time t when the

bunch is at the cavity centre. The summation in m is over 11245 cavity interactions per second for many hours. Eliminating the complex notation in (26.1) and (26.2) gives

$$V_x = \sum_m \left[A_r \sin(\omega_{RF}\,\phi/c) + A_i \cos(\omega_{RF}\,\phi/c)\right] \delta(t - mT_o) \tag{26.3}$$

$$V_z = \sum_m \frac{x\,\omega}{c} \left[A_r \cos(\omega_{RF}\,\phi/c) - A_i \sin(\omega_{RF}\,\phi/c)\right] \delta(t - mT_o) \tag{26.4}$$

The motion of particles following the design path (x = 0, ϕ = 0) when the crab cavity voltage is a perfect sine wave at the operating frequency and correctly phased is completely understood. Here the interest is for particles not on the design path and interacting with unwanted voltage signals and spectral noise in the cavity.

In general the x displacement of a particle from the design orbit in a Synchrotron is given as:

$$x(s) = a\sqrt{\beta(s)}\cos\left(\int_0^s \frac{ds'}{\beta(s)} - \theta\right) \tag{26.5}$$

where a and θ are constants for a particular particle, s is distance along the design path and β is the betatron function. If one only looks at the x displacement at a single point around a storage ring then as the integrand determining the phase in (26.5) has the periodicity of the ring then x displacements at a point change incrementally following a sinusoidal wave is given as:

$$x_m = a\sqrt{\beta(s_c)}\cos(2\pi m\nu - \theta) \tag{26.6}$$

where ν is the betatron number, s_c is the position of the crab cavity and m is an integer [32]. The value of ν will be an integer plus a fractional part ν_f. As ν is multiplied by 2π times an integer in (26.6) then only the fractional part of ν contributes. Defining the betatron frequency as

$$f_b = \frac{\nu_c}{T_o} \tag{26.7}$$

then the x displacement while the particle is in the crab cavity can be expressed as

$$x(t) = \Delta x\ \delta(t - mT_o)\cos(2\pi f_b t - \theta_b) \tag{26.8}$$

where Δx is the maximum displacement at the crab cavity and θ_b is the betatron phase. The betatron frequency at the LHC ~ 3.4 kHz; define the associated angular frequency as ω_b.

For longitudinal motion the phase ϕ(t) is related to the energy deviation ε by:

$$\frac{d\phi}{dt} = -\alpha\frac{\varepsilon}{E_o} \tag{26.9}$$

where α is the dilation factor. Equation (26.9) dictates that the phase decreases when the energy is too large and increases when it is too small, hence acting to keep particles in the RF bucket. The energy of a particle will decrease due to synchrotron radiation by U_{rad} per turn, it will therefore increase as it passes through the cavity by an amount that depends on its phase $V_a(\phi)$ and will remain in the crab cavity depending on its offset by amount $V_c(x)$ hence we can write:

$$\frac{d\varepsilon}{dt} = \frac{V_a(\phi) + V_c(x) - U_{rad}(\varepsilon)}{T_o} \tag{26.10}$$

Clearly the crab cavity can couple the longitudinal motion with the betatron motion when the bunch has an offset. For the LHC, the phase ϕ changes by only a small amount on each revolution hence we assume it has the same value in the accelerating cavity as in the crab cavity. The crab cavity is phased so that its longitudinal field is at its peak as bunches pass through hence for short bunches we can neglect the dependence of $V_c(x)$ on ϕ. As the bunches must stay in their buckets we are only interested in solutions of (26.9) and (26.10) which are oscillatory.

For small oscillations and neglecting the longitudinal acceleration in the crab cavity we can write:

$$\phi(t) = \Delta\phi\ \delta(t - mT_o)\cos(2\pi f_s t - \theta_s) \tag{26.11}$$

where f_s is the Synchrotron frequency of ~ 23 Hz for the LHC, $\Delta\phi$ is half the bunch length and we define the associated angular frequency as ω_s.

At the crab cavity operating frequency both the transverse and longitudinal components of the voltage kick imposed by the crabbing cavities should exactly cancel with the anti-crabbing cavities. The crabbing cavities act when the bunch is in line with the orbit path and the anti-crabbing cavities act when the bunch has returned to alignment with the orbit path. This means that the x displacement of each particle is identical to its value in the crabbing cavities and hence longitudinal and transverse components both cancel if the phase ϕ has not changed. As particles near the back of the bunch will have an advancing phase and particles near the front of the bunch will have a retarding phase then perfect cancellation will not be possible. Particles move from the back of the bunch to the front of the bunch in a time of 50 ms, the time between crabbing and uncrabbing is of the order of 1 μs hence the perturbation is one part in 50000 per cavity per revolution. Given that there are 11245 revolutions per second one expects the effect to be significant. If the kick and the anti-kick do not quite cancel then the overall effect is a random kick at the RF frequency. Anticipating a result given later in this section it is found that random transverse kicks average to zero unless they occur at an offset frequency equal to the synchrotron frequency.

The estimation of bunch lifetime in a proton synchrotron has a dependency on phase noise in the RF cavities [33]. Appendix II of reference [33] relates noise spectral density to the diffusion coefficient for longitudinal bunch growth and emittance growth. Here we only consider the average voltage that a particle sees after many revolutions and our analysis has a different approach. Phase locking the accelerator cavity RF to the bunch centroid together with the associated comb filters is essential to effectively damp Synchrotron oscillations. At the LHC, betratron oscillations are damped with feedback loops acting on fast kickers. Once these control loops are in place[5] then one might expect lifetime to no longer strongly depend on longitudinal and transverse bunch deflection from the perfect orbit but rather on disturbances that have a spatial gradient through the bunch. This is not true because each particle in a bunch has a different position and momentum and as a consequence of non-linear forces, intra-beam scattering [34] and beam-beam interactions [35] a uniform kick applied to all the particles does not result only in a kick of the whole bunch. The uniform kick de-coheres through these non-

[5] These control loops are always active for the LHC.

linear forces and interactions resulting in emittance growth. In the absence of experimental data, best estimates of emittance growth comes from simulation [36, 37]. As yet no simulations that include the non-linearity of the crab cavity field have been undertaken.

26.1 Kick Estimation for Single Frequency Disturbance

The continuing analysis below relates voltage kicks at dangerous frequencies for spectral noise to the LLRF simulations. For clarity we will initially consider a single component of the noise spectrum in the cavity taken at an offset angular frequency ω_n from the RF frequency. For noise at an offset frequency there is no guarantee that the mode is perfectly dipolar hence the x dependence in (26.3) and (26.4) will need to be reconsidered in a more detailed analysis. Explicitly in (26.3) and (26.4) the field will be taken as:

$$A_r(t) = \tilde{A}_{nr}\cos(\omega_n t) \tag{26.12}$$

$$A_i(t) = \tilde{A}_{ni}\cos(\omega_n t) \tag{26.13}$$

we should add a separate phase in each term or split it as sine and cosine terms however the initial result required does not depend on the phase so it is put back later rather than writing a sine and cosine version of every equation.

When inserting the orbit (26.11) into (26.3) and (26.4) we assume that longitudinal phase deviations are sufficiently small for the bunch to roughly fit in the linear part of the field so that:

$$\sin(\omega_{RF}\,\phi/c) \approx \frac{\omega_{RF}\Delta\phi}{c}\cos(\omega_s t - \theta_s) \tag{26.14}$$

and

$$\cos(\omega_{RF}\,\phi/c) \approx 1 \tag{26.15}$$

Putting (26.8) and (26.11-26.15) in (26.3) and (26.4) gives:

$$\tilde{V}_x = \sum_m \left[\tilde{A}_{nr}\frac{\omega_{RF}}{c}\Delta\phi\cos(\omega_n t)\cos(\omega_s t - \theta_s) + \tilde{A}_{ni}\cos(\omega_n t)\right]\delta(t - mT_o) \tag{26.16}$$

$$\tilde{V}_z = \sum_m \left[\tilde{A}_{nr}\frac{\omega_{RF}}{c}\Delta x\cos(\omega_n t)\cos(\omega_b t - \theta_b) - \tilde{A}_{ni}\left(\frac{\omega_{RF}}{c}\right)^2\Delta\phi\,\Delta x\cos(\omega_n t)\cos(\omega_b t - \theta_b)\right]\delta(t - mT_o) \tag{26.17}$$

Note that the voltages have been given tilda's as they are associated with single frequency components of the cavity fields.

Defining the revolution frequency as f_o which for the LHC ~ 11245 Hz and setting $\omega_n = 2\pi f_n$ and applying the delta functions in (26.16) and (26.17) gives:

$$\tilde{V}_x = \sum_m \left[\tilde{A}_{nr}\frac{\omega_{RF}}{c}\Delta\phi\cos\left(\frac{f_n}{f_o}2\pi m\right)\cos\left(\frac{f_s}{f_o}2\pi m - \theta_s\right) + \tilde{A}_{ni}\cos\left(\frac{f_n}{f_o}2\pi m\right)\right] \tag{26.18}$$

$$\tilde{V}_z = \sum_m \left[\tilde{A}_{nr} \frac{\omega_{RF}}{c} \Delta x \cos\left(\frac{f_n}{f_o} 2\pi m\right) \cos\left(\frac{f_b}{f_o} 2\pi m - \theta_b\right) - \tilde{A}_{ni} \left(\frac{\omega_{RF}}{c}\right)^2 \Delta\phi \Delta x \cos\left(\frac{f_n}{f_o} 2\pi m\right) \cos\left(\frac{f_b}{f_o} 2\pi m - \theta_b\right) \right] \quad (26.19)$$

Now substitute for cosine products with separate cosine terms in (26.18) gives:

$$\tilde{V}_x = \sum_m \left[\tilde{A}_{nr} \frac{\omega_{RF}}{2c} \Delta\phi \left\{ \cos\left(\frac{f_n - f_s}{f_o} 2\pi m - \theta_s\right) + \cos\left(\frac{f_n + f_s}{f_o} 2\pi m + \theta_s\right) \right\} + \tilde{A}_{ni} \cos\left(\frac{f_n}{f_o} 2\pi m\right) \right] \quad (26.20)$$

The last term in this equation does not carry any dependence on the synchrotron or betatron phase. This means it is the same for all particles and corresponds to a kick of the whole bunch. We expect kicks of the whole bunch to be removed by the transverse damping system. These terms are therefore omitted, leaving:

$$\tilde{V}_x = \sum_m \tilde{A}_{nr} \frac{\omega_{RF}}{2c} \Delta\phi \left\{ \cos\left(\frac{f_n - f_s}{f_o} 2\pi m - \theta_s\right) + \cos\left(\frac{f_n + f_s}{f_o} 2\pi m + \theta_s\right) \right\} \quad (26.21)$$

Now substitute for cosine products with separate cosine terms in (26.19) gives

$$\tilde{V}_z = \sum_m \left[\tilde{A}_{nr} \frac{\omega_{RF}}{2c} \Delta x \left\{ \cos\left(\frac{f_n - f_b}{f_o} 2\pi m - \theta_b\right) + \cos\left(\frac{f_n + f_b}{f_o} 2\pi m + \theta_b\right) \right\} - \tilde{A}_{ni} \frac{1}{2} \left(\frac{\omega_{RF}}{c}\right)^2 \Delta\phi \Delta x \left\{ \cos\left(\frac{f_n - f_b}{f_o} 2\pi m + \theta_b\right) + \cos\left(\frac{f_n + f_b}{f_o} 2\pi m + \theta_b\right) \right\} \right] \quad (26.22)$$

If a cosine distribution is sampled at regular intervals and the samples averaged then they will average to zero unless the sampling is done at the same point in every period, i.e.

$$\lim_{N\to\infty} \frac{1}{N} \sum_{m=1}^{m=N} \cos\left(2\pi m \frac{f_x}{f_o} + \theta\right) = 0 \quad \text{for} \quad \frac{f_x}{f_o} \neq \text{int} \quad (26.23)$$

In (5.20) the cavity voltage noise only gives a sizeable transverse kick to a particle either when $f_n \pm f_s = k f_o$ where k is an integer (including zero).

In (5.21) cavity voltage noise only gives a sizeable longitudinal kick to a particle either when $f_n \pm f_b = k f_o$ where k is an integer.

It should be remembered that the frequencies f_n are offset frequencies from the RF frequency.

The value of the summation in (26.23) oscillates as N increases. It attains its first maximum value when:

$$N \sim \frac{f_o}{2(k f_o - f_x)} \quad (26.24)$$

The oscillation is offset from zero as θ increases from 0 reaching maximum negative offset at to $\theta = 0.5\pi$ and then maximum positive offset at $\theta = 1.5\pi$.

When $f_x \approx k f_o$ where k is an integer then the maximum absolute value is approximately given as

$$\text{Maximum absolute value } \sum_{m=1}^{m=N} \cos\left\{2\pi m \frac{f_x}{f_o} + \theta\right\} \approx \frac{0.17 f_o}{(k f_o - f_x)}\left(1 + |\sin\theta|\right)$$

$$\text{for} \qquad f_x \approx k f_o \qquad k = \text{integer} \qquad (26.25)$$

This expression stays valid until N is so large that the particle phase θ has shifted as a consequence of intra-beam scattering or non-linearities changing the tune of individual particles. One can assign a time constant after which the phase has on average shifted by π/2 and here this value will be taken to be τ_d .

There is no value in continuing the summation in (26.21) and (26.22) after the phase has shifted by π/2 and one should start a new summation with the voltage growing in a new direction in the complex plane. This means that the total kick grows according to a random walk where each leg of the random walk takes time τ_d . The analysis of the random walk will be done at the end of this section. Now the focus is on the length or stroke of each segment of the random walk.

The maximum appropriate value for summation N before a new summation should be commenced is determined as:

$$N \sim f_o \tau_d \qquad (26.26)$$

Given a maximum value for N from (26.26) we then get a maximum value for what was a potentially infinite pole in (26.25). Putting (26.26) in (26.24) gives:

$$\text{Max}\left[\frac{1}{(k f_o - f_x)}\right] = 2\tau_d \qquad (26.27)$$

The summation in (26.25) can of course never exceed N so that the largest time constant that should be considered is constrained by $0.34 f_o \tau_d \le N$

Equation (26.25) can now be written as:

$$\sum_{m=1}^{m=N} \cos\left\{2\pi m \frac{f_x}{f_o} + \theta\right\} \approx 0.17 f_o \left(1 + |\sin\theta|\right) \text{Min}\left[\frac{1}{(k f_o - f_x)}, 2\tau_d\right]$$

$$\text{for} \quad f_x \approx k f_o \quad k = \text{int.} \qquad (26.28)$$

This expression is awkward to use if one wants to integrate over frequencies near the pole. An easier expression to handle giving roughly the same answer would be to write:

$$\sum_{m=1}^{m=N} \cos\left\{2\pi m \frac{f_x}{f_o} + \theta\right\} \approx \frac{0.34 f_o \tau_d \left(1 + |\sin\theta|\right)}{\sqrt{4\tau_d^2 (k f_o - f_x)^2 + 1}} \qquad k = \text{int.} \qquad (26.29)$$

Note that using the replacement $\theta \to \theta + \pi/2$ in (26.29) one immediately gets the result

$$\sum_{m=1}^{m=N}\sin\left\{2\pi m\frac{f_x}{f_o}+\theta\right\}\approx\frac{0.34 f_o\tau_d\left(1+\left|\cos\theta\right|\right)}{\sqrt{4\tau_d^2\left(k f_o-f_x\right)^2+1}}\qquad k = \text{ int.}\qquad (26.30)$$

When we reach the end of the summation N as constrained by (26.24) then a new summation must commence starting with a new phase for the voltage.

In equations (26.21) and (26.22) the values of A_{nr} and A_{ni} are Fourier Transforms Coefficients for $A_r(t)$ and $A_i(t)$. With respect to the analysis to this point the equations (26.12) and (26.13) picked out one Fourier component. In general the cavity voltage would need to be decomposed with sine and cosine terms hence we sub divide A_{nr} with two sets of coefficients $A_r(f_n)$ and $B_r(f_n)$ and A_{ir} with two sets of coefficients $A_i(f_n)$ and $B_i(f_n)$ so that:

$$\tilde{A}_r\left(f_n\right)=\frac{1}{T}\int_0^T dt\, A_r(t)\cos\left(\frac{n\pi t}{T}\right)\qquad \tilde{B}_r\left(f_n\right)=\frac{1}{T}\int_0^T dt\, A_r(t)\sin\left(\frac{n\pi t}{T}\right)\qquad (26.31)$$

$$\tilde{A}_i\left(f_n\right)=\frac{1}{T}\int_0^T dt\, A_i(t)\cos\left(\frac{n\pi t}{T}\right)\qquad \tilde{B}_i\left(f_n\right)=\frac{1}{T}\int_0^T dt\, A_i(t)\sin\left(\frac{n\pi t}{T}\right)\qquad (26.32)$$

If one records the cavity voltage with its noise for a long period of time, perhaps even days then the voltage with its noise can always be exactly reconstructed as

$$A_r(t)=\frac{A_r(0)}{2}+\sum_{n=1}^{n=\infty}\left\{\tilde{A}_r\left(f_n\right)\cos\left(\frac{n\pi t}{T}\right)+\tilde{B}_r\left(f_n\right)\sin\left(\frac{n\pi t}{T}\right)\right\}\qquad (26.33)$$

$$A_i(t)=\frac{A_i(0)}{2}+\sum_{n=1}^{n=\infty}\left\{\tilde{A}_i\left(f_n\right)\cos\left(\frac{n\pi t}{T}\right)+\tilde{B}_i\left(f_n\right)\sin\left(\frac{n\pi t}{T}\right)\right\}\qquad (26.34)$$

With respect to our approach it is not appropriate to suppose that the phase of the noise can change. For a given period of sampling all the coefficients take fixed values. (*We do allow the phase of the particle to change as they are subject to intra-beam scattering and nonlinear effects.*)

The approximations (26.29) and (26.30) were about averaging the voltage that is seen by one particle as the consequence of one frequency. If now we want to consider all frequencies then the summations on n in (26.33) and (26.34) must be performed hence we have that:

$$\Delta V_x=\tilde{V}_x(0)+\sum_{n=1}^{n=\infty}\Delta\tilde{V}_x\left(f_n\right)\qquad (26.35)$$

$$\Delta V_z=\tilde{V}_z(0)+\sum_{n=1}^{n=\infty}\Delta\tilde{V}_z\left(f_n\right)\qquad (26.36)$$

(*note that the coefficient A and B are voltages)*

For long sampling periods, the summation can be replaced by an integration. The Fourier coefficients must decrease with frequency faster than reciprocal frequency for large frequencies otherwise the summations of (26.33) and (26.34) would not equate to a finite noise voltage.

The noise will apply a significant kick to a particle near a critical frequency. Assuming that the Fourier coefficients have been normalised to Volts per Hz and that they vary slowly near a critical frequency then the contribution to the kick from a critical frequency requires an integration over frequency. Comparing (26.29) with (26.21) and (26.22) then f_x takes the following values $f_n \pm f_s$ and $f_n \pm f_b$ and the integration is on f_n . Representing f_n with f and letting f_y take on one of the values $0 \quad \pm f_s \quad \pm f_b$ then the integration to be performed becomes:

$$\Delta_p \quad = \quad \int_{f=f_y-kf_o-\Delta f}^{f=f_y-kf_o+\Delta f} \frac{f_o \tau_d}{\sqrt{4\tau_d^2\left(kf_o - f_y - f\right)^2 + 1}} \quad df \qquad (26.37)$$

where Δf is some point between the integrand's peak at $f = kf_o - f_y$ and the neighbouring peak. There is a peak at every harmonic of the revolution frequency k hence it is appropriate to take $\Delta f = 0.5 f_o$. The integral simplifies and evaluates as:

$$\Delta_p \quad = \quad \frac{f_o}{2} \int_{f'=-0.5f_o}^{f'=+0.5f_o} \frac{1}{\sqrt{f^2 + \frac{1}{4\tau_d^2}}} \quad df = \frac{f_o}{2} \ln\left[\frac{\tau_d^2 f_o^2 + \sqrt{\tau_d^2 f_o^2 + 1}}{-\tau_d^2 f_o^2 + \sqrt{\tau_d^2 f_o^2 + 1}}\right] \qquad (26.38)$$

For the LHC we have $\tau_d f_o \sim N >> 1$ i.e. de-coherence takes many turns hence (26.38) approximates as:

$$\Delta_p \quad \approx \frac{f_o}{2} \ln\left[4\tau_d^2 f_o^2\right] \quad = \quad f_o \ln\left[\tau_d f_o\right] \qquad (26.39)$$

Unfortunately there is a significant contribution to the value of the integral other than from the critical frequencies which tends to cancel the value from the peak and (26.39) is incorrect by at least the factor $\ln\left[\tau_d f_o\right]$. On this basis the integration will be explored numerically in the next section.

26.2 Estimation for Flat Noise

The integral R to be investigated is as follows:-

$$R = \int_0^{\infty} \tilde{A}(f) \sum_{m=1}^{m=N} \left\{ \cos\left(\frac{f - f_p}{f_o} 2\pi m - \theta_p \right) + \cos\left(\frac{f + f_p}{f_o} 2\pi m + \theta_p \right) \right\} df \qquad (25.40)$$

where the suffix p is either s or b standing for Synchrotron or Betatron. Initially we consider the integration for a constant value of $\tilde{A}(f)$ that is independent of frequency. In this case the integral to infinity potentially gives an infinite answer. Where the power density is finite (as always) one guesses that either the Fourier coefficients must eventually decrease with frequency or that positive Fourier coefficients exactly cancel negative coefficients at high frequencies. On this basis we undertake the integration as a function of the upper limiting frequency of the integration so that we can infer what happens when the integral is taken to infinity. The integration is also undertaken for differing number of machine revolutions N. For the convenience of plotting the answers and showing how the integral of the sum behaves we

take f_o = 3kHz and f_p = 200 Hz. The integral of the sum will be performed for differing values of θ_p . Results for θ = 0 are given in Figure 26.1

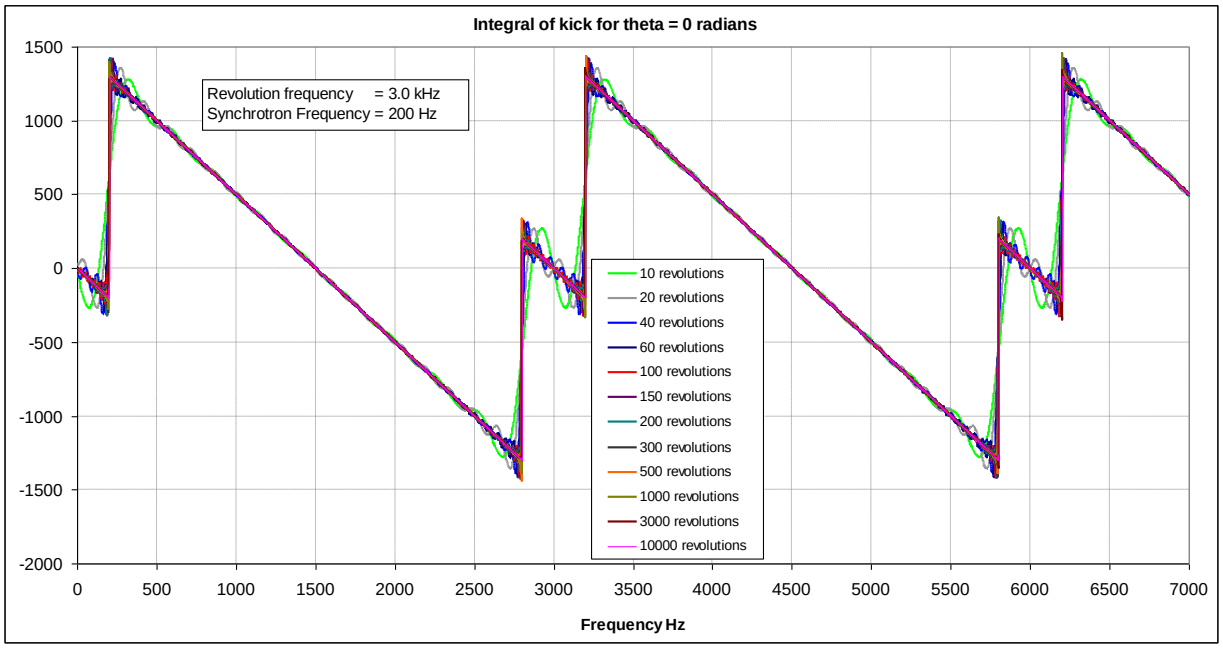

Figure 26.1 Integrated kick factor as function of upper frequency limit, θ = 0

The first critical frequency is for f = 200 Hz. At this frequency the integral increases over a very small frequency range by the amount 1500. The rate at which the integral increases depends on the number of revolutions. This is difficult to see in the figure for the scale given and a close up is shown in Figure 26.2. After the critical frequency at 200 Hz the next critical frequency is 2800 Hz. Between 200 Hz and 2800 Hz the integral decreases with a gradient of exactly minus one. This behaviour was not anticipated by equation (26.29) which is why the approximation did not work. Then at each of the critical frequencies of 2800 Hz and 3200 Hz the integral increases by 1500 giving a total increase of 3000 which is the revolution frequency. This part of the result would have been anticipated by the approximate formula of (26.38) had the integration range been reduced.

The important result is that integration through each pole adds a contribution equal to half the revolution frequency and integration over a frequency interval determined by revolution period frequency but not including the two critical frequencies subtracts the revolution period. Consequently integration to infinity is bounded by the revolution period f_o .

When the actual frequency dependent coefficient $\tilde{A}(f)$ is utilised in the integration then a large kick arises if there is increased noise close to a critical frequency.

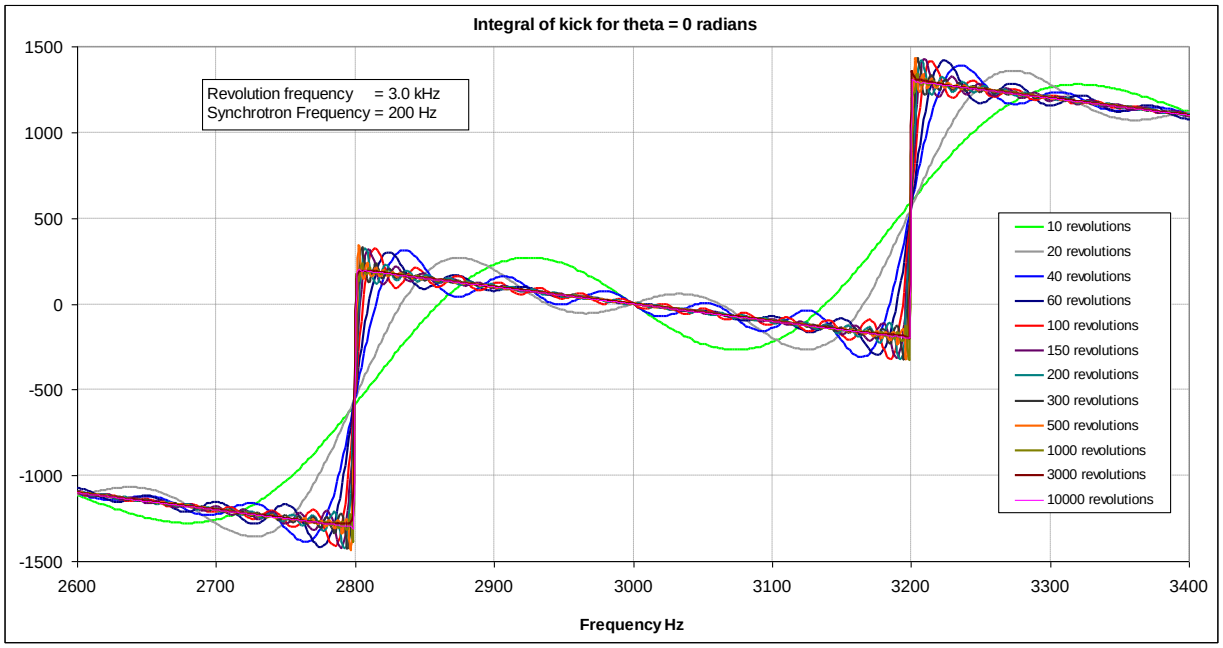

Figure 26.2 Integrated kick factor near 3kHz as function of upper frequency limit, θ = 0

The integration of Figures 26.1 and 26.2 were specific to a starting phase of zero. Figure 26.3 plots the result for a starting phase of π/2. In this figure the approach to a critical frequency contributes with the opposite sign to moving just beyond the critical frequency. This means that increased noise near a critical frequency does not give a net contribution when the particle starts with a phase of π/2. Inspection of the figure also indicates that contribution between critical frequencies also cancels.

Corresponding to the cosine formula of (26.40) there is a corresponding sine formula given by:

$$S = \int_0^{\infty} \tilde{B}(f) \sum_{m=1}^{m=N} \left\{ \sin\left(\frac{f - f_p}{f_o} 2\pi m - \theta_p \right) + \sin\left(\frac{f + f_p}{f_o} 2\pi m + \theta_p \right) \right\} df \qquad (26.41)$$

Thus formula cannot be derived from (26.39) with shift by π/2 and hence has a different appearance to both Figures 26.2 and 26.3 as given by Figures 26.4 and 26.5. Figures 26.4 and 26.5 evaluate the sine formula with $\theta_p = 0$ and $\theta_p = \pi/2$ respectively. It can be seen that critical frequencies do not contribute significantly for $\theta_p = 0$ and give maximum contribution for $\theta_p = \pi/2$.

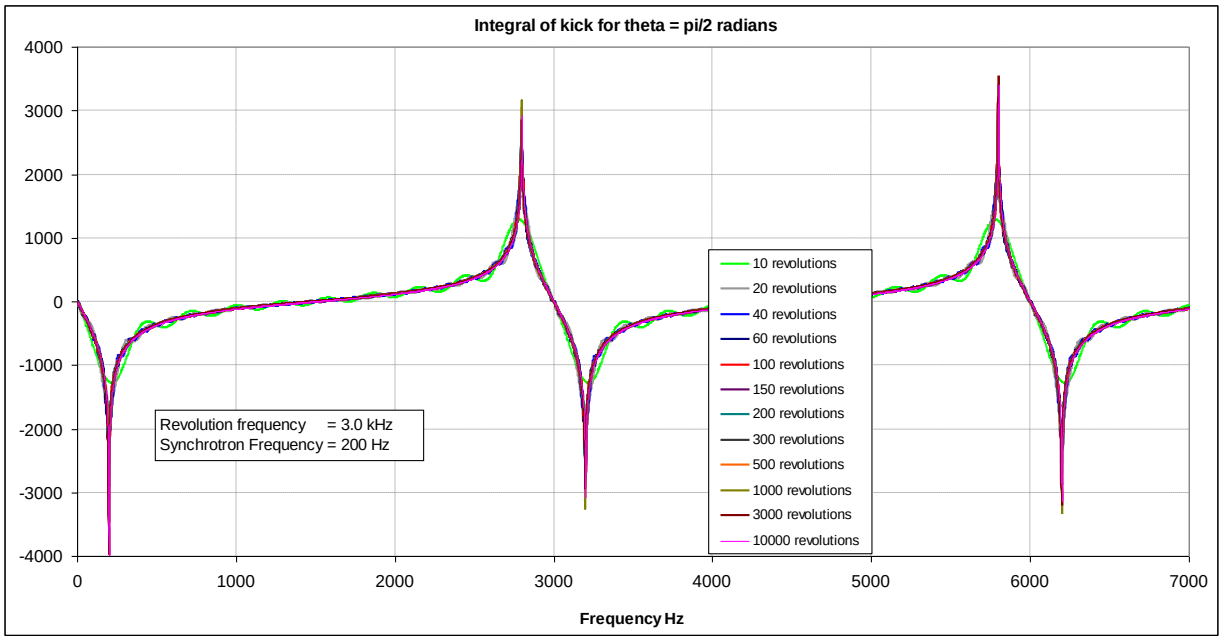

Figure 26.3 Integrated kick as function of upper frequency limit, θ = π/2

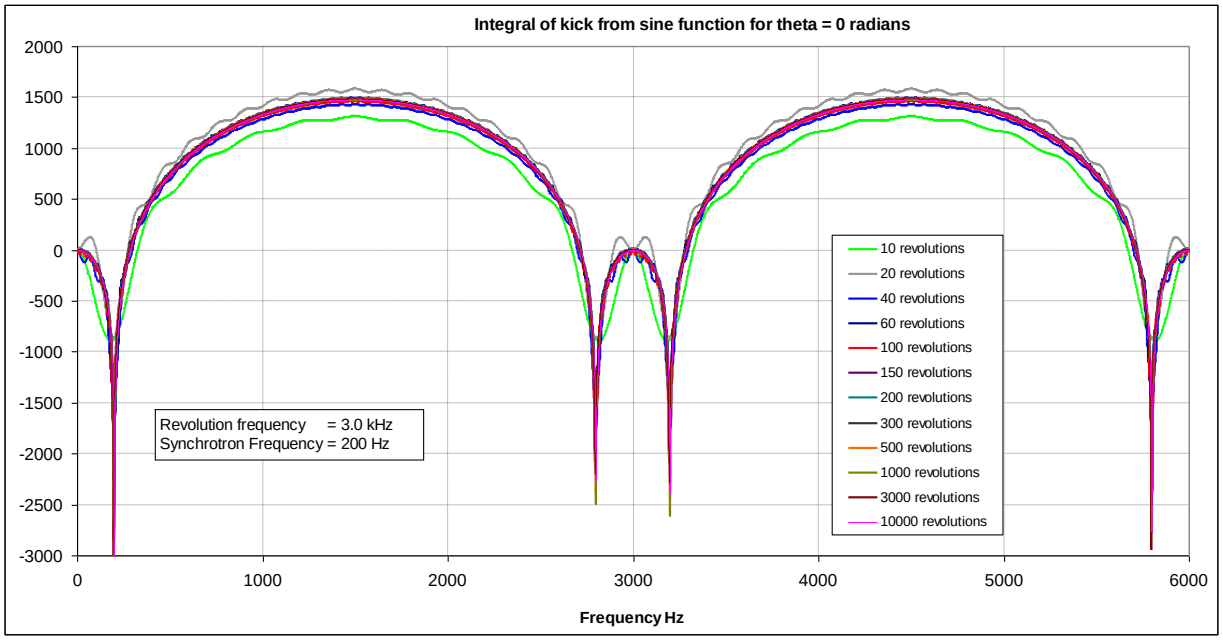

Figure 26.4 Integrated kick factor as function of upper frequency limit, θ = π/2

In Figure 265 the contribution at the revolution frequency minus the critical frequency exactly cancels the contribution at the revolutions frequency plus the critical frequency and the parts in between do not contribute.

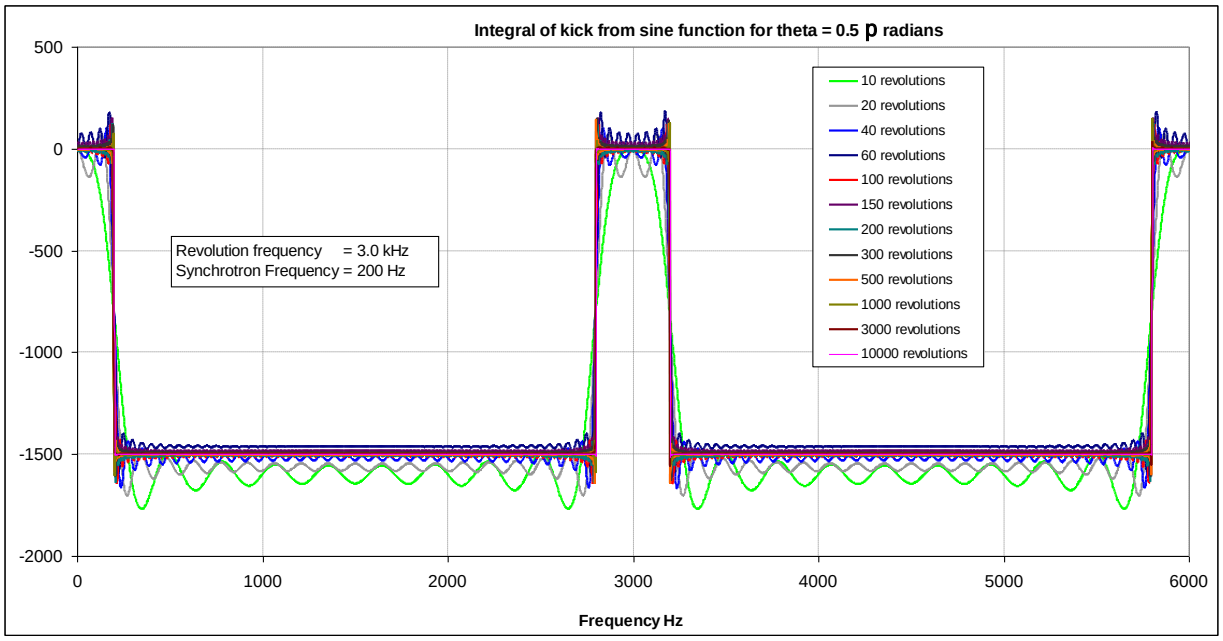

Figure 26.5 Integrated kick factor as function of upper frequency limit, θ = π/2

The interesting feature of this analysis is that perfect noise that does not vary with frequency (white noise) should not result in unwanted kicks.

From (26.21) the worst case scenario for a differential transverse voltage kick on particles in the same bunch occurs when a noise band coincides with a critical frequency and is given by the revolution frequency multiplied by the Fourier coefficient for the frequency multiplied by bunch length expressed as a time, by:

$$\Delta V_x = f_o \tilde{A}_r(f_o \pm f_s)\frac{\omega_{RF}}{2c}\Delta\phi \qquad (26.42)$$

In this equation $\Delta\phi$ is the maximum longitudinal phase deviation of the particle as defined at the start of this section (*i.e. half the bunch length*).

Similarly from (26.22) the worst case scenario for the longitudinal voltage kick is:

$$\Delta V_z = f_o \tilde{A}_r(f_o \pm f_b)\frac{\omega_{RF}}{2c}\Delta x - f_o \tilde{A}_i(f_o \pm f_b)\frac{1}{2}\left(\frac{\omega_{RF}}{c}\right)^2 \Delta\phi\,\Delta x \qquad (26.43)$$

In this equation Δx is the maximum transverse deviation of a particle or half the bunch width at the crab cavity. For an LHC bunch length of 8 cm then $\frac{\omega_{RF}}{c}\Delta\phi \approx 0.67$ and for a bunch width of 1.2 mm at the crab cavity $\frac{\omega_{RF}}{c}\Delta x \approx 0.01$.

From (26.42) we have that excess phase noise at offset frequencies of 23 Hz, 11222 Hz, 11268 Hz and also these frequencies plus multiples of the revolution frequency give transverse growth of a particle's trajectory.

The terms that give longitudinal growth of a trajectory in (26.43) are smaller by a factor of 67 and are excited by noise at offset frequencies of 3400Hz, 7845Hz, 14645Hz, 19090Hz etc

The initial analysis suggested that we might gain this contribution for every harmonic k however figures 26.1, 26.3, 26.4 and 26.5 make the situation far more complex and suggest

that flat noise averages the kick to zero and harmonics give no significant additional contribution. Continuing with the numerical approach it is quite practical to do the summations for tens of thousands of machine revolutions once the Fourier coefficients have been determined. Ideally the Fourier coefficients should be determined for a similar simulation time as the number of revolutions used for determining the typical kicks. Explicitly summations are of the form

$$R = \sum_{n=1}^{n=N} \tilde{A}(f_n) \sum_{m=1}^{m=M} \left\{ \cos\left(\frac{f_n - f_p}{f_o} 2\pi m - \theta_p \right) + \cos\left(\frac{f_n + f_p}{f_o} 2\pi m + \theta_p \right) \right\} \qquad (26.44)$$

These summations will be evaluated in section 26.4.

26.3 Bunch Growth as a Diffusion Process

If the noise acts on all particles in the same way then one gets bunch displacement rather than bunch growth. Bunch displacement is corrected by the Synchrotron control loop and the transverse damping control loop. Inspecting (26.21) and (26.22) it is clear that the synchrotron/ betatron phase θ_p defines the sign of the kick and hence all terms give bunch growth independently of the control loops.

Equations (26.42) and (26.43) predict steady growth of transverse and longitudinal kicks that an individual particle receives whilst it maintains constant phase θ_p . An upper limit estimate of terms in (26.18) is given as $\tilde{V}_x = \sum_{m=1}^{m=N} A_{nr} = NA_{nr} \sim A_{nr} f_o t$ where N is the number of turns and t is the time over which the voltage kick accumulates.

For the simulations of shown in Figure 25.17 the value of A_{nr} ~ -108 dBc hence as a decimal $A_{nr} \sim 10^{-108/20} = 4 \times 10^{-6}$ If one assumes that fluctuations have the same magnitude as the coefficients themselves then given that $f_o \sim 10^4$ then this equation gives a kick of 4% of the set point voltage after one second.

The derivation that arrived at (26.42) and (26.43) implicitly assumes particles change their phase θ_b after a time τ_d and the contribution to linear growth stops at this point with a finite voltage kick having been achieved. Assuming that the linear growth has not resulted in loss of the beam before the phase has varied by $\pi/2$ then the bunch growth moves to a diffusion regime.

The voltage is consequently applied to the particles as coherent strokes coming together so that the total voltage applied is the result of a random walk. At this stage we could relate the voltage stroke to deflections of the particles. As beam dynamics was outside the scope of this study we will just compute the overall voltage. This voltage cannot be properly interpreted because the orbit changes as the voltage is applied and account of damping needs to be included.

For a random walk the average distance squared that is travelled is determined as $\overline{x^2} = \frac{\lambda^2}{\tau} t$

where λ is the mean path and τ is the time to traverse the path. The overall voltage kick that acts on a particle is therefore given as:

$$\overline{V^2} = \frac{\Delta V^2}{\tau_d}\, t \tag{26.45}$$

The effective voltage V_{ave} that acts on a particle after time t is therefore determined as

$$V_{ave} = \sqrt{\overline{V^2}} = \Delta V \sqrt{\frac{t}{\tau_d}} \qquad t >> \tau_d > \frac{1}{f_o} \tag{26.46}$$

where the formula is valid for times much bigger than the de-coherence time and the de-coherence time is bigger than the revolution period. If the de-coherence time is less that period then the period should be used instead.

26.4 Direct Summation

The simulation of 25.5.2 with amplitude errors of 0.05% and phase errors of 5 milli-degrees was repeated for 3000 machine revolutions (~0.25 seconds) and with a beam offset frequency of 46 Hz and a cavity vibration frequency of 70 Hz. This calculation provided a new set of Fourier coefficients spaced at 2.34 Hz intervals up to 300 kHz. (Voltages were averaged over a number of RF cycles to provide 131072 sampling points. Absolute values of the real and imaginary, sine and cosine coefficients obtained are plotted in Figure 26.6 for a small interval either side of the revolution frequency at 11.245 kHz.

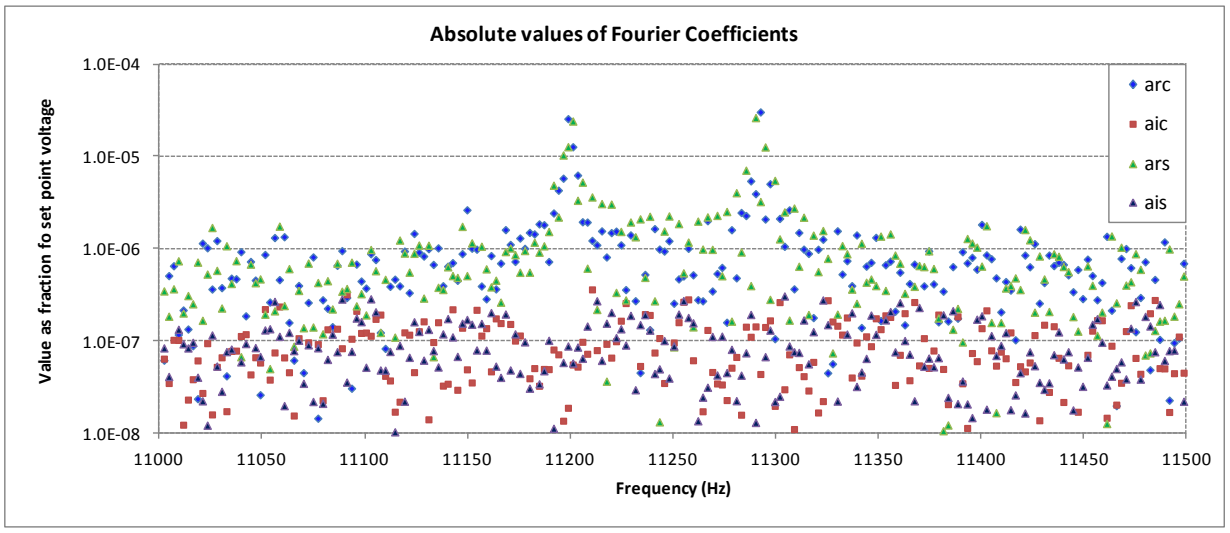

Figure 26.6 Absolute values of Fourier Coefficients near 11245 Hz

Figure 26.7 plots absolute values of Fourier coefficients for the full range. It can be seen that by 300 kHz the Fourier coefficient have fallen by a factor of 6. We have assumed that this range is sufficient for estimation and illustration purposes.

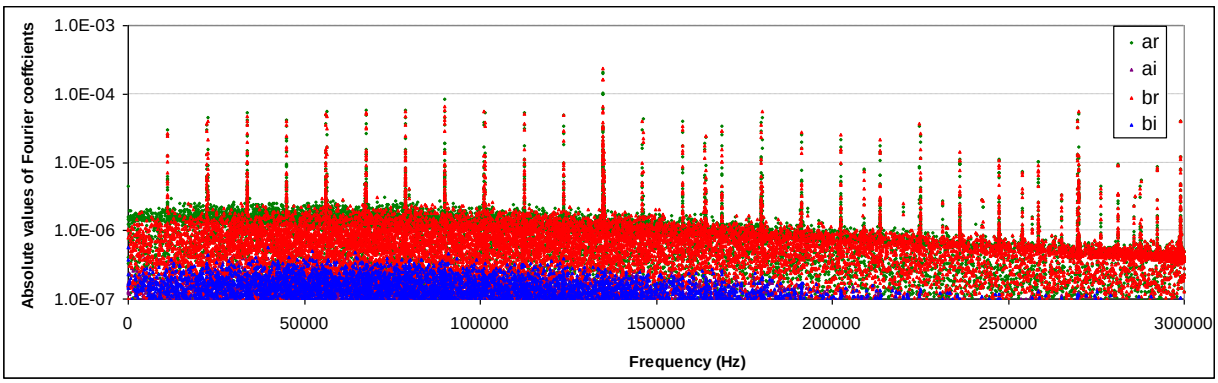

Figure 26.7 Absolute values of Fourier Coefficients

The order of summation given in 5.44 is conveniently switched so the values can be plotted as a function of the number of machine revolutions. The summations performed are given by (26.47) and (26.48):

$$R = \sum_{m=1}^{m=Revs} \tilde{A}_r(f_n) \sum_{n=1}^{n=N} \left\{ \cos\left(\frac{f_n - f_p}{f_o} 2\pi m - \theta_p \right) + \cos\left(\frac{f_n + f_p}{f_o} 2\pi m + \theta_p \right) \right\} \tag{26.47}$$

$$S = \sum_{m=1}^{m=Revs} \tilde{B}_r(f_n) \sum_{n=1}^{n=N} \left\{ \sin\left(\frac{f_n - f_p}{f_o} 2\pi m - \theta_p \right) + \sin\left(\frac{f_n + f_p}{f_o} 2\pi m + \theta_p \right) \right\} \tag{26.48}$$

Nominally f_p might be the synchrotron or the betatron frequency. As fixed frequencies were chosen for cavity disturbances in the simulation it is convenient to f_p vary in (26.47) and (26.48) in order to investigate dependency of proximity of f_p to a disturbance frequency offset from the revolution frequency. Equations (26.47) and (26.48) were evaluated for $\theta_p = 0$ and $\pi/2$ and for the case when the synchrotron/betatron frequency was at the and far away from the disturbance frequency.

In Figures 26.8 and 26.9 the phase was zero and $\pi/2$ respectively and the synchrotron/ betatron frequency was 1000Hz. As both curves could apply to particles in a bunch one is interested in the maximum difference between the graphs. Typically this is of the order of 0.01. As the Fourier coefficients have been normalised by the cavity set point voltage then the differential kick is 100 times smaller than the crabbing kick.

In Figures 26.10 and 26.11 the phase was zero and $\pi/2$ respectively and the synchrotron/ betatron frequency was 46 Hz. Again both curves could apply to differing particles in a bunch. Typically this difference is of the order of 0.8 hence the differential kick is almost equal to the crabbing kick.

When relating these results back to (26.42) and (26.43) it should be remarked that the normalisation for the continuous spectra $\tilde{A}_r(f)$, $\tilde{B}_r(f)$, $\tilde{A}_i(f)$ and $\tilde{B}_i(f)$ was dBc/Hz whereas the normalisation for the discrete spectra $\tilde{A}_{nr}$, $\tilde{B}_{nr}$, $\tilde{A}_{ni}$ and $\tilde{B}_{ni}$ was dBc. With respect to data in figure 26.7 frequencies were df = 2.34 Hz apart and hence discrete coefficients must be divided by 2.34. In order to make the comparison one uses:

$$\text{kick factor} \sim f_o \text{Max}\left[\tilde{A}_r(f)\right] = f_o \text{Max}\left[\tilde{A}_{nr}/df\right] \tag{26.49}$$

The maximum Fourier coefficients away from critical frequencies ~ 2.4×10^{-6} hence one expects a kick factor of $11245\times2.4\times10^{-6}/2.34=0.012$.

The maximum Fourier coefficients at the worst critical frequencies ~ 2.35×10^{-4} hence we expect a kick factor of $11245\times2.34\times10^{-4}/2.34=1.1$.

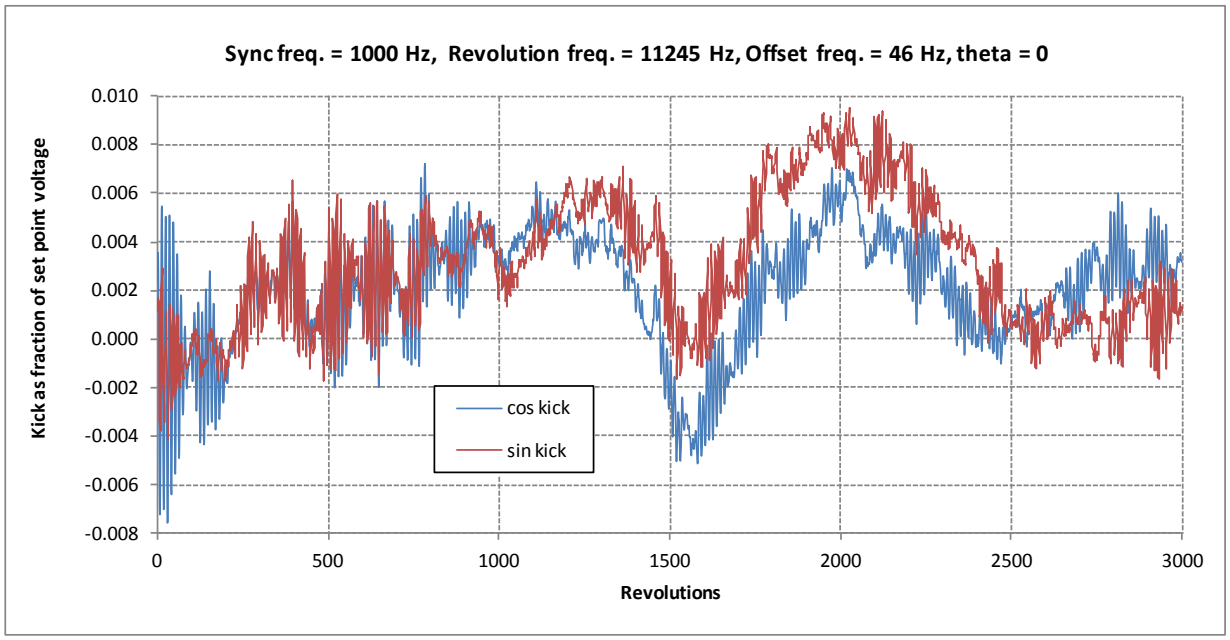

Figure 26.8 Integrated kick as function of revolutions for the disturbance frequency far from the Synchrotron frequency and zero phase

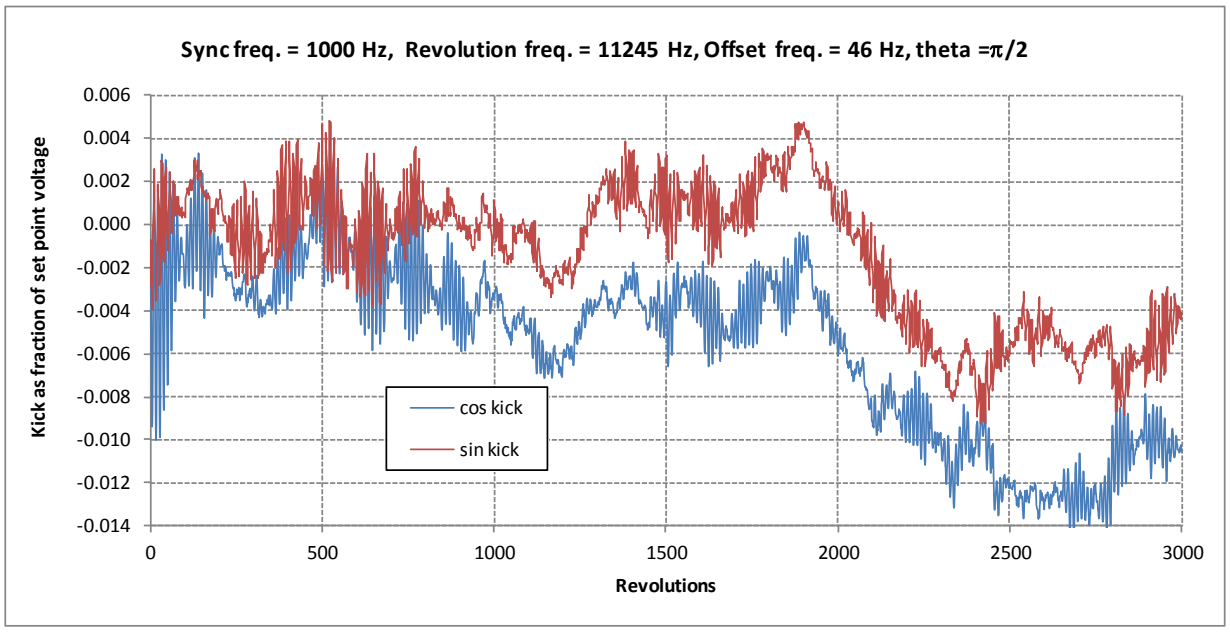

Figure 26.9 Integrated kick as function of revolutions for the disturbance frequency far from the Synchrotron frequency and phase of π/2

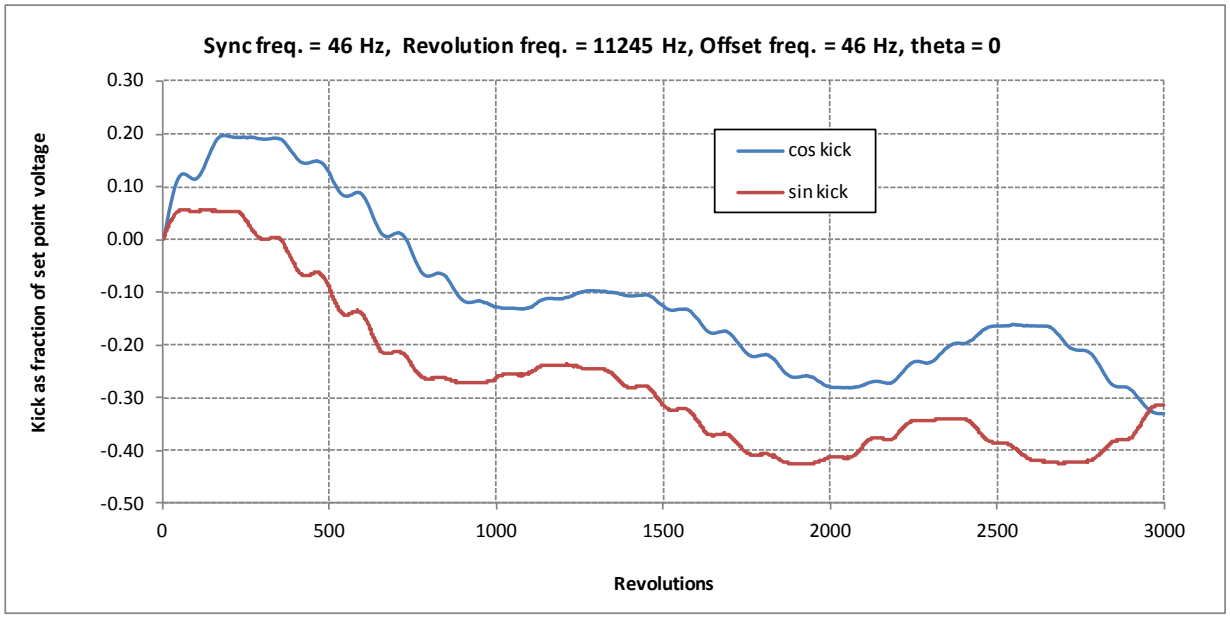

Figure 26.10 Integrated kick as function of revolutions for the disturbance frequency at the Synchrotron frequency and for phase of 0

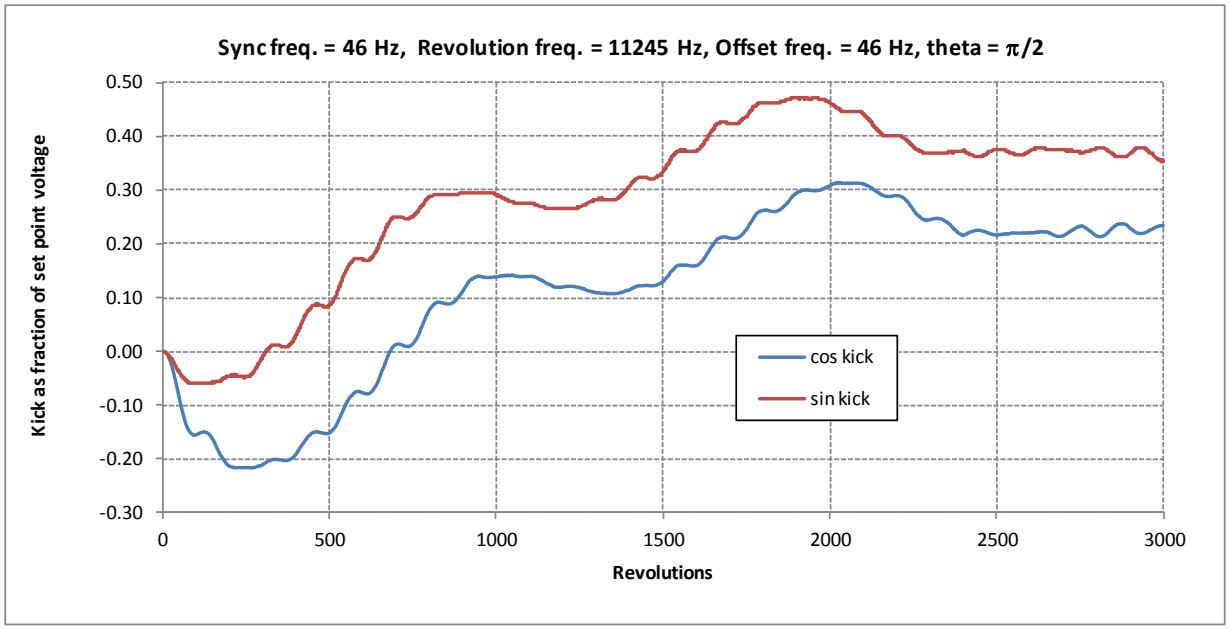

Figure 26.11 Integrated kick as function of revolutions for the disturbance frequency at the Synchrotron frequency and for phase of π/2

In order to complete the analysis using (26.46) then the de-coherence time needs to be known. For illustrative purpose we will take the value as 0.2 seconds as this is the time for about 2000 revolution at which the kick seems to have maximised for the case where the disturbance is away from the Synchrotron frequency as shown in Figures 26.8 and 26.9. For the transverse kick there is an additional factor of $\frac{\omega_{RF}}{2c}\Delta\phi \approx 0.33$ coming from (26.21) hence $\Delta V/V_{sp}$ =

0.0033. Putting numbers in to (26.45) one obtains $V(t) = \Delta V\sqrt{\frac{t}{\tau_d}} = 0.007\sqrt{t}$ hence one has about 20000 seconds before the differential voltages that have acted on differing particles in the bunch become equal to the cavity set point voltage. This time is only a guideline on lifetime and of course it has been evaluated for an artificial case. It should also be remembered that four sets of crab cavities act on each beam hence growth is twice as large as it would be of a single crab cavity system as analysed. The important conclusion of this section is that all cavity disturbances at the synchrotron frequency must be heavily suppressed.

27. Conclusions to Part 2 (LHC)

Potential beam offsets at the LHC Crab cavities could demand a substantial power requirement. The analysis here assumes that active steering limits offsets at the crab cavities to 0.25 mm. With this assumption a crab cavity providing a transverse kick of 3.3 MV each can handle beam loading and anticipated microphonic detuning of up to 40 Hz with a power input of just 8.5 kW and with an external Q factor of 0.57×10^6.

Simulations have been developed to analyse the control performance of the crab cavity assuming an IQ controller, the code uses the actual LHC bunch structure, applies beam loading on every RF cycle, encompasses realistic disturbances and takes account of field measurement errors. The simulations are aimed at determining the level of voltage noise that will occur in the cavity as a consequence of measurement errors and in the presence of disturbances. (This noise is expected to be larger than noise coming from the master oscillator that is locked to the revolution period.)

Failure modes for the crab cavity have been assessed. For the external Q value chosen, cavity quench and loss of amplifier power will not be an issue. A failure of the LLRF controls which drives the cavity 90^o out of phase could be damaging to the LHC. A safety critical system that is independent of the cavity LLRF controls would need to measure phase difference between the RF and the beam and employ a fast kicker to correct the offset caused by an incorrectly phased cavity.

An analysis has determined how Fourier coefficients for voltage noise in the cavity relate to the time averaged voltage that acts differentially on particles in a bunch. For a mechanically stiff cavity, phase noise is smaller and less serious than amplitude noise. The significant mitigation factor for amplitude noise is to reduce amplitude measurement errors in the cavity. Ideally one would like to measure amplitude with a bandwidth of 1 MHz to an accuracy of 1 part in 2^{16}. Whilst this accuracy is not available at the moment it is certainly achievable with the next generation of LLRF boards.

28. References

[1] "*A Multi-TeV linear collider based on CLIC technology: CLIC Conceptual Design Report"* edited by M. Aicheler, P. Burrows, M. Draper, T. Garvey, P. Lebrun, K. Peach, N. Phinney, H. Schmickler, D. Schulte and N. Toge.

[2] R.B. Palmer "*Energy scaling, crab crossing and the pair problem*", SLAC-PUB-4707, 1988

[3] G. Burt, A. Dexter , P. Goudket, A.C and A. Kalinin, "*Effect and tolerances of phase and amplitude errors in the ILC Crab Cavity*", EUROTeV Report 2006-098

[4] W. J. Gallagher et.al. , "*The RF Travelling Wave Particle Deflector*," IEEE Trans. on Nuclear Sci., 1965

[5] P.K. Ambattu, G. Burt, V. F. Khan, R.M. Jones A.C. Dexter and V. Dolgashev "*Analysis and Control of Wakefields in X-Band Crab Cavities for Compact Linear Collider*", TH10, XB-2010, Daresbury, December 2010

[6] A. Dexter and G. Burt "*Phase and Amplitude Control of Dipole Crabbing Modes in Multi-Cell Cavities*", EUROTeV-Report-2008-064, 2008

[7] J. Frisch, "NLC Crab Cavity Phase Stability", LCC-0136, SLAC-TN-04-004, March 2004.

[8] F. Peauger et al. "*A 12 GHz RF Power Source for the CLIC Study*", THPEB053,Proc IPAC 2010, Kyoto, Japan, pp 3990-3991

[9] J. W. Staples, R. Wilcox and J. M. Byrd, "Demonstration of femto-second phase stabilization in 2 km optical fibre", Proceedings of PAC07, Albuquerque, New Mexico, USA,

[10] ArcelorMittal "*INVAR® Controlled Expansion Alloys*" http://www.arcelormittal.com/stainlessandnickelalloys/fileadmin/pdf/datasheets_uk/Invar_EN.pdf

[11] R. J. England et.al., "*X-band Dipole Mode Deflection Cavity for the UCLA Neptune beamline"*, Proc. PAC-2005, Tennessee

[12] P.K. Ambattu, G. Burt, R.G. Carter, A.C. Dexter, R. Jones and P. McIntosh, "*Initial study on the shape optimisation of the CLIC crab cavity*", THP024, Proc LINAC08, Victoria, BC, Canada

[13] A. C. Dexter, G. Burt, P.K. Ambattu, V. Dolgashev and R. Jones, "*CLIC Crab Cavity Design Optimisation for Maximum Luminosity*", to be published in Nuclear Instrumentation and methods 2011

[14] I. Syratchev. *"Variable High Power RF Splitter and RF Phase Shifter For CLIC"*. CERN, Switzerland : CERN-OPEN 2003

[15] Kurtz, Stephen R. "*Mixers as Phase Detectors"* San Jose : WJ Communications, 2001.

[16] S Watson, H C Wee, H Griffiths, RJ Williams. "*A highly phase-stable differential detector amplifier for magnetic induction tomography."* University of Glamorgan,UK : IOP Publishing, 2011, Vol. Physiol. Meas.

[17] Andersson, Alexandra. "*Phase Detection Electronics For CLIC."* IPAC2011, San Sebastian, Spain : 2011.

[18] Yi-Peng Sun, R. Assmann, J. Barranco, R. Tomas, T. Weiler, F. Zimmermann, R. Calaga, A. Morita, "*Beam Dynamic Aspects of Crab Cavities in the LHC*", Phys. Rev. ST Accel. Beams 12, 101002 (2009)
http://prst-ab.aps.org/abstract/PRSTAB/v12/i10/e101002

[19] Hall B., Burt G., Lingwood C., Rimmer R., Wang H., "*Novel Geometries for the LHC Crab Cavity*" WEPEC049 IPAC10,
http://accelconf.web.cern.ch/AccelConf/IPAC10/papers/wepec049.pdf

[20] F. Zimmermann, "*LHC upgrade scenarios*," Particle Accelerator Conference, 2007. PAC. IEEE , vol., no., pp.714-718, 25-29 June 2007,
http://ieeexplore.ieee.org/stamp/stamp.jsp?tp=&arnumber=4441113&isnumber=4439905

[21] R.B. Palmer "*Energy scaling, crab crossing and the pair problem*", SLAC-PUB-4707, 1988

[22] T. Leiri, K.Akai, H. Fukuma, M. Tobiyama " *Beam dynamics measurements using a gated beam position monitor at KEKB*", Nuclear Instruments and Methods A, Vol. 606, No 3, July 2009, http://dx.doi.org/10.1016/j.nima.2009.04.036

[23] Bruning O., Burkhardt H. and Myers S. "*The Large Hadron Collider*" CERN–ATS-2012-064 http://cdsweb.cern.ch/record/1443022/files/CERN-ATS-2012-064.pdf

[24] Maria R. and Fartoukh S. "*Optics and layout for the HL-LHC upgrade project with a local crab cavity scheme*", sLHC-project report 0055, July 2011
http://cdsweb.cern.ch/record/1364853/

[25] E. Ciapala et al. "*LHC Crab cavity specifications*", EuCARD-REP 2012-004 August 2010. http://cdsweb.cern.ch/record/1287113

[26] G. Burt, A. Dexter , P. Goudket, A.C and A. Kalinin, "*Effect and tolerances of phase and amplitude errors in the ILC Crab Cavity*", EUROTeV Report 2006-098
http://www.eurotev.org/reports__presentations/eurotev_reports/2006/

[27] A. Dexter and G. Burt "*Phase and Amplitude Control of Dipole Crabbing Modes in Multi-Cell Cavities*", EUROTeV-Report-2008-064, 2008
http://www.eurotev.org/reports__presentations/eurotev_reports/2008/

[28] Angoletta M.E. "*Digital Low Level RF*", WEXPA03, EPAC 2006
http://accelconf.web.cern.ch/accelconf/e06/PAPERS/WEXPA03.PDF

[29] Baudrenhien P. "*LLRF for Crab Cavities*" LHC-CC1 5th Crab Cavity Workshop CERN, Nov 2011
http://indico.cern.ch/getFile.py/access?contribId=25&sessionId=6&resId=1&materialId=slides&confId=149614

[30] Boussard D. "Design of a Ring RF System", CERN SL/91-2 (RFS)
1. http://cdsweb.cern.ch/record/1023436/files/CM-P00065157.pdf

[31] Baer T., Calaga R., De Maria R., Fartoukh S., Jensen E., Tomas R., Tuckmantel J., Wenninger J., Yee Rendon B., and Zimmermann F., "Very Fast LHC Crab Cavity Failure and Their Mitigation", IPAC12 http://accelconf.web.cern.ch/accelconf/IPAC2012/papers/moppc003.pdf

[32] Sands M. "*The Physics of Electron Storage Rings An Introduction*", SLAC 121 UC-28 November 1970 http://www.slac.stanford.edu/pubs/slacreports/slac-r-121.html

[33] Boussard D. "*RF for the CERN Proton-Antiproton Collider*" CERN SPS/85-38 http://cdsweb.cern.ch/record/162005/files/cer-000073340.pdf

[34] Pinwinski A. "*Intra-Beam Scattering*" Proc. CERN Accelerator School, pp 402-421, Oxford 1985, http://cdsweb.cern.ch/record/179307/files/CERN-87-03-V-1.pdf

[37] Evans L. and Gareyte J. "*Beam- beam effects"*, Proc. CERN Accelerator School pp 159-185, Oxford 1985 http://cas.web.cern.ch/cas/

[36] Ohmi K., Calaga R., Tomas R., Hofle W., Zimmermann F. "*Beam-beam effect with an external noise in LHC*" TUPAN048 PAC07 http://care-hhh.web.cern.ch/CARE-HHH/LUMI-06/Proceedings/IR%20Upgrade%20II/lhcbb2-Ohmi.pdf

[37] Ohmi K., "*Beam-beam limit in a hadron collider"*, THYB01 IPAC2012 http://accelconf.web.cern.ch/accelconf/IPAC2012/papers/thyb01.pdf

29. Acknowledgements

This work has been funded by the UK research council STFC as part of the Cockcroft Institute Core Grant number ST/G008248/1 and by the European Union under the FP7 EuCARD IA Project Grant agreement. 227579.